ZNO-BASED OXIDE-METAL VERTICALLY ALIGNED NANOCOMPOSITES FOR TUNABLE HYPERBOLIC METAMATERIALS

by

Robynn-Lynne Paldi

A Dissertation

Submitted to the Faculty of Purdue University

In Partial Fulfillment of the Requirements for the degree of

Doctor of Philosophy

School of Materials Engineering

West Lafayette, Indiana

August 2021

THE PURDUE UNIVERSITY GRADUATE SCHOOL

STATEMENT OF COMMITTEE APPROVAL

Dr. Haiyan Wang, Chair

School of Materials Engineering

Dr. Xinghang Zhang

School of Materials Engineering

Dr. Marinero Ernesto

School of Materials Engineering

Dr. Elliot Slamovich

School of Materials Engineering

Approved by:

Dr. David Bahr

Dedicated to all those who thought I would never amount to anything.

ACKNOWLEDGMENTS

I would like to first express my deepest appreciation and gratitude to my research advisor, Dr. Haiyan Wang. Without her guidance and encouragement during the oftentimes lonely and grueling hours spent working on research and my thesis, completing my degree would not have been possible. She not only helped instill a sense of research insight into me but helped facilitate my development as a scientist and engineer. She always was happy to discuss many of my crazy ideas and provide her own insight and guidance in shaping it into a tangible research direction. I moved over 2000 miles away from my home and support network in California to pursue my education at Purdue, and in the time of my PhD, she has become not only a great source of professional knowledge but has provided much personal knowledge. During our numerous discussions, she has always known exactly what to say whether on research or personal matters, and I am always impressed by her knowledge. I have learned so much from her advising and will be forever grateful to her for the many opportunities she has provided me by working in her group. Her advice has always been expressed with great enthusiasm and has always been able to cheer me up. She has always strived to do the best for her students and me, and I hope that in the research I have conducted while in her group and in my career, I can live up to the potential she sees in me.

I would also like to thank my graduate committee: Dr. Xinghang Zhang, Dr. Ernesto Marinero, and Dr. Elliot Slamovich for their input and suggestions in guiding my research. I greatly appreciate the time and effort they have taken to give me careful feedback and in attending my prelim, data review, and final exam.

I also want to thank our collaborator at Sandia National Labs, Dr. Aleem Siddiqui. Working with Dr. Siddiqui has provided new research insight and directions I would not have thought of without our many fruitful discussions every 1st and 3rd Wednesday of the last two years. He has provided the opportunity to learn more in-depth about device structure where most of my previous work has only been considering the materials fabrication side. Moreover, it has taught me how to better communicate my ideas to a wide audience. His guidance and support in both research and career advice have been helpful for development.

I would also like to thank my group members and colleagues in Dr. Haiyan Wang's functional thin film group, the alumni (Dr. Xing Sun, Dr. Jijie Huang, Dr. Jie Jian, Dr. Bruce Zhang, Dr. Leigang Li, Dr. Shikhar Misra, Dr. Han Wang, Dr. Zhimin Qi, and Dr. Xingyao Gao) and the current members (Dr. Xin Li Phuah, Dr. Di Zhang, Dr. Matias Kalaswad, Juanjuan Lu, James Barnard, Jianen Shen, Yizhi Zhang, Bethany Rutherford, Junchen Liu, Jiawei Song, Hongyi Dou, and Zihao He). I am very grateful especially to Xin Li Phuah for her deep friendship during my PhD. I feel so lucky to have the opportunity to have worked with so many bright and potential researchers.

Last but certainly not least, I would like to express my gratitude to thank my friends and family for their continued support during my PhD. I have matured and changed a great deal over the last four years, and they have stuck around to watch me undergo such transition. My best friend Jessica Taylor and her husband Ryan Taylor have provided unwavering friendship and support of which I will forever be grateful for. I would also like to thank my best friend, Mr. TT. He is a Cardigan Welsh Corgi and my support dog; he has provided a many snuggles and cuddles to comfort the many downtimes in my PhD. And to my parents, who continue to support and love me the same whether they are picking me up from school in the first grade or watching me walk across the stage to receive my PhD. Thank you.

TABLE OF CONTENTS

LIST OF TABLES

LIST OF FIGURES

ABSTRACT

Vertically-aligned nanocomposite thin films have recently emerged as a platform to combine multifunctionalities. These materials are made up of two co-grown immiscible phases where one phase grows as anisotropic vertical pillars in the matrix of the second phase. Many of the classic systems of VAN consist of oxide-oxide nanocomposites but more recently the oxide-metal combinations have been realized with great promise of combining metal and oxide functionalities. In particular for streamlined processing of hybrid plasmonic metamaterials with nanoscale light matter manipulation. The work presented in this dissertation is towards realizing oxide-metal VAN with ZnO as the matrix. ZnO is particularly interesting for composite design due to its breadth of properties including piezoelectricity, semiconductivity, relative non-toxicity, and wide-spread availability making it applicable for sustainable and compact device designs. In the first part of this dissertation, ZnO is combined with plasmonic Au to form ZnO-Au VAN. The ZnO-Au design demonstrates highly ordered and tunable in-plane periodicity which results in strong hyperbolic dispersion and plasmonic response, making it desirable for hybrid plasmonic hyperbolic metamaterials. The resultant morphology has spontaneous and controllable quasi-hexagonal in-plane order and a tailorable microstructure through deposition parameter control.

In the second part of this work, a new oxide-nanoalloy VAN system of ZnO-Au_xAu_{1-x} is designed to reduce the optical losses of Au in hyperbolic metamaterials application. Ag is combined with Au to reduce losses and overcome particle-in matrix morphology of ZnO-Ag, with the result being reduced losses as compared to ZnO-Au. The third part investigated the tunability of the new oxide-nanoalloy VAN ZnO-Au_xAg_{1-x} through the oxygen background pressure. Both optical properties and morphology were shown to be strongly correlated with the background pressure.

In the final part, ZnO is combined with ferromagnetic metals of Co, Ni, and their alloy Co_xNi_{1-x} for ferromagnetic/piezoelectric coupling. Oxidation was found to occur due to the high reactivity of Ni and Co to oxygen ambient, with ZnO-Co growing as an oxide-oxide VAN of ZnO-CoO. ZnO-Ni and ZnO-Co_xNi_{1-x} demonstrated anisotropic ferromagnetic and optical response. The work presented in the body of this thesis serve to demonstrate ZnO-based

nanocomposite towards future device and heterostructure integrations in both optical and acoustic applications.

1. INTRODUCTION AND BACKGROUND

Functional oxides and their nanocomposites have attracted great research interests and are considered as one of the key material components for various device applications ranging from microelectronics, sensors, optical devices, optoelectronics, catalysis, and many others. This introduction chapter first discusses the background of oxide thin films, especially functional oxides and their applications (Section 1.1). The second part of the chapter presents the deposition methods to grow high quality oxide thin films (Section 1.2). The third part focuses on ZnO and their thin film structures (Section 1.3). The fourth part focuses on the new vertically aligned nanocomposites and their different types based on material systems (Section 1.4). The fifth part discusses the properties and background of plasmonics and light/matter interactions (Section 1.5). The final sixth part gives the motivation for the work conducted in this thesis (Section 1.6).

1.1 Oxide thin films

1.1.1 Functional oxide thin films

Extensive work and studies have been conducted for the development of next-generation integrated device application in the search for sustainability and compactness. Materials in thin film form offer a more elegant platform for compact and sustainable device integration over their bulk counterparts. Functional oxide thin films and heterostructures offer an emergent pathway for device application across a breadth of fields with a wide range of multifunctionalities. Oxide thin films include unique functional properties such as ferroelectricity, thermoelectricity, piezoelectricity, superconductivity and more that can all be tuned to fit specific device needs. These functional properties are highly dependent on the film morphology, strain effects, and oxygen stoichiometry and are tailorable by variations in the specific growth methods. Oxide films offer a range of structures such as wurtzite, corundum, zircon, perovskite, and many other.

There are two types of classification for these materials including simple oxides and complex oxides. Simple oxides are inorganic, ionic compounds which consist of a metal cation bound to an oxygen ion. Metal oxides have chemical formula $M_a^{x+}O_b^{2-}$ where a and b refer to the stoichiometry of each constituent and x is the charge of the metal cation. Common binary oxides include ZnO, MgO, VO_2, and Al_2O_3. The second class of oxides are the complex oxides which

have more than one cationic species in the chemical formula, such as $BaTiO_3$, $SrTiO_3$, and more. The research into application of functional oxide thin films for electronic and magnetic devices greatly expanded after the discovery of a high-temperature superconducting $YBa_2Cu_3O_7$ (YBCO). Many of the tunable properties realized in functional films are based on the extreme sensitivity of electronic changes due to very small structural variation.

Minute changes to the crystal structure within an oxide thin film result in dramatic affects to the functional properties. Such small structural changes can be induced via strain, defects, and interface control. Point defect formation is highly variable in functional oxides, and it is typical that higher melting temperatures result in higher defect formation energy. The ZnO system is one exception to this with a defect formation energy as low as 2.5 eV while the typical ranges for binary oxides are from 5-10 eV. Another contributing factor to defect formation is thermal excitation and oxidation/reduction which results in metal/oxygen stoichiometry. Brouwer diagrams provide a fundamental description of defect concentrations at different oxygen pressure and can describe oxide defect chemistries. The Brouwer diagram for ZnO is shown in Figure 1.1. In this example, the different partial pressure regimes for pO_2 are shown, such that the plot reads defect concentration as a function of log pO_2, showing which defects are dominating under which experimental conditions. Oxygen vacancies are dominating in the low pO_2 regime and Zn interstitials are dominating at high pO_2. In the ZnO system, the availability of excess intrinsic defects will determine the property of the film, leading to specifically engineered application. The Brouwer diagram demonstrates the sensitivity of oxide thin film cation/anion stoichiometry.

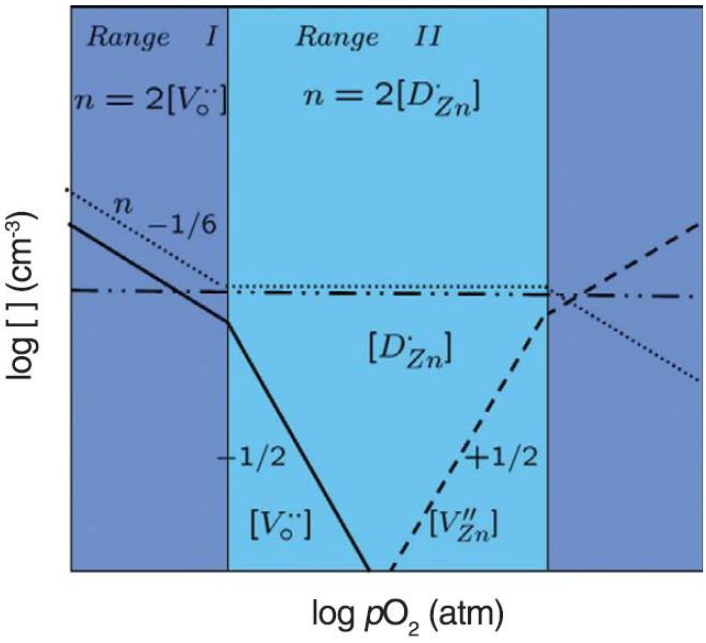

Figure 1.1 Brouwer diagram for ZnO. Adapted from [1]

The sensitivity of oxide thin film functional properties is greatly affected by interfacial strain and lattice mismatch. Oxides at their interfaces tend to become non-stoichiometric, strained, and have induced defects. The lattice mismatch in controlling oxide thin film properties is driven by the structural differences between the lattice and oxide thin film grown. Examples of epitaxy are given in Figure 1.2. The lattice mismatch is given by the following Equation 1:

$$\text{Equation 1: } f = \frac{a_f - a_s}{a_s}$$

In equation one a_s and a_f are the substrate and film lattice parameter, respectively, and f is the lattice mismatch. The general rule of thumb when f >0, the film will be in compression, and if f<0, the film will be in tension. Films can have different coherency, as described in Figure 1.2; coherent, semi-coherent, or incoherent. Coherent films as shown in Figure 1.2a and b form when the lattice misfits are <±10%. Semi-coherent films like in Figure 1.2c occur when misfit is <20%. The large mismatch is rectified by dislocation formation at the interface to relieve misfit strain. The misfit f>20% will create incoherent interface as that shown in Figure 1.2d, such that 20% misfit strain can be considered a limit for strained epitaxial film growth. Moreover, during epitaxial growth, the film orientation will align itself such that the interfaces will have the least misfit strain. The lattice mismatch and strain effect on oxide thin films is greatly evidenced in

ferroelectric perovskite thin films such as $BaTiO_3$ and $SrTiO_3$ [2,3]. When critical film thickness is below 50nm, the ferroelectric curie temperature T_c, remnant polarization, and the structural phase transition are highly tunable through strain engineering. Multilayering of the films also provides another avenue for tailoring the strain and properties [4,5].

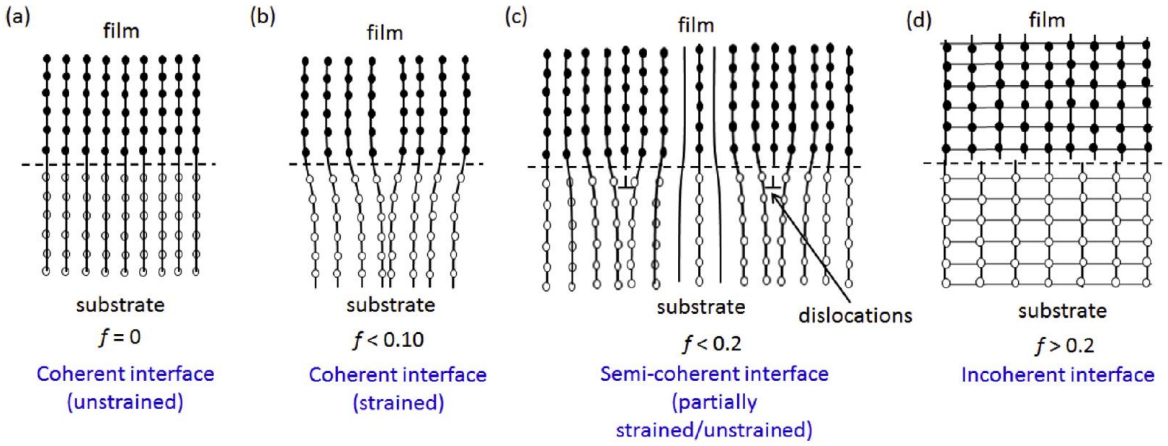

Figure 1.2 Types of epitaxy at film and substrate heterointerfaces. a) unstrained coherent interface, b) stained coherent interface, c) semi-coherent interface, d) incoherent interface. Adapted from [6].

1.1.2 Applications of oxide thin films

Applications of oxide thin film span the range of optical, magnetic, and electrical applications. The research into functional oxide thin films for device application came to prominence after the discovery of high temperature superconductivity in $YBa_2Cu_3O_{7-x}$ (YBCO) thin films. The practical application, though, of oxide thin films is still greatly limited and inhibited by a lack of proper control of stoichiometry and defect formation. Some oxides have found use, such as transparent indium tin oxide (ITO) and Al-doped zinc oxide (AZO) thin films in solar cells and displays as electrodes; [7,8] Other examples include ferroelectric oxides in ferroelectric random access memory (FeRAM), [9], binary oxides such as SiO_2 used as gate dielectrics in MOSFETs [10], and binary oxides such as SnO_2 and ZnO as gas sensors [11].

The limiting factor of widespread applications of oxide thin films is the control of the defects and stoichiometry which many of the unique functionalities are directly controlled through. For example, in $YBa_2Cu_3O_{7-x}$superconducting films, superconductivity only occurs for oxygen stoichiometry $6.37 \leq x \leq 7.0$, in which it undergoes a phase transition from tetragonal to the superconducting orthorhombic phase [12]. Some oxide thin films are interesting for their

ability to demonstrate magnetoelectric coupling. Magnetoelectric coupling is the change in an electric polarization in response to a magnetic field, for example in $TbMnO_3$ and $TbMn_2O_5$ [13,14]. The major application of this is in exchange coupling, where a ferromagnet and antiferromagnet are interfacially coupled and the ferromagnetic spin domains are tunable through flipping the orientation of the antiferromagnet. Multiferroic exchange coupling is widely seen as applicable to electrical switching of spin devices in spintronics, with oxides such as $BiFeO_3$ receiving the most attention for this application [15].

1.2 Growth methods for oxide thin films

1.2.1 Thin film growth mechanics

The major workhorse for oxide thin film growth is vapor phase deposition techniques, which as the name implies, involve growth of thin films from a gaseous vapor phase. The basic growth is described as follows: vapor atoms will impinge upon the substrate face and are entered into the adsorbed state, referred to as adatoms. Adatoms may either re-sputter or diffuse across the substrate surface. In the ideal situation, adsorption sites will be equally distributed across the substrate surface and diffusing adatoms will clump together. If a critical size is reached, adatoms will nucleate and grow to form the initial thin film growth. Nucleation and growth usually proceed via one of three growth modes: 3D island growth, 2D layer growth, or 2D+3D island+layer growth. The major factor which determines the type of growth is related to the binding energy. E_b is the measure of the bond strength between a pair of adatoms and E_a is the measure of the strength between the adatoms and the substrate. For $E_a > 3E_b$, 2D layer growth is expected, and for $E_a < 3E_b$, 3D layer growth is expected. When $E_a \sim E_b$, kinetic effects are considered and a 3D+2D mix growth may result. In the 2D layer growth, a true layer by layer deposition is expected. In the 3D+2D growth, an initial 2D few layers will grow with local areas of 3D vertical growth.

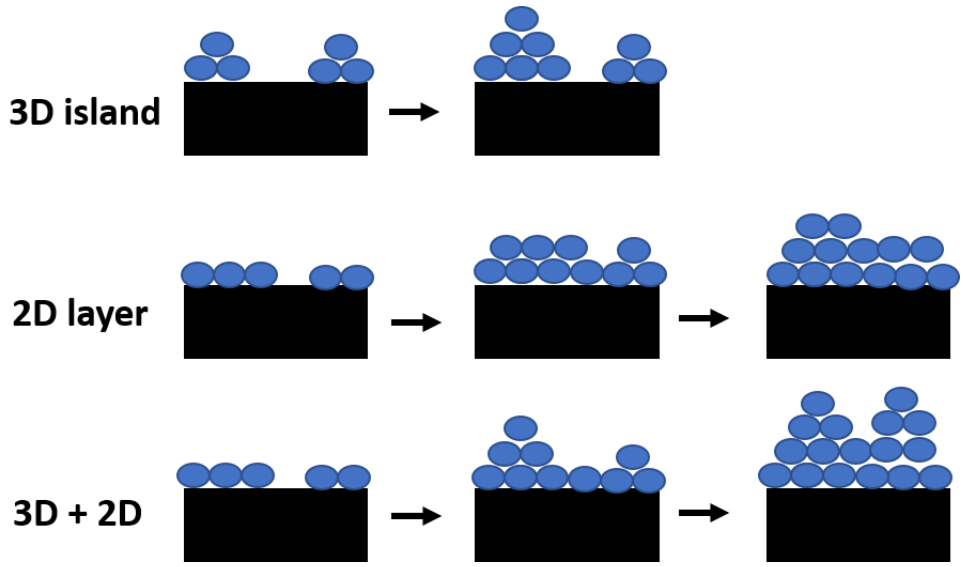

Figure 1.3 Schematic diagram showing film growth modes.

Another way to consider thin film growth is through Young's relation, e.g. wetting of the thin film of the surface of the substrate. In this relation, the wettability of thin films on substrates can be described as a balance of the surface energies, and certain interfacial tension relationship will lead to either 2D, 3D, or 2D+3D growth. An overview of an ideal, defect free substrate with an adatom wetting the surface is shown in Figure 1.4. The relationship is described as a balance at the contact angle θ where the film, vapor, and substrate all intersect. The interfacial energies are γ_{fs} for the film substrate boundary, γ_{fg} for the film and vapor boundary, and γ_{sg} substrate and vapor. The Young's relation for the contact angle is then given by equation 2:

$$\text{Equation 2 } cos\theta = \frac{\gamma_{sg}-\gamma_{fs}}{\gamma_{fg}}$$

For layer growth to occur, θ ~0 and $\gamma_{sg} < \gamma_{fs} + \gamma_{fg}$. In the event of island growth, θ < 0 and $\gamma_{sg} \sim \gamma_{fs} + \gamma_{fg}$. For the island + layer growth mode, $\gamma_{sg} > \gamma_{fs} + \gamma_{fg}$.

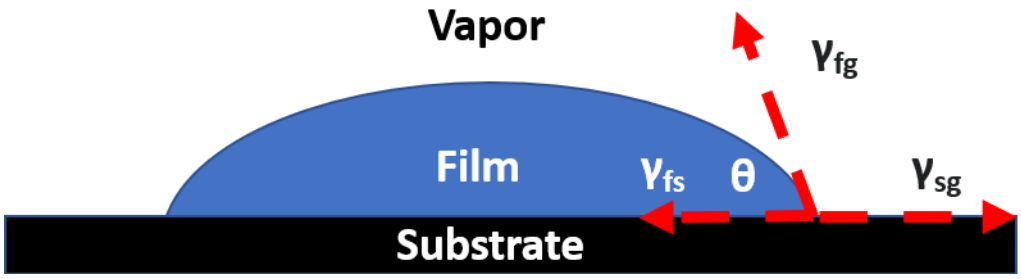

Figure 1.4 Schematic for Young's relation for surface tension and thin film nucleation.

1.2.2 Thin film epitaxy

The necessity for thin film epitaxy is generally a rule of thumb than a requirement. An epitaxial film will usually have matching relationship with the underlying substrate, inducing a single crystal out-of-plane direction that is measurable through techniques such as x-ray diffraction (XRD) and selective area electron diffraction (SAED). The epitaxial thin film, though, is not considered a true single-crystal due to high defect concentrations and in-plane grain boundaries that might exist. A treatment of the different types of epitaxial thin films can be found in section 1.1.1 and include coherent, semi-coherent, and incoherent films. In functional oxides, it is generally desirable for application to have an epitaxial thin film to control properties. Moreover, the sensitivity of oxide thin films to strain means that epitaxy provides a knob for tuning functional properties. For many oxides, the material in the bulk may demonstrate insulting properties but when strained in an epitaxial thin film demonstrate tunable metal-insulator transitions. Many oxide properties are directly tunable via lattice mismatch [16,17]. Lattice mismatch and specific strain engineering is achieved by substrate selection, with typical oxide substrates such as $SrTiO_3$ with cubic structure, $LaAlO_3$ with pseudocubic structure, and Al_2O_3 which has a hexagonal structure. Many of the thin film growth techniques deposit from a gaseous vapor, which have an inherent tendency to grow epitaxially. A discussion on the major techniques and other methods is presented below.

1.2.3 Sputtering

The sputtering technique is a well-established epitaxial thin film growth method and is used for large-scale production since it can develop uniform film growth on large substrates. The disadvantages of this technique are in the vacuum requirements, film thickness (> micrometers), and the line of sight deposition. The basics of sputtering include the ejection of atoms from a source material due to impinged energetic particles. An overview of the sputtering setup is shown in Figure 1.5. The target is mounted to face the substrate and an inert gas (usually argon) is introduced to the system at a certain processing pressure. A power supply is attached to the target, acting as the cathode (negative potential) and electrons will then be accelerated from the cathode. The electrons collide with argon gas molecules, inducing a weakly ionized gas (plasma). Ionized gas particles are then accelerated by an electric field across the target,

impinging on the target, creating a cascading collision effect that ejects target material towards the substrate (e.g. sputtering). The sputtered target atoms then come to condense on the substrate, causing thin film growth of the target material.

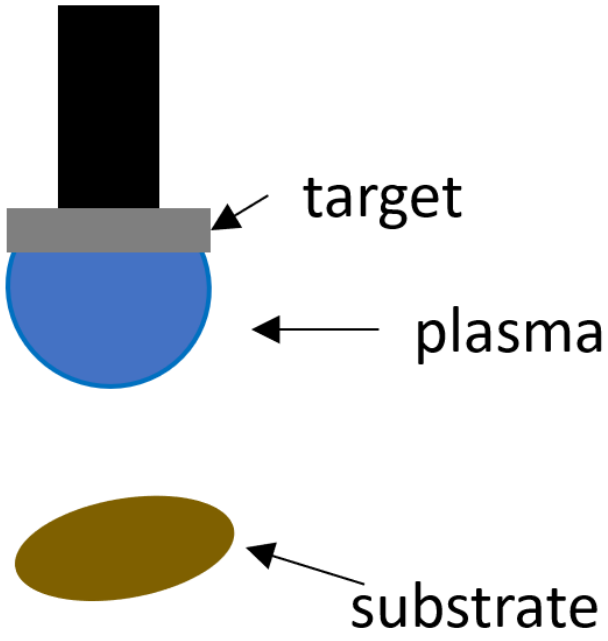

Figure 1.5 Sputtering schematic diagram.

Sputtering has been used to grow a wide-range of different oxides and is particularly useful for the growth of oxides for hard-coatings such as Al_2O_3. The great benefit of sputtering is its ability for uniform, large-scale thin film growth. The disadvantage is that growing complex oxides on a large-scale through the sputtering technique proves challenging to grow stoichiometric and uniform films. A standard system as outlined in Figure 1.5, backsputtering of O^{-2} ions occur and results in reduced film quality and physical properties. The backsputtering issue is the major disadvantage to overcome to realize large scale uniform growth oxide thin films. Sputtering at high pressures [18] and using dual parallel sputter guns to grow $Pb_{0.67}(Mg_{1/3}Nb_{2/3})O_{3-0.33}PbTiO_3$ (PMN-PT) and $BiFeO_3$ have all been proposed as methods for sputtering uniform, stoichiometric oxide thin films [19]. Both the PMN-PT and BFO systems are

sensitive to growth conditions, and the dual parallel sputter guns was shown as able to grow uniform stoichiometric films**.**

1.2.4 Pulsed Laser Deposition

Pulsed laser deposition (PLD) gained considerable attention as a technique for depositing high quality, epitaxial, stoichiometric oxides during the 1980s when it was used to grow superconducting $YBa_2Cu_3O_7$ (YBCO) films. Since then, it has become the most common technique within the oxide research community for thin film growth. The advantages that make this technique attractive are the almost congruent transfer of stoichiometry from target to substrate, high quality epitaxial films, and the ability to grow films in a high-pressure background gas. Disadvantages include the complex interplay of growth parameters, low film surface coverage, and potential high costs. One very attractive quality of PLD is as a relatively simple technique involving a laser beam and a target. A laser pulse is incident on the target, creates plasma plume ejection, which then condenses on a substrate and causes film growth. The parameters that are available for tuning growth during PLD are the target-substrate distance, laser fluence and frequency, substrate heating, and background gas composition and pressure.

Technique description

A schematic for a typical PLD setup can be seen in Figure 1.6. First, a target with composition of the film that is going to be grown is placed within a vacuum chamber on a rotating target holder. Then the chamber is pumped down to a base pressure of 10^{-6} mbar with a combination of mechanical and diffusion pumps. After chamber evacuation, a background gas can be introduced. For PLD growth of oxides, an oxygen ambient is commonly utilized though other gases are possible to use including argon, helium, and nitrogen [20,21] The substrate the film is to be deposited on is placed a distance anywhere from 3 to 5 cm parallel to the target. Careful selection of the substrate with similar crystal structure to the film is necessary if high quality epitaxial thin films are desired, otherwise films will have strain in their structure and can degrade properties [22]. Additionally, the temperature of the substrate is tunable up to 800°C, which will contribute to surface diffusion during film growth [23,24]. During PLD, ablation of the target surface takes place during a pico- [25], femto- [26], or nanosecond laser pulse by

either a KrF (248 nm) or XeCl (308 nm) ultraviolet excimer laser. The beam is focused at an angle of 45^{o} and incident on the surface of the target and the pulse has tunable frequency. Irradiation of the surface creates a plasma plume of ejected particles.

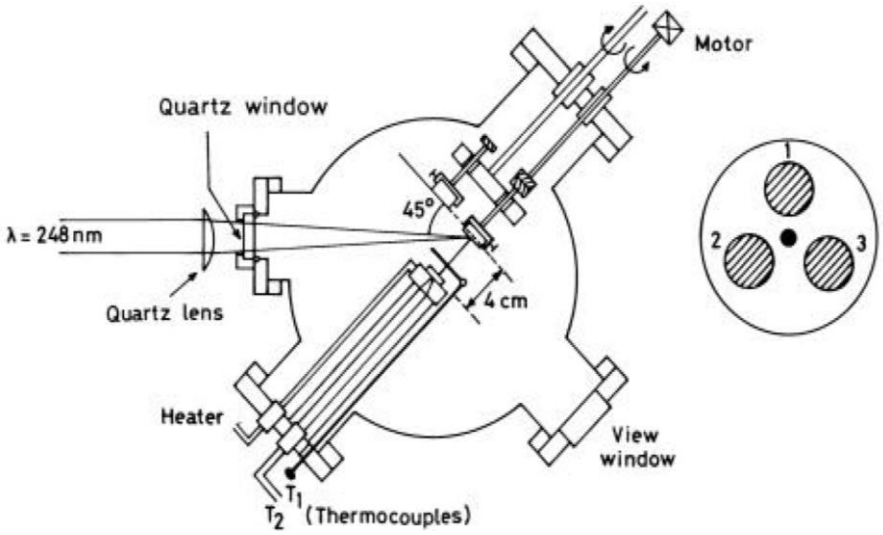

Figure 1.6 Schematic of typical PLD setup. Diagram obtained from [24].

Substrate growth temperature

The substrate growth temperature plays a critical role in controlling the nucleation and growth of oxide thin films during pulsed laser deposition. Four inequalities exist to describe the relationship between film growth rate $\dot{R}$ and substrate temperature based on critical nucleus size r^* and ΔG^*, the formation energy for critical nucleaus.

Assuming the following equation:

$$\text{Equation 3 } \Delta G_v = \frac{kT}{\omega} ln \frac{\dot{R}}{\dot{R}_e}$$

where k is Boltzmann's constant, T is the substrate temperature, ω is the atomic volume, $\dot{R}$ is the deposition rate, $\dot{R}_e$ is the equilibrium evaporation rate from the film nucleus at temperature T, and ΔG_v is the volumetric free energy. Assuming an inert substrate, the following inequalities can be derived:

$$\text{Equation 4 } \left(\frac{\partial r^*}{\partial T}\right)_{\dot{R}} > 0$$

$$\text{Equation 5 } \left(\frac{\partial \Delta G^*}{\partial T}\right)_{\dot{R}} > 0$$

$$\text{Equation 6 } \left(\frac{\partial r^*}{\partial \dot{R}}\right)_T < 0$$

$$\text{Equation 7 } \left(\frac{\partial \Delta G^*}{\partial \dot{R}}\right)_T < 0$$

The above inequalities can summarize most thin film nucleation and growth behaviors. From equation 4, high substrate temperatures will lead to an increased critical nucleus size and 3D island growth is expected to form a higher surface coverage than at low substrate temperatures. Equation 5 indicates a nucleation barrier exists for high substrate temperatures, where at low substrate temperatures it is reduced, and the number of critical nuclei will decrease with temperature. A continuous film will take much longer to grow at high substrate temperatures. From equation 6, increasing the deposition rate will result in smaller islands and a thinner continuous film will develop. In general, high substrate temperatures and low deposition rates yield high quality, single crystalline and epitaxial thin films. Conversely, low substrate temperatures and high deposition rates will yield polycrystalline and reduced epitaxial films.

In PLD depositions, substrate temperature tuning is very commonly studied and has been demonstrated for a wide range of systems. Ga-doped ZnO has been investigated, showing that as the substrate temperature is increased the film crystallinity improves as well as the optical and electrical properties [27]. In ZnO films, a similar effect was also observed [28] along with an increase in particle size.

Laser frequency and fluence

The laser frequency affects the number of pulses incident on the target while the laser fluence determines the energy density of each laser pulse. The laser pulse allows for non-equilibrium instantaneous growth and is only limited by the frequency of the laser. In general, lower repetition rates will allow for the formation of smooth surfaces since the nuclei will have more time for ripening. A pulsed kinetic Monte Carlo (PKMC) model was used to study the role of laser frequency in pulsed laser deposition film growth and microstructure. [29]. As frequency is increased, the film nucleus ripening is decreased and the time to find a thermodynamically favorable spot, which subsequently leads to a less smooth and strained film. In the PKMC models, it was found that laser repetitions of f = 1000 Hz led to large island densities and

smallest island size while frequencies of f = 10 Hz led to the largest island size and smallest island density. The PKMC film morphology simulations are shown in Figure 1.7

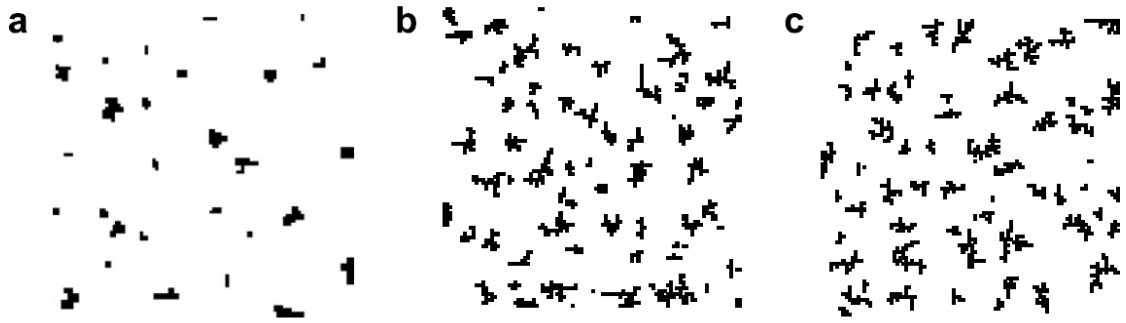

Figure 1.7 PKMC film morphologies for different laser frequencies. A) 10 Hz, b) 100 Hz, and c) 1000 Hz. Adapted from [29].

Target and laser interactions

Critical to PLD is the laser-target interaction. This is a complex thermodynamic process that involves conversion of the high energy laser pulse to kinetic energy in the plasma plume of ejection materials. It is possible to tune the kinetic energy and expansion dynamics of the plasma plume by PLD parameters including background gas pressure and composition [21,26] substrate heating [30], and laser fluence ($\frac{laser\ energy}{laser\ spot\ size}$ [eV/cm^2]) [31].

During laser ablation, first the energy of the laser pulse is absorbed by the target surface which causes melting and vaporization. Vapors build up on the target surface induces plasma ignition by way of an explosive phase change and a plume is created consisting of neutral atoms, ions, electrons, molecular ions, free radicals, and micron size clusters [32]. The plume partially absorbs some of the heat from the target surface and then is accelerated to hypersonic velocities toward the substrate where condensation creates thin film growth [32,33]. This process is summarized in Figure 1.8.

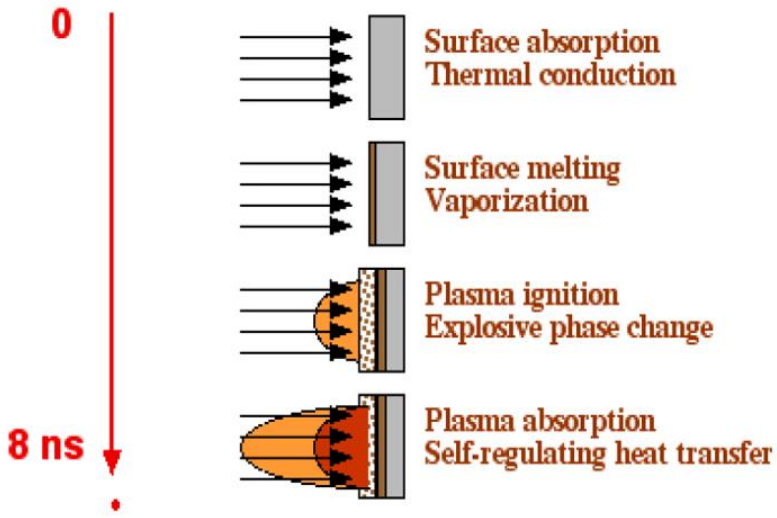

Figure 1.8**:** Summary of the laser-target interaction for a nanosecond laser pulse ablation. Obtained from [32].

Tracking of plume expansion dynamics is possible by in-situ characterization of emissions from the visible spectrum. Techniques for this purpose include laser induced fluorescence spectroscopy [34] and wavelength-dispersed emission spectroscopy [35]. A representative emission spectrum is shown in Figure 1.8. The problem with current methods of in-situ characterization is that they only track emissions in the visible spectrum and a complete story of expansion dynamics may be untold. Experimental elucidation is critical for oxide growth because the plume directly affects the film stoichiometry and morphology as discussed in the below sections following. While numerical and analytical methods have been produced to describe expansion dynamics, they cannot model the chemical reactions that occur between the oxygen background gas and plasma plume, which is important in understanding film stoichiometry tuning.

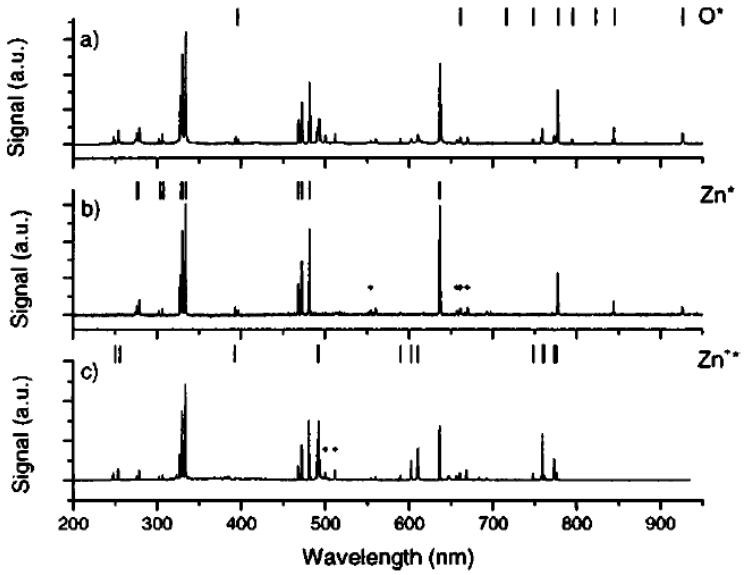

Figure 1.9**:** Typical emission spectra for laser ablation of ZnO showing neutral Zn and O, and positive Zn^+ ions. Produced by wavelength-dispersed optical emission spectroscopy. Obtained from [35].

Numerical and analytical models to describe background pressure and plasma plume interactions

Different analytical and numerical methods have been developed to describe the governing mechanisms of plume expansion. The literature discusses three characteristic pressure regimes based on background-gas plasma plume interactions: an adiabatic low-pressure expansion regime, shockwave propagation transitional regime, and a ballistic blast wave high pressure regime. Examples of the different regimes are shown in Figure 1.10

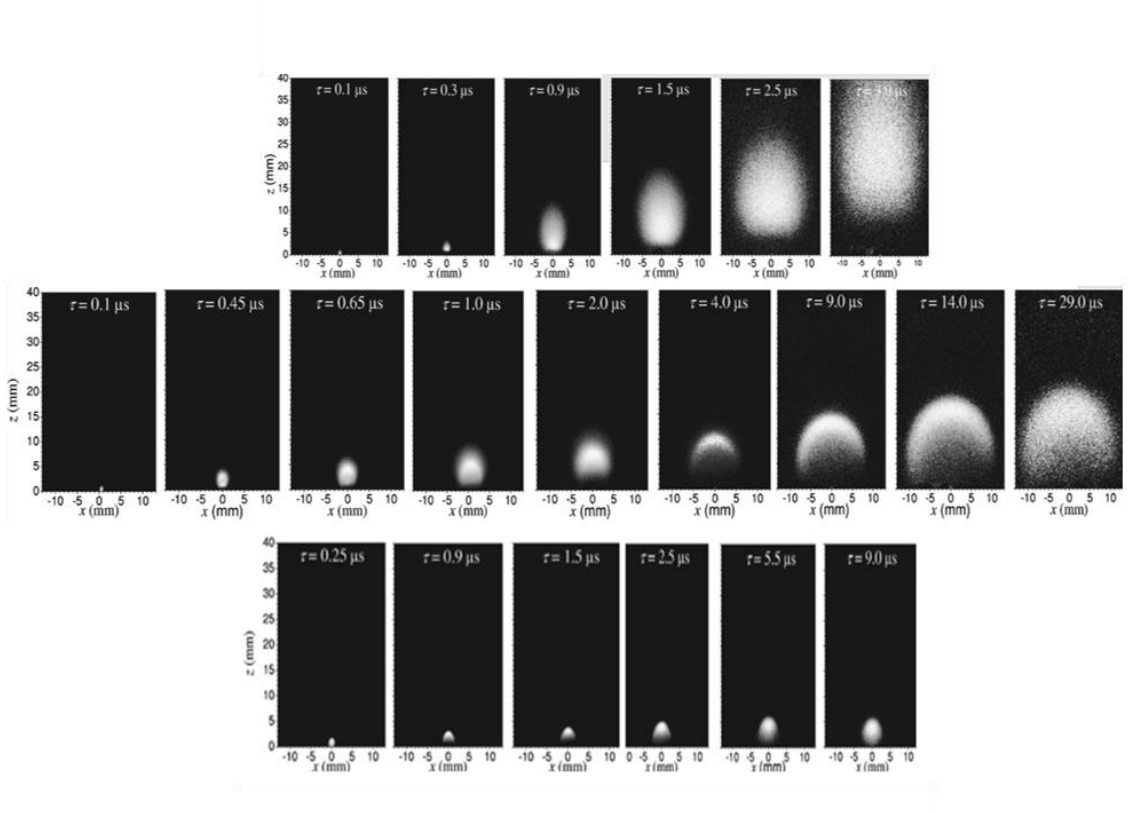

Figure 1.10 ICCD Fast photography images of a $LaMnO_3$ laser ablation plume for three pressure regimes. Top panel is representative of vacuum up to 10^{-3} mbar. Middle is representative of moderate pressure regimes 10^{-2} – 10^{-1} mbar. Bottom panel demonstrates complete stopping of plume in elevated pressures up to 3 mbar. Obtained from [36].

In low pressures, the background gas and plasma plume do not interact [36]. Therefore, plume expansion can be described by adiabatic processes and modeled by gas-dynamic equations [20,37] At the transitional regime, plasma expansion can be described through diffusion laws, where ablated particles are thermalized in collisions with the background pressure [37]. In this regime, breaking and confinement effects and deceleration of the plume are noticeable. This is demonstrated in the spherical shape of the plume seen in the middle diagram of Figure 1.10 compared with the low-pressure plume in the top row of Figure 1.10. Propagation in this regime is characterized by shockwave oscillations, which leads to strong gas-plume intermixing at the periphery of the plume [21]. This regime can also be described with an analytical model for shockwave propagation [20]. At high pressures, complete stoppage of the plume is observed and particles in the plume reach the substrate by diffusion through the background gas [36,37] In this regime, the plume expansion dynamics are discussed in terms of

a “blast-wave” model. Above a certain threshold background pressure, the snowplow effect will occur [21,36]. The plasma plume will push away the background gas but the background gas will be unable to fill the space behind the gas.

To simplify analysis of the regimes, several general models have been developed to describe all three expansions of the plume. These models include a spherical expansion model based on laws of mass, momentum, and energy conservation [38], a two-fluid gas-dynamic model with an analogy to an underexpanded jet [39], and a combined-continuous kinetic model that utilizes a hybrid of the method of large-particles and direct monte carlo simulations [40]. Of these models, the combined continuous model developed by Itina et al can be applied in all three regimes and describe complicated plume-gas interactions. The other models in their simplicity are unable to describe plume-gas effects, especially gas-mixing and the initial plume expansion [38], and breakdown at the moderate transitional regime. The importance of the model is that it can be applied in vacuum up to high pressures and can accurately elucidate complicated behaviors at the transitional moderate pressure regime. With the model such phenomena as plume deceleration, snowplow effect, and plume-gas mixing can be investigated.

Oxidation of the plasma plume by a reactive oxygen background gas

The limitation of numerical and analytical methods like the combined-continuous model are the inability to describe the chemical reactions that occur between an oxygen background gas and the plasma plume. Numerical and analytical models neglect this interaction by assuming the plasma plume expands into an inert background [30,36,41,42]. Oxidation of the plasma plume is believed to determine film stoichiometry for oxide thin films [30,43] and optimization of the oxygen background gas could lead to precise growth of oxide films with engineered properties.

Plume and oxygen background gas interactions

Oxidation of the plume occurs by two mechanisms. The first is creation of oxygen ions by recombination effects between oxygen molecules in the background gas and electrons in the plasma plume. The second mechanism is caused by superheating in the compressive layer formed by the gas and plasma plume due to breaking and confinement of the plume by the background gas [44], leading to ionization of molecular oxygen in the background gas. Based

on expansion dynamics, location of highest oxygen stoichiometry in the plume will be different. Figure 1.11 shows density maps of ground state AlO species produced during laser ablation of aluminum in an oxygen ambient. Low pressure regime is not shown because the plasma plume is not oxidized in these pressures. At the transitional regime, oxidation occurs at the periphery of the plume because of vorticial flows and strong intermixing caused by diffusive processes [40]. At high pressure, due to the snowplow effect, oxidation occurs at the plume front. Mapping species formation could provide a possible tool for optimizing oxygen content in the film by preferentially placing the substrate in a location of the plume that has highest oxygen content.

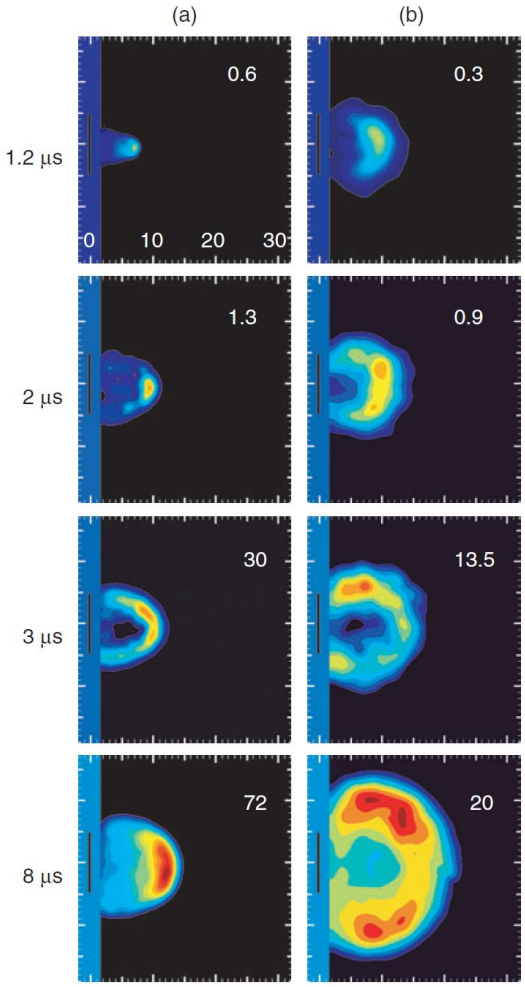

Figure 1.11**:** Density maps of ground state AlO constituents formed during laser ablation of aluminum in different oxygen pressures, obtained by laser induced fluorescence spectroscopy. a) 70 Pa, ballistic regime b) 13 Pa, transitional regime. Obtained from [45].

Oxygen film stoichiometry tuning

Increasing background pressure during pulsed laser deposition will increase oxygen content in the film [22]. This trend is shown for an aluminum oxide film in Figure 1.12. Films of Al_2O_3 deposited in low pressure are oxygen deficient because of preferential ablation of lighter species [46]. As oxygen pressure is increased, films become oxygen rich due to preferential scattering of lighter species [47] and oxidation of plasma constituents. Oxidation of the plasma plume will increase with increasing background pressure, shown for $LaAlO_3$ in Figure 1.13. As pressure increases, LaO species emissions increase because of elevated oxidation. The background could be therefore used as a tool for oxygen compensation in PLD of oxide films. The issue arises that as background pressure increases, film morphology transitions from smooth to columnar, demonstrated in the density variation shown in Figure 1.12.

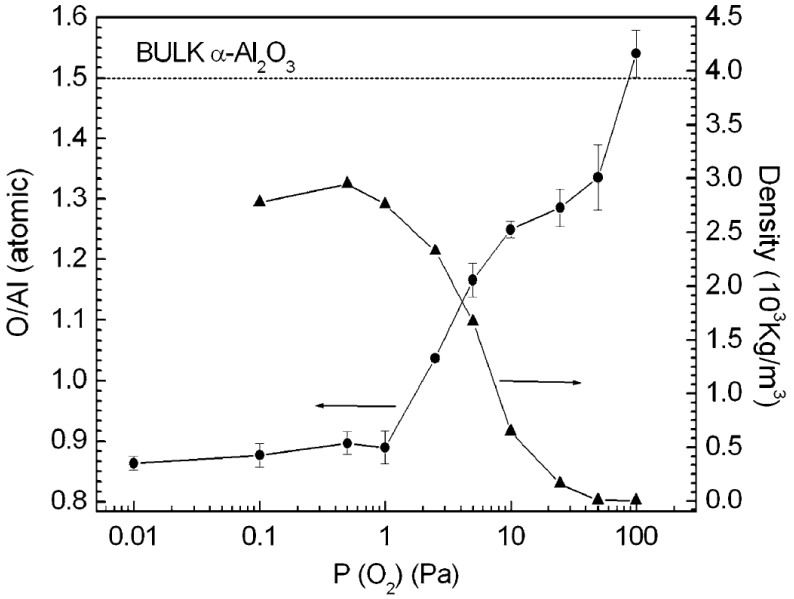

Figure 1.12: O/Al calculated by EDX and density pressure dependence for Al_2O_3. Obtained from [48].

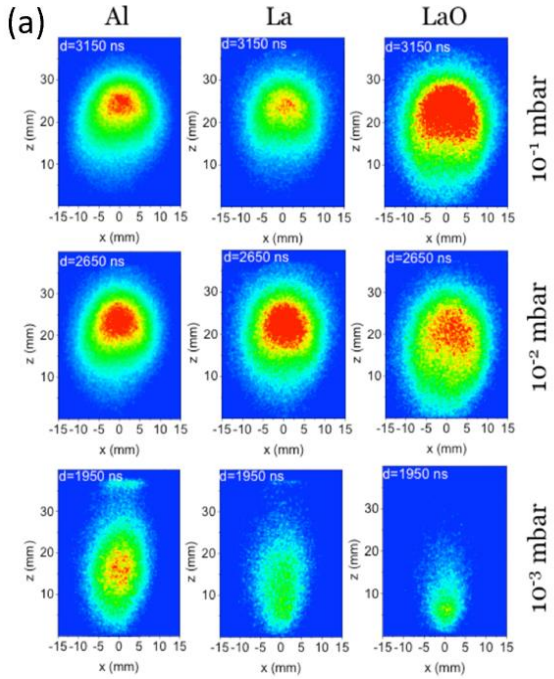

Figure 1.13**:** 2D optical emission images of single species plume approaching the substrate for a $LaAlO_3$ plume at for three different background pressures. Obtained with permission from [46].

Film morphology control

The three different expansion regimes will produce three different film morphology. Examples of the film morphologies are shown in Figure 1.14 and demonstrated in the literature for Al_2O_3 [48], yttria-stabilized zirconia (YSZ) and gadolinium-doped cerium oxide (CGO) [49], and aluminum-doped zinc oxide (AZO) [50].

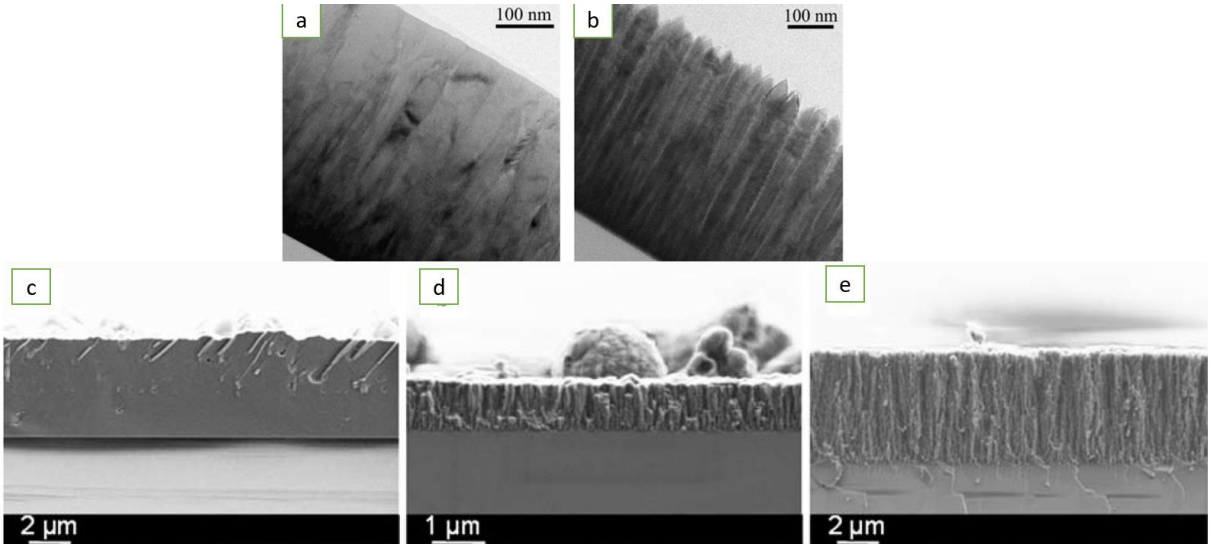

Figure 1.14 TEM micrographs of YSZ films deposited at a) and b). SEM images of aluminum oxide films deposited at c) d) e). Obtained from [48,49].

In the low-pressure regime, smooth and oxygen deficient films can be grown with high density seen in Figure 1.14c. At the transitional growth, films will have columnar growth with variable density seen in Figure 1.14d. Growth in high pressures will have open, porous microstructure seen in Figure 1.14e. Film morphology tuning can lead to tailored applications of oxide films. Based on the microstructure of aluminum oxide, the film can be utilized in different applications, where the smooth film seen in Figure 1.14c can be used for a hard surface coating and the porous microstructure seen in Figure 1.14e can be applied as a support for catalysts because of its high surface area. The advantage of PLD is that it allows for growth of different types of film morphology based on background pressure tuning. To achieve this before in Al_2O_3, different deposition techniques were necessary.

The columnar structure will transition towards a nanorod like growth that has spacing between the grains with increasing background pressure, which is demonstrated in Figure 1.15 for Al-doped ZnO. The diameter of these nanorods can be increased via increasing background pressure. A consequence of the transition from smooth to nanorod growth is the tunability of surface roughness of the films. This is demonstrated for AZO [50] and YSZ [51] and highlighted in Figure 1.16.

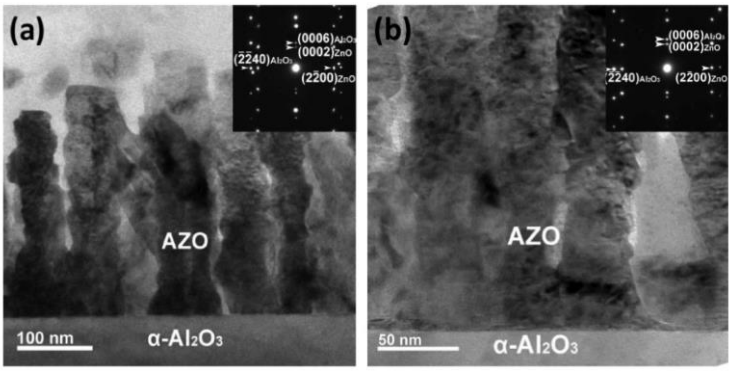

Figure 1.15**:** Cross-section TEM micrographs of AZO grown at a) 250 mtorr and b) 100 mtorr. Obtained from [50].

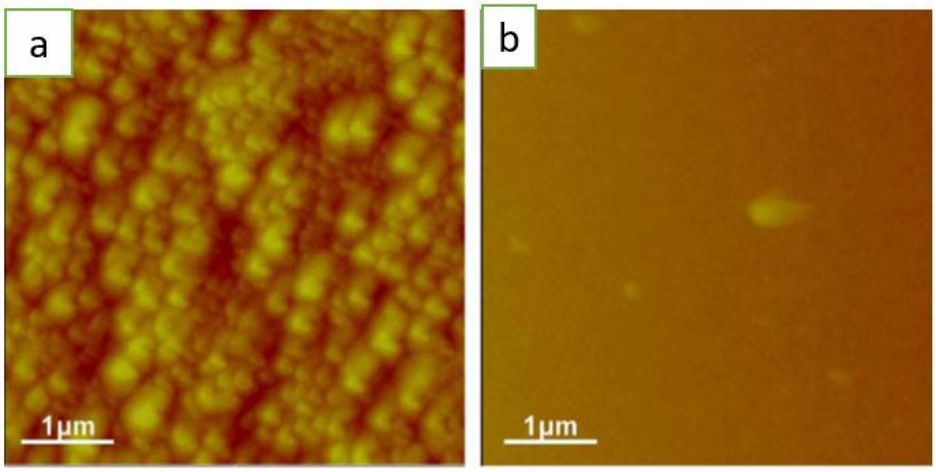

Figure 1.16**:** Atomic force microscopy (AFM) images of AZO grown at a) 250 mtorr and b) 50 mtorr. Obtained from [50].

Since the nanorods will tend to grow apart with intergranular spacings, this will cause the properties of films to become highly anisotropic in the direction of the nanorod's growth. Therefore, the properties of these oxide films are dominated by their microstructure. This explains the increased in-resistivity for AZO seen in Figure 1.17a. The optical properties will also be affected by the surface roughness and the nanorod growth, demonstrated in the widening of the absorption edge in Figure 1.17b. Joon Hwan Lee et al take advantage of this microstructure and property tuning in AZO to grow a bilayer film consisting of the nanorod film grown on top of the smooth film for solar cell applications, as seen in Figure 1.17c. It maintains

the electrical conductivity of the smooth layer while taking advantage of the light trapping capabilities of the nanorod structure.

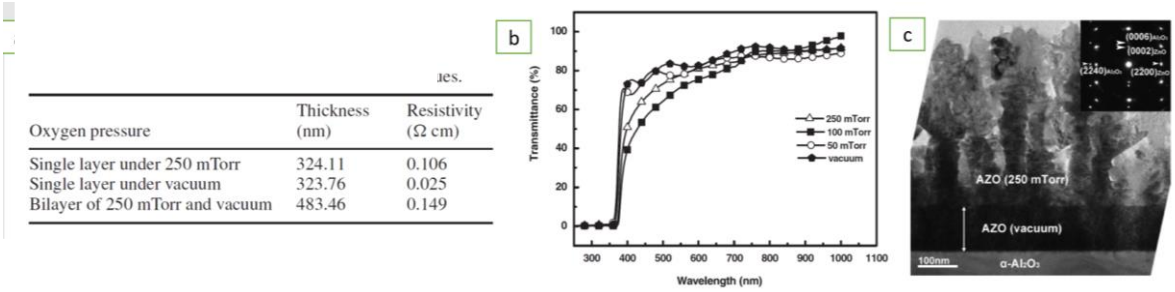

Oxygen pressure	Thickness (nm)	Resistivity (Ω cm)
Single layer under 250 mTorr	324.11	0.106
Single layer under vacuum	323.76	0.025
Bilayer of 250 mTorr and vacuum	483.46	0.149

Figure 1.17 a) table of resistivities for AZO films deposited at different background pressure. b) transparency of films for different background pressures. c) bilayer of AZO. Obtained from [50].

To explain the variation in microstructure with the background pressure as observed in Figure 1.14, F. Di Fonzo et al. proposed an empirical scaling law for Al_2O_3 based on the pressure and the target-substrate distance [48]. Both scales together because they influence the kinetic energy of impinging species, and therefore, the energy available for surface diffusion. A. Infortuna et al. plotted a structure zone map for CGO and YSZ films based on their experiments to describe microstructures produced during PLD [49]. To explain the structures formed at different background pressures, it is important to consider two mechanisms.

The first mechanism is energetic surface smoothing developed by P.R. Willmott et al. This process is summarized in Figure 1.18. Particles impinging at low coverage (red) will nucleate small, dense islands (purple) for very small surface coverage. If their kinetic energy is high enough and they land on top of other nucleated species, they will split the islands to form daughter islands (green). Therefore, density of small islands will increase until coverage is ~ 50% monolayers and begin to cause coalescence. From here, impinging atoms must diffuse to descending step edges, which is accelerated by kinetic energy of impinging atoms and coupled to the mobility of diffusing adatoms. For film coverage greater than a single monolayer, the impinging species will not be able to break up the 2D growth. Instead, they will impinge, and their kinetic energy will contribute to local surface diffusion for sustained 2D growth. This model holds for species with kinetic energies on the order of 10 – 100 eV. If they have kinetic energy lower than 10 eV, they will not be able to break up islands and cause coalescence. If they have a kinetic energy that is too high, they will impinge and cause defects [52]. Continued 2D

growth at low pressure is also caused by re-emission effects, whereby species will bounce off nucleating hills on the film and preferentially deposit in the valleys between the hills [53].

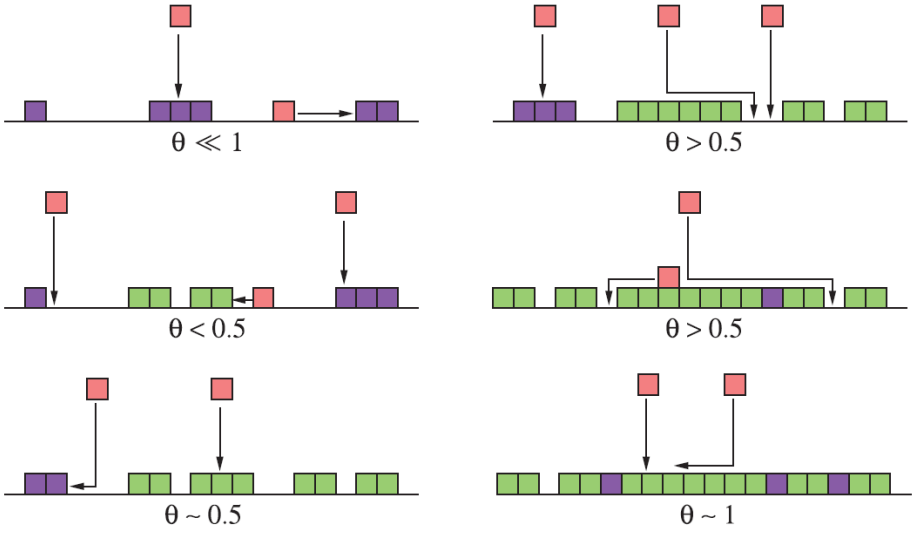

Figure 1.18**:** Kinetic model to describe long term 2D growth at low pressures. Obtained from [52].

The second process that explains nanorod like growth at high pressures is unique to the pulsed laser deposition process, which is formation of stable clusters inside the plume during expansion [54,55]. Clusters form as a side effect of the initial ablation [24, 43] and can potentially become ionized inside the plasma plume [32], attracting other plume constituents. As background pressure is increased, mean free path is decreased inside the plume and more collisions will occur. This can cause the clusters to become bigger as they collide and stick to other particles, which potentially explains the tunable nanorod size and surface roughness seen in [50]. Another factor contributing to the columnar growth is a reduction of the kinetic energy. Table 1 shows a summary of maximum kinetic energies for species in $LaOAl_3$. As pressure is increased, the maximum energy drops below the 10 eV threshold necessary for energetic smoothing and 2D growth [52]. Another contribution to the nanorod and columnar growth is shadowing effects [53], whereby large clusters will preferentially nucleate on hills growing on the film.

Table 1.1 Maximum kinetic energy (eV) for different background pressures (mbar) in an $LaAlO_3$ and $LaGaO_3$ system. Obtained from [56].

Species	$10^{-6}-10^{-3}$	10^{-2}	10^{-1}
Al	14 ± 0.2	14 ± 0.2	0.1 ± 0.02
Ga	35 ± 0.2	35 ± 0.2	0.4 ± 0.02
La	58 ± 0.2	55 ± 0.2	0.7 ± 0.02
LaO	52 ± 0.2	52 ± 0.2	0.8 ± 0.02

1.2.5 Molecular Beam Epitaxy

Molecular beam epitaxy (MBE) is a vapor deposition technique that allows for the control of atomic vapor arriving to the growing film. Usually, MBE is coupled with some kind of monitoring system such as reflective high energy electron diffraction (RHEED) to control the surface termination and the flux of incident cations. A typical setup is shown in Figure 1.19. The benefit of the MBE approach is in precise, stoichiometric control of complex oxide growth, remarkably for the growth of well-ordered and stoichiometric layers with abrupt interfaces and interface chemistry control [57]. Many systems that might be unstable in the bulk can be grown in MBE systems as epitaxial heterostructures [58,59].

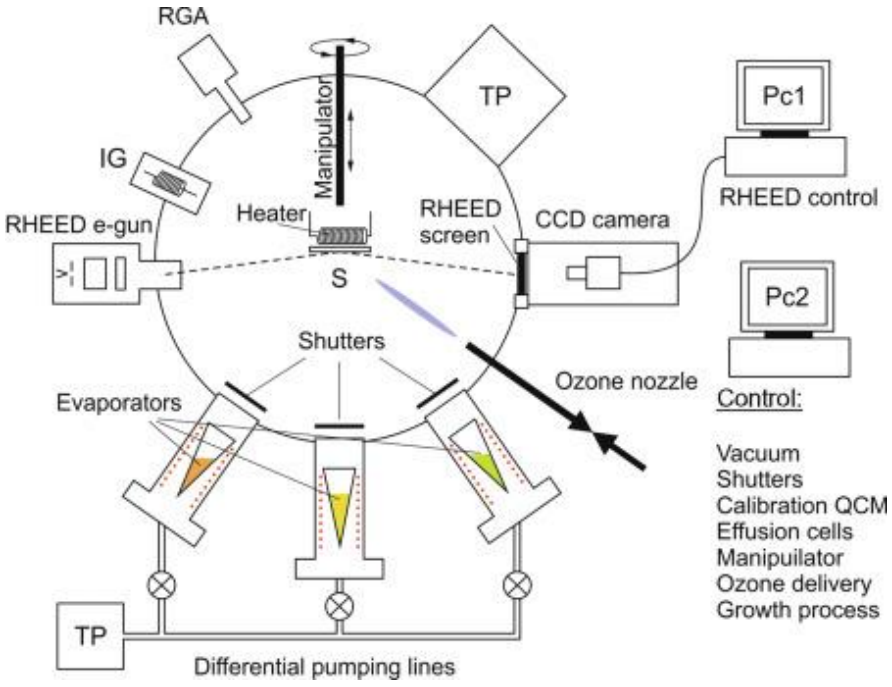

Figure 1.19 Top view schematic of an MBE system. Obtained from [60]

1.2.6 Other methods

Other methods for the development of oxide thin film include chemical processes such as sol-gel synthesis or electrodeposition. These are useful for growth of nanowires and nanoparticle structures. In the sol-gel process, a colloidal solution is formed that is evolved towards a liquid and solid phase with specific morphology. Solid phases are separated either through centrifugation or through a drying phase. The drying phase is then followed by a firing phase to ensure densification, structural stability, and grain growth. Typically, in the thin film growth the initial sol is deposited onto a desirable substrate. A schematic representation of the sol-gel process is depicted in Figure 1.20. Sol-gel processing has been used significantly to develop metal oxide nanoparticles with tunable particle size, with the advantage being the relatively low processing temperatures, cost-effectiveness, and controllable fine nanostructures [61]. The ZnO system has been greatly studied through the sol-gel method in application for anti-corrosive coatings and as electrodes for supercapacitors [62]. Moreover, the sol-gel method provides a platform for achieving plasmonic metal (Ag, Au, Cu, etc.) and oxide nanocomposites [63].

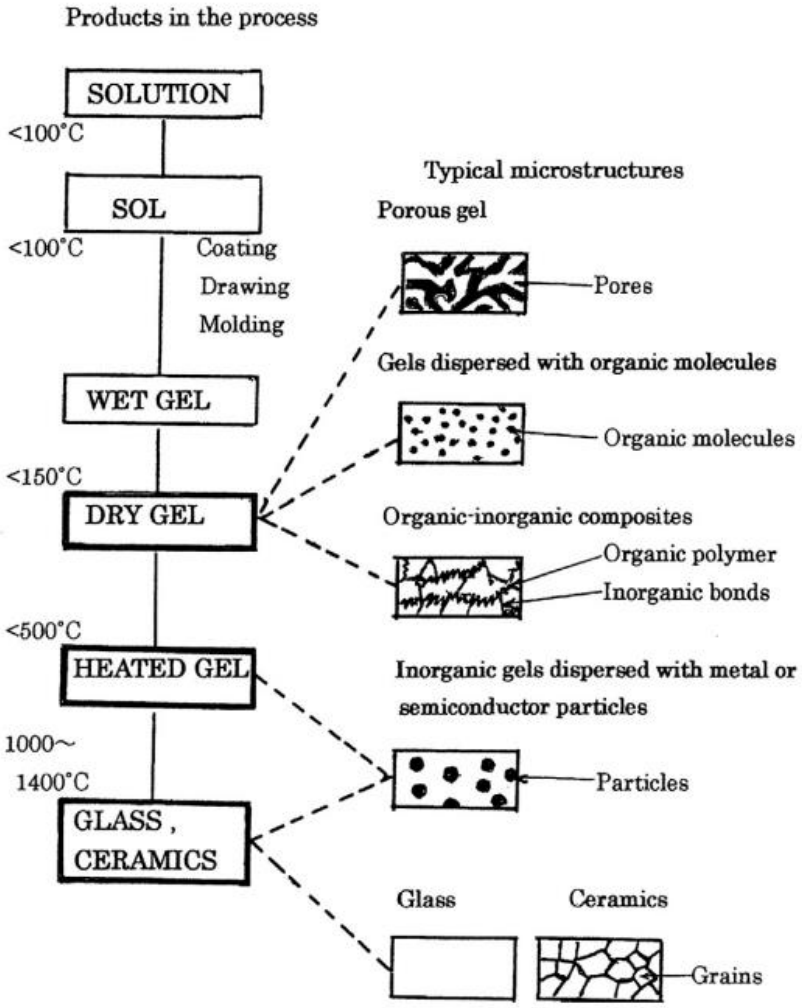

Figure 1.20 Sol-gel process steps and microstructure at each step. Adapted with permission from [64]. Copyright 2001. American Chemical Society.

Electrodeposition is another efficient and low-cost method for fabrication of oxide thin films and coatings. The process is based on electrochemical phenomena whereby the reduction of electroactive species causes deposition on a cathode surface. In a simple setup, an anode and a cathode are submerged in an electrolyte solution containing ions of the material that is desired to be deposited, e.g., an electrolytic cell. An external force (either current or voltage) is applied, causing a reduction reaction and in controlled conditions, the redox reaction leads to formation of an electrodeposit on the cathode. The fundamental redox reaction for electrodeposition of ZnO is based on the precursor of OH^- which is accompanied by reactions with Zn^{2+} according to the following equation: $Zn^{2+} + 2OH^- = Zn(OH)_2$ [65]. The zinc hydroxide formed is transformed at

elevated temperature into zinc oxide: $Zn(OH)_2$ -> $ZnO+H_2O$. ZnO thin films deposited from electrodeposition can be attached to a wide range of 2D and 3D structures, such as conductive meshes and foams for use in anodes or onto titanium alloys for use as anti-bacterial coatings [66,67].

1.3 Zinc Oxide thin films

1.3.1 Structure and properties

ZnO-based nanostructures and thin films have gained widespread interest for applications for electronics, optoelectronics, biomedicine, energy-harvesting, and sensing owing to the unique properties of ZnO. This interest in ZnO-based thin films and nanostructures is due to the different functionalities including piezoelectric, optical, magnetic, catalytic, electrical, and gas-sensing properties [68] Moreover, due to the easy growth of ZnO and low processing temperatures, it boasts a plethora of nanostructures including nanorods, nanotubes, nanowires, and nanoribbons [69]**.** ZnO also has an excitonic binding energy of 60 meV, making it ideal for light emission applications in the UV range [70,71]. ZnO is a direct wide intrinsic n-type semiconductor with a bandgap of around ~3.37 eV [70]. The bandgap combined with high conductivity make ZnO interesting for application in transparent conducting oxides and thin-film transistors [68,72]**.** A table of common properties for ZnO is presented in Table 1.2.

Table 1.2 Structure and properties of ZnO . Values obtained from [71,73,74]

Property	Value
Bandgap	3.37 (direct)
Density	5.606 g/cm^3
Crystal structures	Wurtize, rocksalt, zinc blende
Stable structure 300K	Wurtzite
Melting point	1975^{o}C
Lattice constants	a = 0.3245 nm, c = 0.5207 nm.
Dielectric constant	8.66
Refractive index (n)	2.0041
Intrinsic carrier concentration	10^{16} to 10^{20} cm^{-1}
Breakdown voltage	5.0 x 10^6 v/cm^{-1}
Exciton binding energy	60 meV
Electron hall mobility at 300K	200 cm^2/Vs
Hole hall mobility at 300K	5-50 cm^2/Vs
Ionicity	62%
Intrinsic carrier concentration	Max p-type doping ~ 10^{17} cm^{-3} Max n-type doping ~ 10^{20} cm^{-3}

One of the most interesting aspects of ZnO is its rich defect chemistry despite its simple chemical formula, [75] which is often overlooked but important in the context of novel application. ZnO is an intrinsic n-type semiconductor and defect chemistry arises due to off-stoichiometry of either oxygen vacancies (V_o) or Zn interstitials (Zn_i). The descriptions are based

on Kroger-Vink notation, where i = interstitial site, Zn = Zinc, O = Oxygen, and V = Vacancy. Kroger-Vink notation describes defect chemistry of atomic sites where the superscript indicates charge, the prime refers to negative charge, the dot refers to positive charge, and an "x" or cross indicates zero charge. The donor defects present in ZnO are $Zn_i^{\cdot}$, $Zn_i^{\cdot\cdot}$, Zn_i^{x}, $V_o^{\cdot\cdot}$ and, $V_O^{\cdot}$, while the acceptor defects are $V_{Zn}^{\prime}$, and $V_{Zn}^{\prime\prime}$. The defect ionization energies range from 0.05-2.8 eV [76]. **.** A schematic of the conduction band for ZnO with different defect ionization is given in Figure 1.21. Zn vacancies result in an acceptor sites while oxygen vacancies and zinc interstitials result in donor levels. There is great debate within the community whether vacancies or interstitials dominate [68,73,75,76]**.** Many of the applications of ZnO rely on the rich defect chemistry, so a deep understanding is necessary to control properties. Moreover, doping with aliovalent ions to achieve p-type doping for application in p-n junctions is based on a balancing of extrinsic doping and intrinsic doping defect concentration [68,69,74]. Achieving p-type conductivity in ZnO proves difficult due to the defect chemistry. Shallow acceptor sites tend to be compensated by the presence of deep level donors in the conduction band, preventing p-type conductivity [77,78], as seen in Figure 1.21.

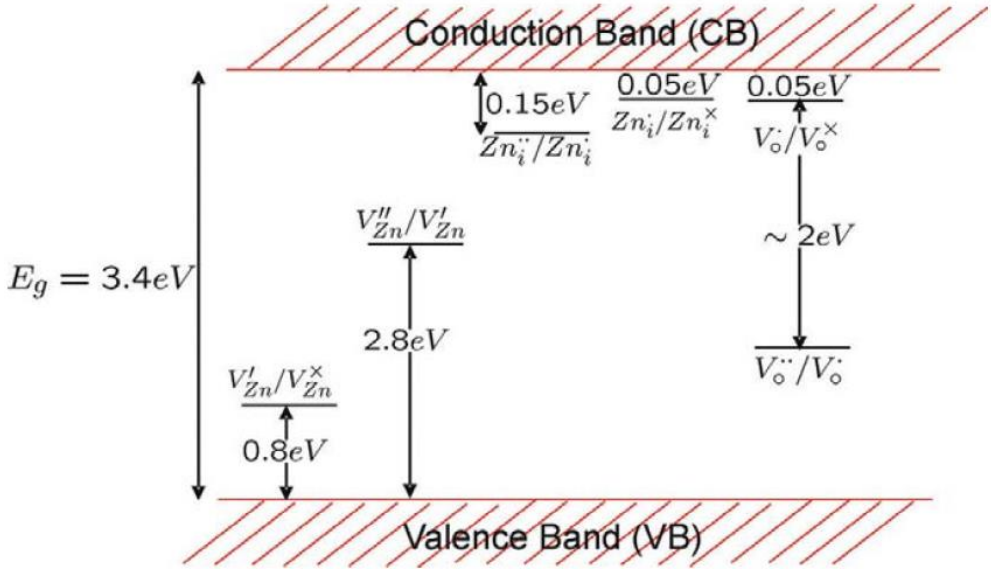

Figure 1.21 Electronic band structure of ZnO. Obtained from [1].

1.3.2 Application of zinc oxide thin films

Many of the properties outlined in Table 1.2 make it promising for a wide-range of applications. ZnO has been considered as an alternative in transparent conducting electrodes (TCOs) for the currently used indium tin oxide (ITO). TCOs play an important role in displays and solar cells and the advantage of ZnO over ITO is the widespread availability and cheaper cost [7]. High quality ZnO is processable at low temperatures and compatible with polymer and glass substrates [8,79–81]. ZnO conductivity is much less than ITO, but this can be overcome and improved by doping with elements such as Al, In, and Ga [7,27,82]. These doping constituents combined with a porous and conductive surface have also amended the use of ZnO in gas sensors [83]. ZnO also reports biocompatibility, non-toxicity, and antibacterial properties making it a promising choice for biosensors [84].

ZnO possesses both a high exciton energy and wide bandgap, making it a candidate for use in blue and UV LEDs. ZnO is much more cost effective and more available than the currently used GaN but the lack of reliable and stable p-type conductivity limit its use in homoepitaxial p-n junctions [85]. Heteroepitaxial p-n junctions, e.g. growing ZnO on p-type materials, has been widely reported as an alternative route for LED based ZnO devices [86,87]. Due to the wide bandgap and excitonic binding energy, ZnO is also ideal for use in semiconductor laser diodes [85]. Many of the current blue and UV lasers are based on GaN, which has an exciton binding energy of 25 meV [88]. The limit in laser diodes of ZnO has been due to the instability of reliable production of p-type conductivity [89]. The wide bandgap of ZnO also makes it a promising photodetector for UV rays for use in space applications and communications [90]. Moreover, ZnO is both thermally and chemically stable making it a robust material for use in military and civilian based photodetector application. It is also possible to tune the bandgap of ZnO with dopants In, Al, and Mg to make a photodetector for specific wavelength regimes [90,91]. ZnO also exhibits very strong radiation hardness, which is important for space applications. [92,93]

Another interesting aspect of ZnO is its ability to achieve ferromagnetic properties by doping with transition metals, making it a dilute magnetic semiconductor (DMS). In a dilute magnetic semiconductor, transition metal ions are partially substituted into a main group cation in both zinc blende and wurtzite semiconductors [94]. When grown as thin films, DMS can achieve electrical manipulation of their magnetic properties, or the reverse of magnetic

manipulation of their electrical properties and the possibility of spintronic devices becomes possible [95]. ZnO is particularly interesting for use in DMS due to its wurtzite structure and the equilibrium solubility of Mn^{2+} and Co^{2+}, two transition metals, approaches 10% at processing temperatures of up to 800^{o}C [96]. Interestingly, the dilute ferromagnetic properties in ZnO have been predicted through simulations [97], yet the experimental realization has proved challenging. Long range magnetic order has been found in a breadth of systems [96,98], but there is still ongoing debate as to whether it is ferromagnetic ZnO or the formation of dopant magnetic nanoparticles embedded into the ZnO [98].

1.4 Vertically-aligned nanocomposite thin films

1.4.1 Nanocomposite thin films

Oxide thin films have benefitted greatly from the advancement of deposition techniques such as PLD and MBE, allowing for precise control of growth almost atom by atom. Many of the functional oxide thin film properties can be coupled into crystalline or amorphous nanocomposites to allow for enhanced functionalities. Multilayers of oxides have demonstrated 2D electron gasses at the interface of $LaAlO_3/SrTiO_3$ [99]. Oxides with embedded plasmonic metal nanoparticles benefit from the localized field enhancement to improve optical properties [100–102]. Moreover, multilayers of plasmonic metal and oxides have demonstrated hyperbolic metamaterial properties, capable of subdiffraction imaging [103]. More recently, a new class of vertically-aligned nanocomposite thin film has emerged as a platform for achieving coupled functionalities [104–108]. In the two-phase VAN thin film, two immiscible phases grow epitaxially on a specific substrate to form pillars of one phase in the matrix of the second phase [109]**.** The benefit of the VAN over other nanocomposite is the one-step self-assembly through the pulsed laser deposition technique and the wide-range of materials selection. Moreover, the vertical interface allows for a unique vertical strain tuning not present in other nanocomposite thin films and the ability to overcome strain relaxation due to critical film thickness [107,109,110]. Typical examples of different nanocomposite are shown in Figure 1.22.

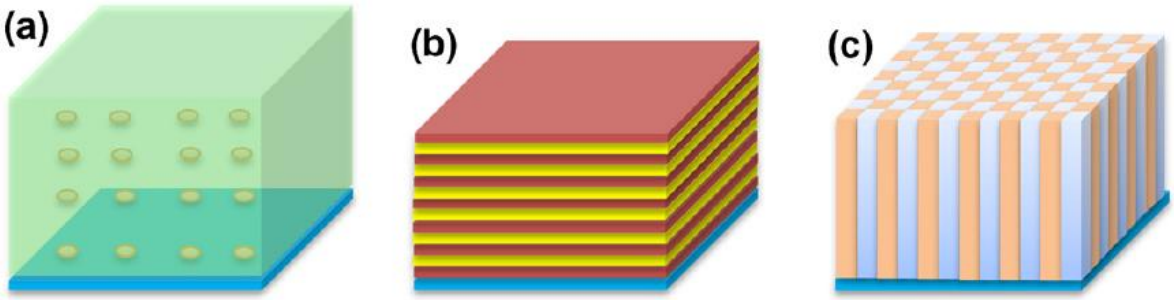

Figure 1.22 Types of nanocomposite thin films a) Particle in matrix. b) multilayer composite. c.) vertically aligned pillar in matrix composite. Adapted from [107].

1.4.2 VAN Growth

The VAN growth and ultimate microstructure is governed by total free energy minimization and a balance of processing parameters [106,111–114]**.** Deposition parameters such as oxygen pressure, substrate temperature, coarsening rate, and film thickness all effect the resulting microstructure. The substrate orientation, lattice parameter, crystal structure, and surface energy all determine the morphology of the nanopillars. And in the case of materials selection, the ratio of the two phases, the lattice mismatch and interfacial/elastic energy all help to determine the end microstructure [105,115]**.**

VAN growth is believed to follow a similar growth mechanism as single phase oxides [107,116], which is schematically represented in Figure 1.23, e.g. a three step growth mechanism. Initially, pulse laser ablated species arrive to the substrate surface and are adsorbed. Adatoms then undergo surface diffusion to minimize free energy of the system and find the most energetically favorable spot. Second, nucleation will occur, and cluster agglomeration leads to thin film growth. Third, eventual coarsening and two-phase growth leads to the formation of the vertically-aligned nanocomposite. Due to the immiscibility of the two phases, a vertical interface is formed and eventual nanopillar in matrix thin films result. The morphology of the VAN and pillar morphology are determined by growth parameters and materials selection [117].

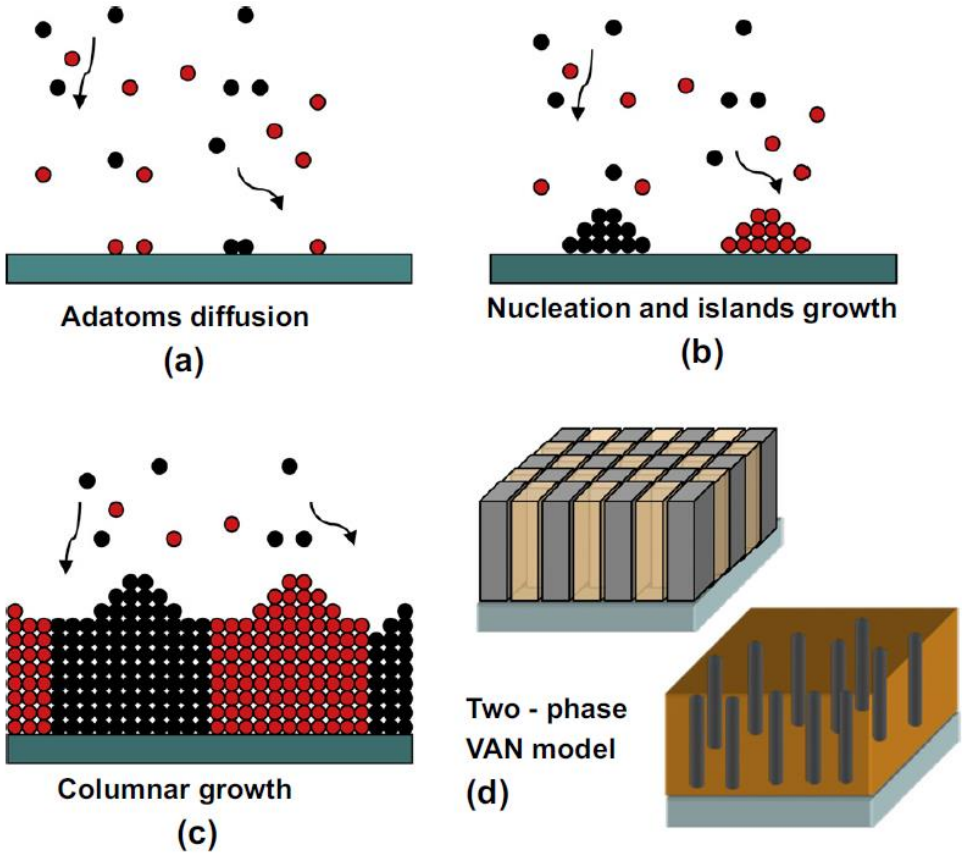

Figure 1.23 VAN growth mechanism. a) Adatoms arrive to substrate. b) Surface diffusion and nucleation. c) Coarsening and film growth. d) Resultant VAN morphology. Adapted from [107].

1.4.3 Spontaneous in-plane ordering

In nature, many biological processes observed can be described in terms of ordered structures. One such example are butterfly wings, which have a periodic nanostructure that absorbs and reflects the brilliant colors observed [118]. Another is in the color changes observed in chameleons which is linked to the arrangement in guanine nanocrystals underneath the chameleon skin [119]. In a relaxed state, the crystals are closely packed together in an ordered pattern and the chameleon will show an overall green color. [119,120]. In an excited state, the spacing between the ordered crystals expands and the color shift of the skin changes from green to blue and the ordering of the guanine crystals is directly tuned. [120,121]**.** Reconfigurable and ordered structures present opportunities for engineering multifunctionalities across a broad spectrum of scales. The vertically-aligned nanocomposite thin film platform offers a way to

achieve in-plane ordering of the pillar phase by underlying substrate templating or through spontaneous methods. [122]. Spontaneous ordering offers the benefit of controllable nanoscale ordering determined by the growth kinetics and thermodynamics. Furthermore, the spontaneous ordering allows for direct device integration of ordered heterostructures such as in integrated photonics circuits or ultra-high density memory devices. [110,122].

In-plane ordering in VAN thin films is achieved by selective control of the growth during deposition which includes the substrate orientation, substrate strain, self-templated growth, and through the growth conditions [110,114,122,123]. The substrate and interface energies of the thin film are highly sensitive to the orientation of the substrate. Different substrate orientation enables the formation of different pillar morphologies [124]. It was shown for the ZnO-LSMO system grown on two different $SrTiO_3$ substrate orientation of (100) and (110) that the orientation played a significant effect for achieving spontaneous in-plane ordering. When ZnO-LSMO VAN was grown on (100) substrate, the VAN exhibited a nanomaze-like morphology and when grown on (110) substrates, ZnO phase forms rectangular nanopillars [122]. The substrate strain also plays a role in determining the arrangement of pillars in the VAN structure. A $BiFeO_3$-$CoFeO_3$ VAN was grown on substrates including $LaAlO_3$, $LaNiO_3$, and $SrTiO_3$ [125,126] It was found that by varying the in-plane substrate parameter, it is possible to tune the in-plane ordering arrangement [124–127]. Based on the in-plane lattice parameter, a strain compensation model has been proposed for achieving spontaneously ordering VAN structures, shown in Figure 1.24. In the strain compensation model proposed, two phases A and B are selected to grow on a substrate with lattice parameter in-between A and B, with either A in compression or B in tension. After the growth of the A-B VAN, the ordered structure will form as a minimization of strain energy [122].

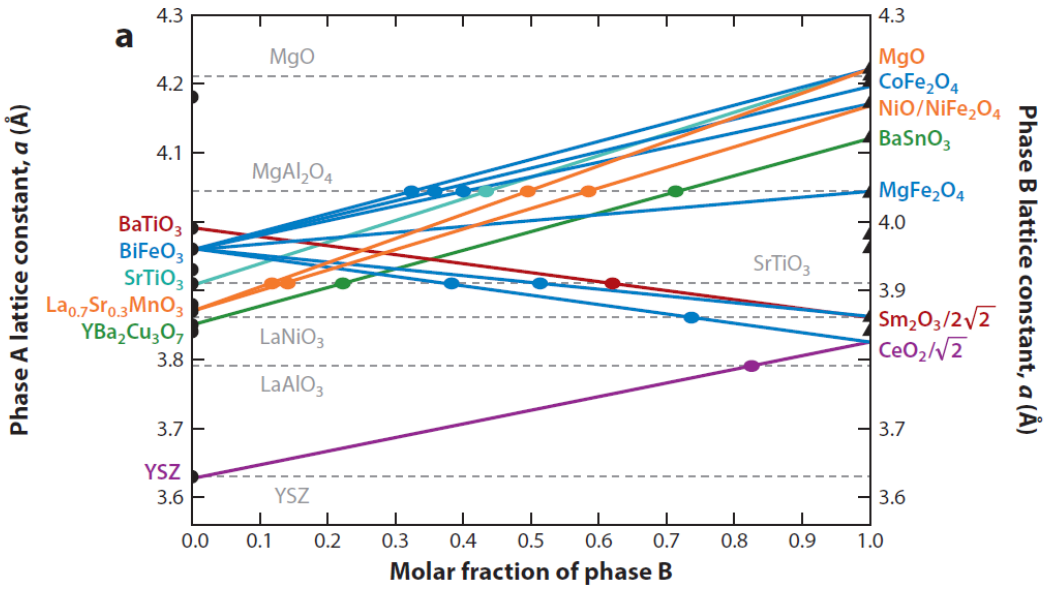

Figure 1.24 Theoretical in-plane lattice matching distances as a function of the relative molar ratio between A and B in VAN thin films. The left axis is for phase A and right is for phase B. Colored lines connection A and B mark the A-B VAN with spontaneously ordering microstructures. Dashed grey lines represent the in-plane lattice parameters of typical substrates, MgO, $MgAl_2O_4$, STO, $LaNiO_3$, $LaAlO_3$, and YSZ. Adapted from [122].

In-plane ordering can also be achieved through both growth control and through templated substrate growth. During growth, tuning of the parameters of oxygen pressure and substrate temperature have been shown to greatly affect the in-plane ordering. With increasing substrate temperature, in the BFO-$CoFeO_3$ system, has shown to control the in-plane width of pillars, reduce the pillar density, and increase the alignment of pillars [128]. The deposition pressure is a direct way to control the amount of kinetic energy available during the growth and increases the growth rate. For example, in BFO-CeO_2 VAN, increasing pressure resulted in smaller pillars of CeO_2 embedded in BFO [128]. It is also possible to control pillar in-plane ordering using templated substrates. Heat treated STO creates alternating terminated surfaces of SrO and TiO_2 [129]. A LSMO-CeO_2 VAN grown on templated STO substrate have CeO_2 (011) domains preferentially growing on SrO terminated surfaces [123]. Spacing between the pillars is also possible to tune by using different miscut angle substrates.

1.4.4 Oxide-oxide vertically-aligned nanocomposite thin films

Oxide-oxide vertically aligned nanocomposite platforms present great opportunity for combining oxide properties to achieve exotic multifunctionalities. Due to the unique two-phase combination and versatile selection of materials, the possibilities are virtually endless in terms of functional combinations for technical application and exploring physical phenomena. For example, low-field magnetoresistance (LFMR) has been explored in $La_{0.7}Sr_{0.3}MnO_3$ based nanocomposites [106,130]. YBCO superconductors combined with $BaSnO_3$ [131] have been used to explore flux pinning and ionic conductivity has been effectively increased in VANs for solid oxide fuel cells [132]. A high anisotropic conductivity is achieved in $(Ce_{0.9}Gd_{0.1}O_{1.95})$:$(Zr_{0.92}Y_{0.08}O_{1.96})$ (GDC:YSZ) thin films as a result of low oxide-ion migration due to the two-phase strain coupling allowing for fast ionic transport along the vertical oxide-oxide interface [132]. Multiferroic VANs have also been designed through vertical-strain coupling by combining ferroelectric and ferromagnetic oxides [115,133]. Moreover, vertical tunnel junction structures have been demonstrated in $La_{0.7}Sr_{0.3}MnO_3$:ZnO VANs by the coupling of LSMO ferromagnets with ZnO insulators [134]. Exchange bias has also been shown in VANs combining ferromagnets and antiferromagnets [135].

The oxide-oxide VAN beyond technical application also offer a platform for studying new modes of physical phenomena at both the vertical and lateral interfaces. Interfaces in correlated oxides create a promising platform for studying phenomena due to the interactions of atomic effects [136]. During the growth of oxide-oxide VAN, both kinetics and thermodynamics play important roles for determining the resultant morphology; elastic strain also helps determine the final morphology [112]. Oxide-oxide VAN systems have been used to study the highly correlated spin, orbital, charge, and lattice effects occurring at the heterointerfaces of different system. Due to the vertical strain coupling and highly tunable nature of VANs, these properties can be precisely controlled. For example, high carrier mobility has been discovered in $LaAlO_3$:$(Sm_2O_3)_x$ VAN thin films [135].

1.4.5 Oxide-metal vertically-aligned nanocomposite thin films

Oxide-oxide systems present the bulk of research for vertically-aligned nanocomposites but oxide-metal VANs have been realized where once thought incapable of growth due to the

different growth modes of metals and oxides [137,138]. In typical oxide-oxide VAN growth, nucleation is thought to occur as layer-by-layer growth for both phases due to the similar surface energy of oxide VAN phases and selected oxide substrates. Typically, metals grown on oxide substrate tend to grow as 3D islands due to vastly different surface energy. Therefore, to achieve oxide-metal VANs on oxide substrates, the different surface energies owing to 3D island growth of metals and 2D layer growth of oxides must be controlled. Moreover, systems must be selected such that co-growth can be achieved, and oxygen diffusion is reduced. One of the first demonstration of an oxide-metal VAN was in Fe_x:$(La_{0.5}Sr_{0.5}FeO_3)_{1-x}$ systems where decomposition of the LSFO resulted in Fe nanoinclusions [128]. Metallic arrays of different metals embedded into ceramic matrix have been demonstrated but require tedious growth methods and are limited by materials selection [139–141]. In comparison, a self-assembly approach utilizing the VAN platform would prove beneficial for applicability.

One of the first true self-assembled two-phase oxide-metal VAN was the $BaZr_{0.8}Y_{0.2}O_3$(BZY) -Ni system, demonstrating highly anisotropic ferromagnetic and electrical conductivity as compared with the bulk [142]. The promise of this material would be in magnetic data storage due to the highly anisotropic magnetic properties. Oxide-metal VAN have also come to include materials such as BTO-Au VAN for application in hybrid optical metamaterials, providing a throughput method for achieving nanowire array with hyperbolic dispersion [143,144]. In both the BZY-Ni and BTO-Au VAN, the materials were carefully selected for co-growth. When growth is not properly matched, this results in particle-in matrix formation such as in $LiNbO_3$-Au or TiO_2-Au [145,146]. The criteria for achieving VAN growth in oxide-metal nanocomposites is not yet fully understood, but the strain-compensation hypothesis may provide one guide for achieving ordered structure [122].

1.5 Plasmonics and light/matter interactions

1.5.1 Plasmonics

Surface plasmons are collective oscillations in the electron cloud at the interface between two materials with opposing dielectric functions [147,148]. They are readily excited at the metal/dielectric interface by absorption of light. By specific engineering of the nanostructure, surface plasmon modes can be used for nanoscale light manipulation and applications run the

gamut from biosensing, photonics, to energy-harvesting [149–153]**.** Currently, plasmonic metal nanostructures of noble metals (Ag, Au) are ubiquitous in application and study but surface plasmon resonance has been realized in doped-semiconductors [154,155] and in low dimensional materials like graphene [156]. In the gap between two plasmonic metal nanostructures, the optical field can be effectively enhanced [157,158] and used for non-linear optical application such as surface-enhanced Raman scattering [159–161]. The size and shape of the plasmonic nanostructure determines the type and mode of plasmon resonance, either transverse or longitudinal [162,163]**.** Some example morphology and extinction coefficients are given in Figure 1.25 for plasmonic Ag nanoparticles, demonstrating the relationship between particle morphology and plasmon resonance.

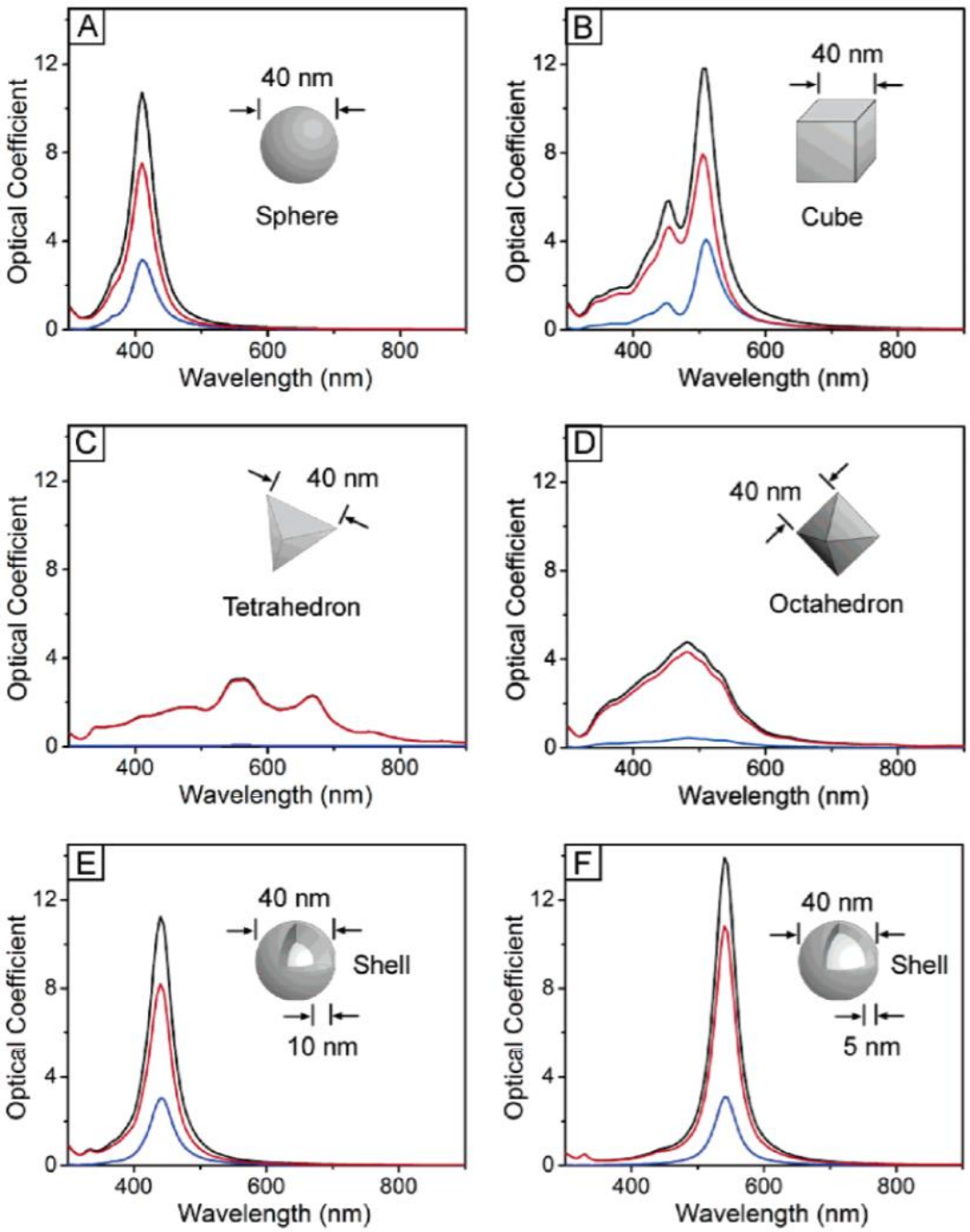

Figure 1.25 Calculated UV-vis extinction (black), absorption (red), and scattering (blue) spectra of silver nanostructures in water by mie theory. a) Isotropic sphere. b) Anisotropic cubes. c) tetrahedra. d) Octahedra. e) hollow and f) thinner shell walls. Adapted with permission from [164]. Copyright 2006. American Chemical Society.

1.5.2 Metamaterials

Metamaterials are those material specifically engineered to demonstrate functional properties not found in nature. They are usually constructed composite materials with specific and repeating patterns smaller than the wavelength of the element they influence. The properties they demonstrate are derived from the geometry of the designed structure based on shape, shape, size, and orientation and are capable of interactions with electromagnetic fields, as schematically shown in Figure 1.26. They can be used to break the diffraction limit [165], achieve negative refractive index [166], investigate fundamental physical phenomena [167,168], guide and bend light [169–171], and to achieve superconductivity [172,173]. Analogues of optical metamaterials also exist in acoustic based devices [174–176].

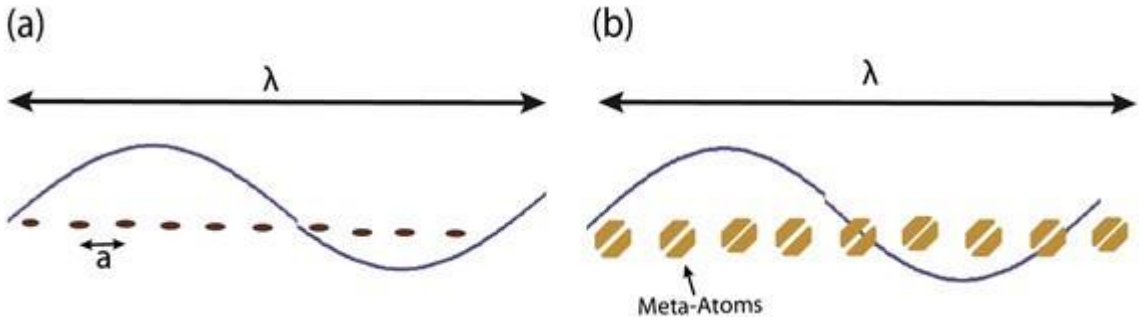

Figure 1.26 a) Periodic array of atoms with radius and interatomic spacing of each atom much less than wavelength of radiation. b) Metamaterials composed of nanoinclusions called meta-atoms with critical dimensions much less than the wavelength of radiation. Artificial atoms provide unique electromagnetic responses not seen in natural structures. Adapted from [177].

1.5.3 Hyperbolic metamaterials

Hyperbolic metamaterials (HMMs) have gained attention for playing a central role in the field of integrated photonics and nanophotonics due to their access to the near-field. HMMs derive their properties from surface plasmon resonance, the discrete oscillation of electrons at the interface between a dielectric and metal. For a hyperbolic metamaterial made up of multilayers, the supported resonance is a propagating surface plasmon [178]. For HMMs made up of nanoparticles or nanowire embedded into matrix, the metal surface supports localized surface plasmons [178]. The excitement of a surface plasmon resonance is accompanied by electromagnetic field enhancements in the near-field of the interface which decays exponentially in the area surrounding the metallic surface. For subwavelength dielectric/metal multilayers that

are periodically stacked or in periodic arrangements of metallic nanowire embedded into matrix, the electromagnetic field enhancement are bound to individual plasmonic surfaces, creating a collective response and a bulk effective dielectric function [178–180]. In general, HMMs contain anisotropic dispersion in their dielectric function, hence hyperbolic.

Two specific structures have been identified for realizing hyperbolic metamaterials, including metal/dielectric multilayers and metallic nanowires in dielectric matrix. The two different nanostructures are demonstrated in Figure 1.27. Hyperbolic metamaterials support the propagation of high k-vector, allowing for the breaking of the diffraction limit [181] and for optically resolvable sub-wavelength objects through optical hyperlenses [182]**.** The HMM can also be utilized in quantum sources to enhance the spontaneous emission for tunable fast decay broadband features [183,184] and HMM in the IR range can allow for heat transfer for thermal emissions [180]. Hyperbolic metamaterials have also been looked at as potential analogues for studying fundamental physical phenomena such as hawking radiation. [167,185] Dynamically tunable HMMs are the proposed new direction for achieving a real-time tunable dielectric function [186].

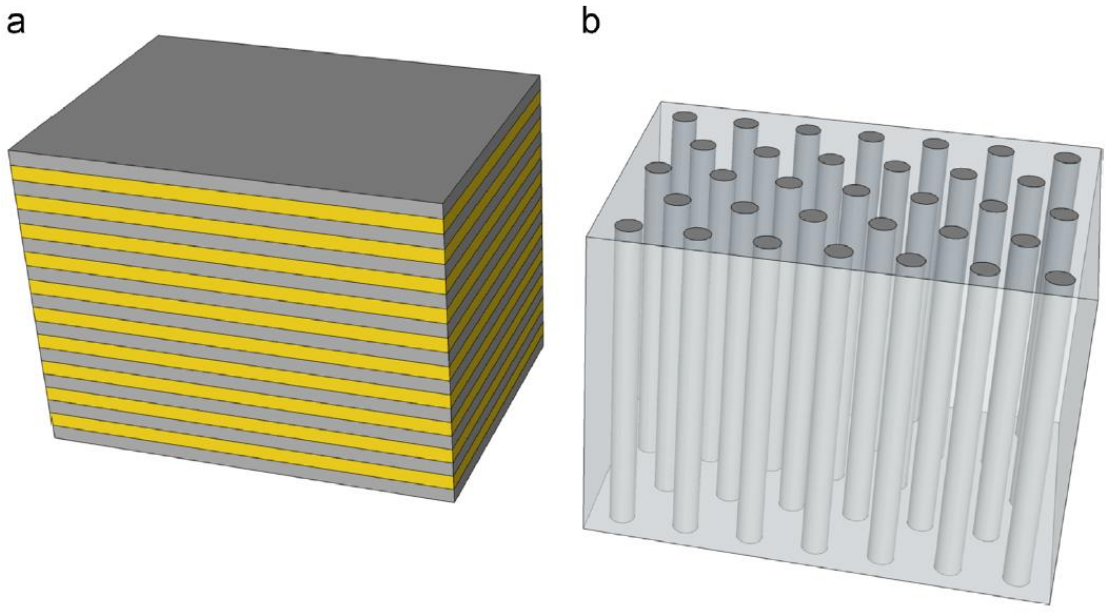

Figure 1.27 Schematic diagram showing hyperbolic metamaterials including a) multilayer and b) metallic nanowire embedded in matrix. Adapted from [179].

Hyperbolic media are described in terms of their isofrequency curves in k-space, which can be understood from the following equation giving the dispersion relation for uniaxial media:

$$\text{Equation 8 } (k_\perp^2 + k_z^2 - \varepsilon_\perp k_0^2)\left(\frac{k_\perp^2}{\varepsilon_{zz}} + \frac{k_z^2}{\varepsilon_\perp} - k_0^2\right) = 0 \quad [181]$$

Here, $k_\perp$ and k_z are the components perpendicular and out of plane of the wave-vector with $k_\perp = \sqrt{k_x^2 + k_y^2}$. $\varepsilon_\perp$and. ε_{zz} are the components of permeability for perpendicular and out of plane with $\varepsilon_\perp = \varepsilon_{xx} = \varepsilon_{yy}$. In the case of both perpendicular and out-of plane being zero, one will obtain an isofrequency curve of an ellipsoid. For $\varepsilon_\perp > 0$ and . $\varepsilon_{zz} < 0$, this corresponds to a two-fold hyperbolic isofrequency surface and is termed a dielectric or type I HMM (in reference to behavior in the perpendicular plane) [179]**.** For the case of $\varepsilon_\perp < 0$ and . $\varepsilon_{zz} > 0$, this is a one-fold hyperboloid isofrequency curve termed metallic or Type II HMM [179]. The dispersion relation and isofrequency surfaces are demonstrated in Figure 1.28.

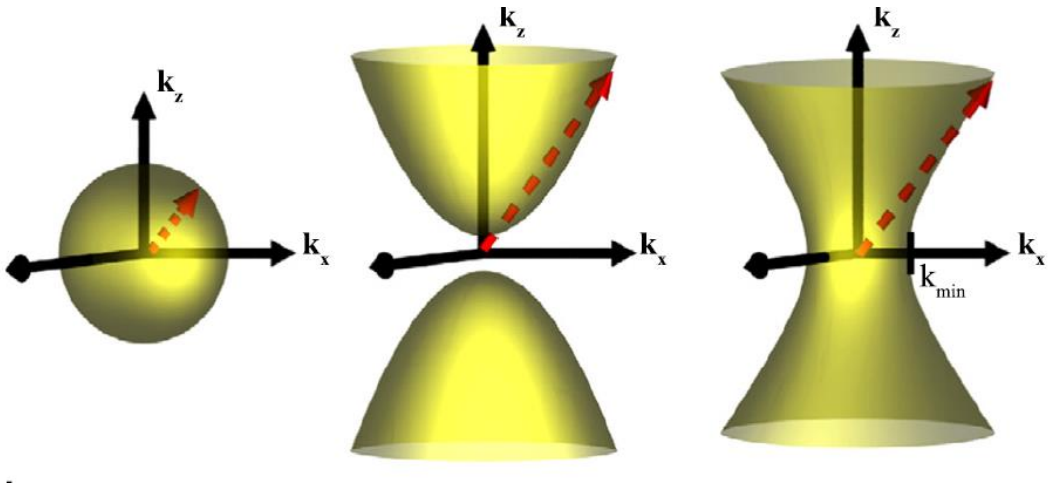

Figure 1.28 Types of isofrequency surfaces .in 3D k-space for an isotropic medium and hyperbolic medium of Type I and Type II response. Adapted from [179].

Efforts have been devoted to realizing practical application of HMMs but is widely limited due to fabrication and materials selection. The multilayer HMM require multi-step and controlled deposition to produce structures. The nanowire array offers a much better route for achieving application of HMMs toward future devices. Such techniques as electrochemical deposition, e-beam lithography, and anodic aluminum oxide (AAO) templating have all been used to achieve HMMs [181,187,188]. Though promising, these methods are limited to materials selection, tedious fabrication, and the potential scalability. Recently, the self-assembled

oxide-metal VAN system has gained attention as a platform for achieving nanowire array of HMM due to the streamlined, one-step self-assembly with tunable nanoscale structure [143]. Another limitation to hyperbolic metamaterials is in the active plasmonic metals utilized. Noble metals such as Ag and Au are used for their strong resonance but suffer from dissipative losses due to joule heating. To reduce loss, different materials and geometries have been proposed [189–192].

1.6 Thesis motivation

1.6.1 Motivation for thesis work

The oxide-metal vertically aligned nanocomposite thin film platform provides great opportunity for combining two unique and vastly different materials into a new material. Due to the recent emergence of this field, there is great opportunity for studying new physical phenomena and the effect of deposition parameters on the morphology and properties. For example, is it possible to grow metals in an oxygen ambient without oxidation effects? There are limited fundamental studies in terms of oxide-metal VAN systems. The motivation for the work presented in this thesis is both fundamental and application based. ZnO matrix is selected as the base oxide matrix material and different metals are incorporated to form new functional oxide-metal VANs. ZnO presents great opportunity for incorporation due to its functional properties, non-toxicity, and general availability. Au is first incorporated to study hyperbolic dispersion in ZnO VAN. ZnO-Au VAN are grown on hexagonal c-cut sapphire substrates and the combination of hexagonal ZnO and cubic Au presents opportunity for studying the epitaxy of unique cubic/hexagonal structures where previous oxide-metal VAN have been cubic/cubic structures. Furthermore, the ZnO-Au VAN provides a platform for studying the fundamental effects of parameter tuning including oxygen pressure and frequency tuning and the resulting effect on both properties and morphology.

The ZnO-Au VAN is presented as a platform the realizing hyperbolic dispersion in ZnO materials. The second part of this thesis is involved in improving the absorption losses of hyperbolic metamaterials due to the metallic Au. A nanoalloy approach is employed based on Au_xAg_{1-x}, as Ag are determined to have much lower losses than Au. Moreover, the ZnO-Ag forms a particle-in matrix morphology and a nanoalloy approach is presented as a way to co-

grow metals and oxides into VAN that may prefer a particle-in matrix formation. Following the successful demonstration of the ZnO-Au_xAg_{1-x} oxide-nanoalloy VAN with much lower losses than those of ZnO-Au VAN, a fundamental parameter tuning based on oxygen pressure is performed on ZnO-Au_xAg_{1-x} VAN. The oxygen pressure tuning proves an effective way to tune nanoalloy composition, pillar morphology, and optical properties. In the final chapter of this thesis, new ferromagnetic metals are incorporated into ZnO. ZnO with Ni, Co, and Ni_xCo_{1-x} nanoalloy are explored. In the case of ZnO-Co, interdiffusion caused the formation of a ZnO-CoO VAN so an alloy approach with Ni was proposed to achieve ferromagnetic metals into ZnO matrix.

2. EXPERIMENTAL SECTION

2.1 Pulsed laser deposition

All the films grown in this report were deposited through the pulsed laser deposition technique. A detailed description of the method can be found in Section 1.2.4. A two-phase nanocomposite target is used for deposition and are prepared through a sintering with spark plasma sintering. Targets are prepared by calculating specific molar ratio and nanoparticle powders are used and mixed together for sintering. ZnO based VAN thin films are then grown through the PLD method on c-cut sapphire substrate. The laser used for the growth is a Lamdba Physik Complex Pro 205, with λ=248 nm. The parameters tuned during this thesis include the oxygen background pressure and the laser frequency. Pressure is fundamental in controlling both oxygen stoichiometry in the film and surface diffusion during condensation.

2.1.1 X-ray diffraction

X-ray diffraction is a powerful microstructural characterization technique which can reveal the crystal structure of a material. It can also reveal information about the composition, size and shape, strain, and epitaxy of a material. In this thesis work, XRD was utilized to understand the epitaxial quality of films as well as the strain present. The system used was a Panalytical XPert X-ray diffractometer with Cu target having corresponding wavelength of 0.154 nm, as shown in Figure 2.1. X-ray diffraction works by bombarding the sample with an electron beam and generating x-ray signal, which are then measured by a detector.

Figure 2.1 X-ray diffraction setup

Diffraction is caused by the scattering of radiation by periodic arrays with spacing with equivalent spacing as the λ as the radiation. For crystalline structures, the atoms and ion are ~0.1 nm in size and will act as diffraction gratings on the sub-nanometer scale. Spacing between the lattice places are hkl miller indices and the interplanar distance d_{hkl} is the distance between parallel crystal planes. In XRD, crystal planes *diffract* incoming radiation, which can be described by the Bragg's law. The Bragg's law relationship can be described by Equation 9:

Equation 9 $dsin\theta = n\lambda$

where λ is the wavelength of the incoming x-rays (0.154 nm for the setup in this thesis work), d is the interplanar lattice spacing, and θ is the angle of diffraction. Measurement of the critical angle θ allows for the computation of interplanar spacing d. For diffraction to be measured in a crystal, the reflections must be detectable which necessitates x-rays to be scattered off adjacent crystal planes that are in phase. When x-rays are in phase, this leads to constructive interference, allowing for diffracted waves to reinforce and the Bragg's law is satisfied. When destructive interference occurs, diffracted waves are out of phase and cancel each out, Bragg's law is not satisfied, and no data is measured.

The Bragg's law is a simplification for understanding the basic principle of diffraction. It is necessary but insufficient for describing diffraction as it only describes the diffraction condition for primitive unit cells. Most material and crystal structure will have atoms at additional lattice sites which can cause out-of-phase diffraction to occur outside of Bragg angle and the diffraction predicted by the Bragg's law will not occur, e.g forbidden reflections. To calculate forbidden reflections, an atomic scattering factor and structure factor are used. These are important for determining both amplitude and phase of reflections and plays a role in refining the crystal structure since it is related to the reflection intensity. The structure factor is given in the following equation:

Equation 10 $F_{hkl} = \sum_{i=1}^{N} f_i e^{2\pi i(hu_i+kv_j+lw_i)}$

Equation 10 describes how atomic arrangement uvw influences intensity of reflected waves and determines which reflections to expect.

2.1.2 Transmission Electron Microscopy

Transmission electron microscopy was heavily utilized in this work to investigate the morphology of vertically-aligned nanocomposite thin films. Specifically, both transmission electron microscopy (TEM) and scanning transmission electron microscopy (STEM), an overview of which is given in Figure 2.2. Electron microscopy is analogous to optical microscopy but uses an electron beam and electromagnetic focal lenses instead of light-based components and lens. The benefit of using an electron beam is the high image resolution which can allow for the measurement of both position and chemistry of individual atoms. The electron beam also offer a very high magnification range, from 200 to 1 million times in the TEM and can image from micro to nano-scale in one imaging session. Moreover, electron generated signals lead to a wide range of phenomena due to interaction between electrons and atomic structures, and information about structure and chemistry can be extracted at specific locations of the specimen.

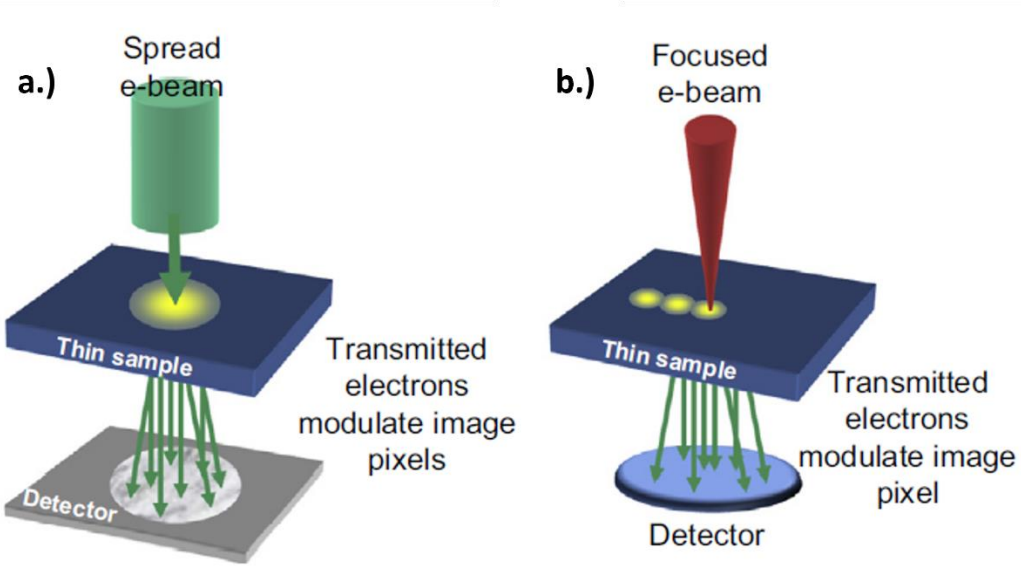

Figure 2.2 Schematic overview of TEM and STEM imaging methodology. a) Parallel image acquisition in the TEM, b) serial collection of transmitted electrons in the STEM. Adapted from [193].

An overview of the different components in a TEM system is shown in Figure 2.3. In the TEM, the electron beam is accelerating electrons across a 80-300 kV voltage to allow for passage through up to a micron thick material. For routine imaging, 2-300 kV high voltage is

used while lower energy electrons accelerated with kV <100 is used for imaging of light elements or for sample damage reduction. Control of the electron beam is produced through a series of different electromagnetic lenses. The condenser lenses focus the beam into a specific size and convergence angle. Objective lenses focus transmitted electrons and form both first image and diffraction patterns that are then magnified by projector lenses into the detector unit. Additional lenses are installed for the STEM imaging mode. TEM has two operation modes including diffraction and imaging, and contrast is determined by interactions of the electron with the sample such as scattering, illumination, and the path of electrons through the lenses after passing through the sample. As electrons pass through, they are scattered either elastically or inelastically, scattered electrons can be locked with an objective aperture to form a bright-field image from unscattered electrons with darker contrast. The objective aperture when situated at the back focal plane will block elastically scattered electrons and form a dark-field image. Elastically scattered electrons can also be used to form diffraction patterns in the back focal plane of the objective lens. Selective area electron diffraction (SAED) is a tool used in TEM to analyze lattice information including type, parameter, orientation, and phase relationships.

In the scanning mode of TEM, specific coils are fitted to the microscope that can scan the electron beam across the sample. In the STEM mode, contrast is very strong due to small nearby changes in the atomic number, i.e. z-contrast. Electrons in the STEM mode are collected by a specific detector called the high angle annular dark field detector to form images. Another important tool of the STEM mode is chemical x-ray analysis, or energy dispersive spectroscopy (EDX). Spatial resolution can allow for the elemental identification of single atoms.

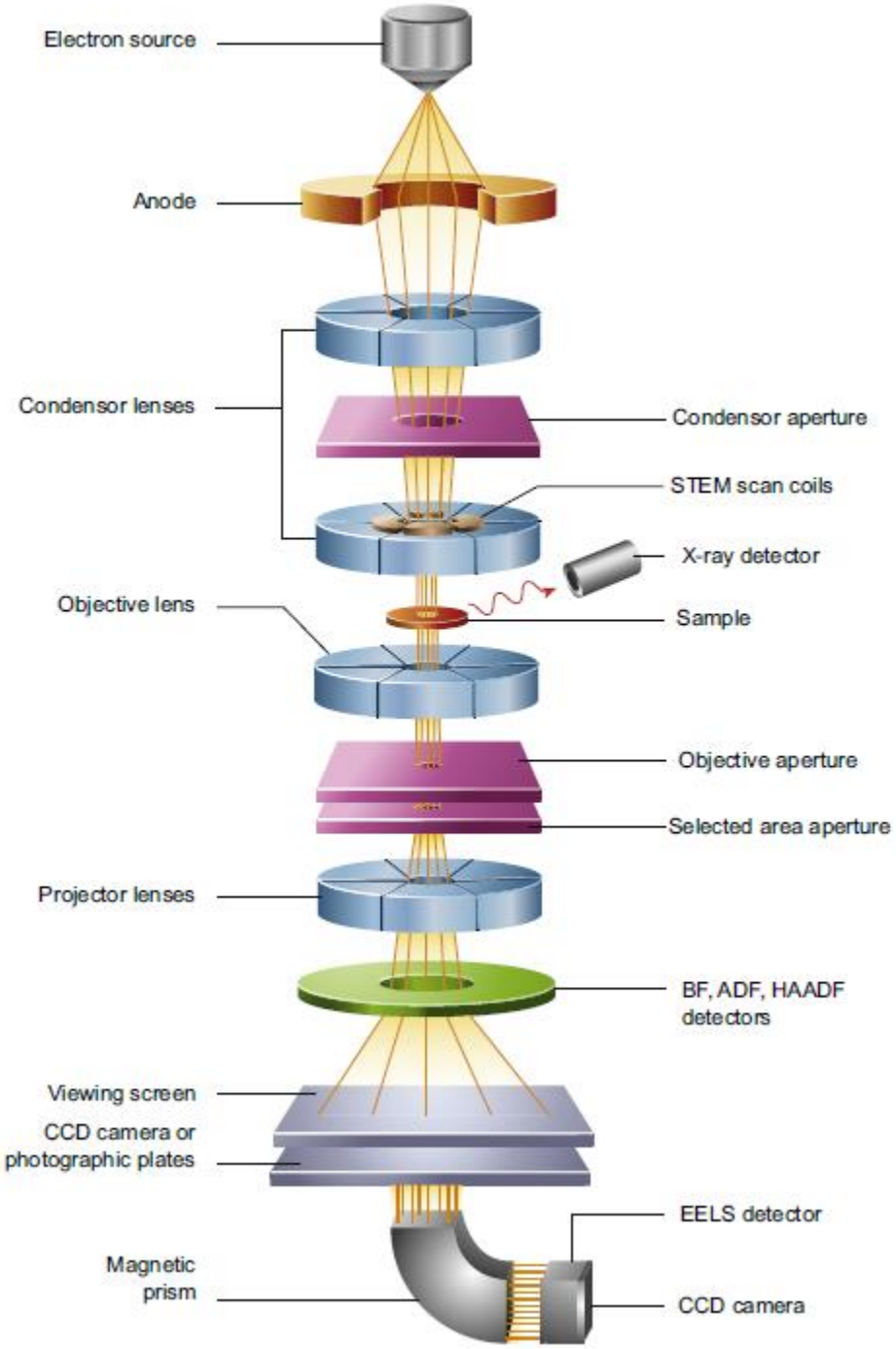

Figure 2.3 Schematic overview of parts in a TEM microscope. Adapted from [193]

2.2 Optical Measurement tools

2.2.1 Spectroscopic Ellipsometer

Spectroscopic ellipsometry is a non-destructive optical surface characterization technique for investigating thin film systems. It can provide information about complex optical functions, the roughness of the film, and can characterize interfaces in multilayer films. Measurements are based on the polarization of light reflected from a film sample. A model is then used to fit the measured data to reveal sample information; measurement itself is throughput but modeling and analysis requires interpretation to reveal obtain sensical data. The measured data are ψ and Δ, which describe the angle of polarization and are based on the complex Fresnel reflections. Ellipsometry measurements were carried out in this thesis on an RC2 Spectroscopic Ellipsometer (J.A. Woodlam Company) across a spectrum range of 210-2500nm. An image of the setup can be found in Figure 2.4.

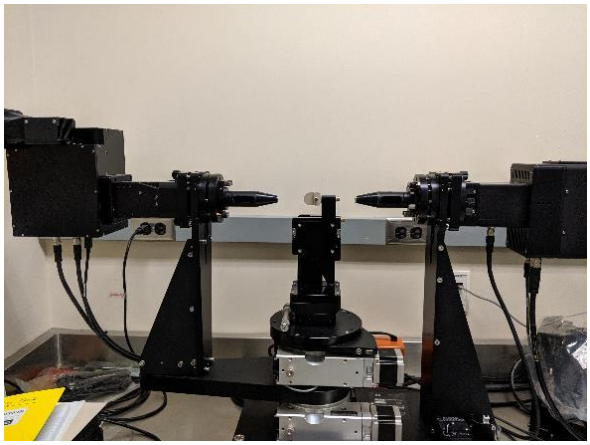

Figure 2.4 Spectroscopic ellipsometer setup.

2.2.2 UV-Vis Spectroscopy

UV-Vis spectroscopy is a measurement of absorptive or reflective properties in the visible and ultraviolet regime through the use of light in those regimes. The technique was used to measure plasmonic responses of the metals in the ZnO-based VAN thin films in this thesis work. In the UV-Vis range, atoms and molecules will absorb light and undergo an electronic transition to excite electrons in the orbital to a higher anti-bonding state. This excitation will absorb and give off a specific wavelength of light, which can then be measured. For this thesis work, a Lambda 1050 UV-vis spectropherometer was used, which an image is depicted in Figure 2.5.

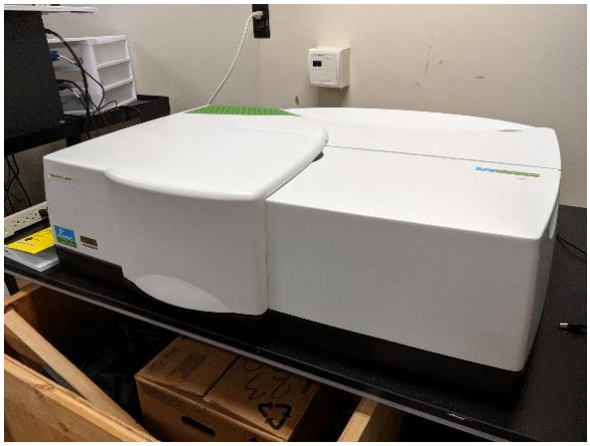

Figure 2.5 UV-Vis spectrophotometer

2.3 Magnetic property measurements

Magnetic property measurements (or MPMS) were conducted on ferromagnetic metal and ZnO vertically-aligned nanocomposites in chapter four of this thesis. An MPMS-3 magnetometer was used which measures the magnetic field of small and thin film samples. This is done with a superconducting quantum interference device (SQUID) sensor. In the MPMS, a superconducting NbTi wire is wound into coils which the sample is moved through. There are two modes, DC and VSM mode, in DC mode the sample is moved linearly through the coils and in VSM mode the sample is oscillated through the coils. The static magnetic moment is measured but it is also possible to measure the AC susceptibility, e.g. the response of the sample to a specific AC magnetic field.

3. STRAIN DRIVEN IN-PLANE ORDERING IN VERTICALLY-ALIGNED ZNO-AU NANOCOMPOSITES WITH HIGHLY CORRELATED METAMATERIAL PROPERTIES

3.1 Overview

Hyperbolic metamaterials demonstrate exotic optical properties that are poised to find applications in subdiffraction imaging and hyperlenses. Key challenges remain for practical applications, such as high energy losses and lack of hyperbolic properties in shorter wavelengths. In this work, a new oxide-metal (ZnO-Au) hybrid-material system in vertically aligned nanocomposite thin film form has been demonstrated with very promising in-plane two-phase ordering using a one-step growth method. Au nanopillars grow epitaxially in ZnO matrix and the pillar morphology, orientation, and quasi-hexagonal in-plane ordering are found to be effectively tuned by the growth parameters. Strong surface plasmon resonance has been observed in the hybrid system in the UV-Vis range and highly anisotropic dielectric properties are resulted with much broader and tunable hyperbolic wavelength regimes. The observed strain-driven two-phase in-plane ordering and its novel tunable hyperbolic metamaterial properties all demonstrate strong potential for future oxide-metal hybrid-material design towards future integrated hybrid photonics.

3.2 Introduction

Optical metamaterials with epsilon near zero (ENZ) permittivity and hyperbolic dispersion can be created in nanostructures that consist of periodic arrangements of negative permittivity. The periodic nature of these structures create photonic band gaps in which certain wavelengths of electromagnetic radiation are not permitted to propagate within the material. One way to achieve this structure is through directly embedding arrays of metallic nanowires into a dielectric medium, which is expected to create ENZ permittivity [194,195] and lead to hyperbolic

dispersion [179,181]. The exciting realization of ENZ in the visible range could lead to exotic functionalities including light squeezing by subwavelength waveguides [196,197], light-tunneling [198], and invisible cloaking [199]. Nanowire arrays present large aspect ratios which lead to uniaxial anisotropy and hyperbolic dispersion, in which one direction of the material behaves like a metal and in the other direction it behaves as a dielectric[3,9]. Hyperbolic metamaterials were first theorized and created for optical imaging beyond the diffraction limit [165], but new research has led to applications in high T_c superconductivity [172,200] and as a potential platform for studying fundamental physical phenomenom [167,168,185,201].

Much effort has been devoted towards the realization of metallic nanoarray structures for metamaterials application with techniques such as electrochemical deposition [153], e-beam lithography [202], and anodic aluminum oxide (AAO) template method [203,204]. Although promising, the AAO template and lithography methods are typically limited by materials selection, tedious multi-step growth methods, and scalability [204]. It was also reported that hyperbolic dispersion and ENZ permittivity are strongly correlated with the anisotropy and ordering of the metallic nanowire array. Thus, it is important to precisely control the metamaterials on a nanoscale for highly tunable properties. Another critical need is to produce metamaterials with hyperbolicity in shorter wavelength regimes (e.g., visible), while the demonstrated hyperbolic metamaterials are mostly in the longer wavelength regime (e.g., infrared),

Recent efforts are focused on oxide-metal hybrid metamaterials in a vertically aligned nanocomposite (VAN) form, grown through a one-step pulsed laser deposition (PLD) technique. VAN's have demonstrated their potential in nanoscale metamaterials design through robust materials selection and highly anisotropic optical properties [143,145]. The unique vertical strain coupling along the two-phase interface has led to unique multifunctionalities [107,108,111,115,205]. However, extensive work on morphology tuning and strain engineering has been focused on oxide-oxide VAN systems and related properties[22,27–29]. The work on strain engineering and morphology tuning in oxide-metal systems is scarce [207,208].

In this work, a new oxide-metal hybrid metamaterial (ZnO-Au) in the VAN form has been demonstrated using PLD. As illustrated in Figure 3.1, the Au nanopillars grow uniformly and epitaxially in the ZnO matrix. In this study, Au is selected as the plasmonic metallic

nanostructure in the metamaterial and ZnO is selected as the matrix due to its well-known dielectric response and piezoelectric properties. ZnO was also selected for other properties such as non-toxicity, earth abundance, and enhanced photocatalytic properties [209]. The proposed morphology tuning can be achieved by varying the growth parameters such as oxygen partial pressure and laser deposition frequency. Through the morphology and in-plane ordering control, it is expected to achieve tunable optical responses such as hyperbolic behavior and wavelength range, anisotropic complex dielectric properties, and plasmonic wavelength. Thus, detailed microstructural analysis including TEM, STEM and EDX mapping are conducted to couple with the optical properties measured by optical transmittance and ellipsometry.

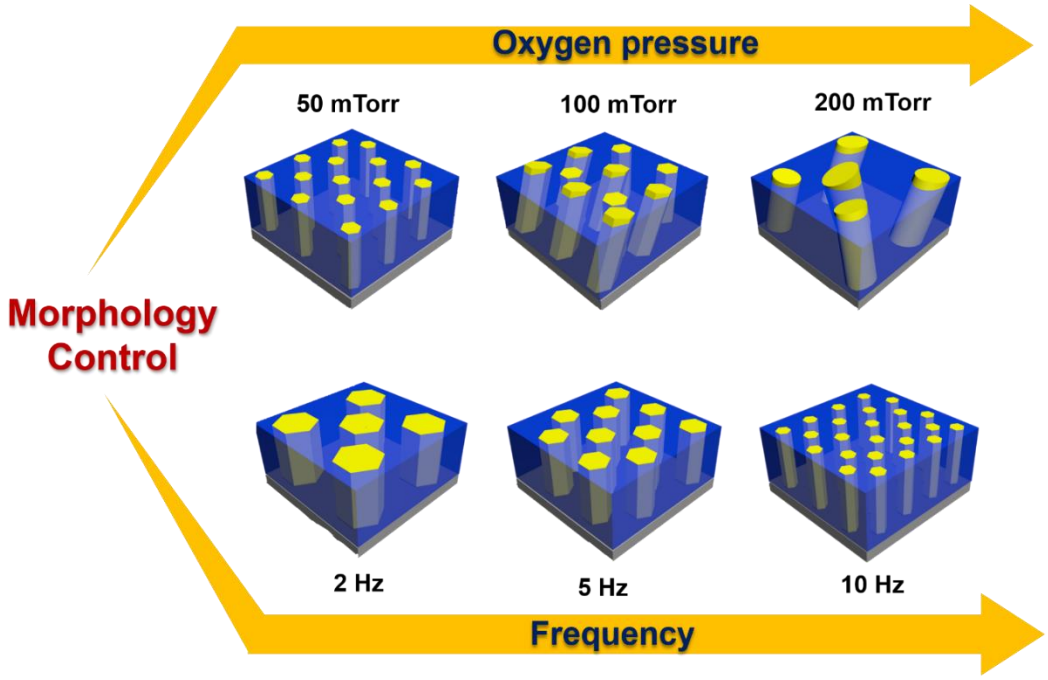

Figure 3.1 Schematic diagram of the ZnO-Au VAN grown on c-cut Al2O3 and designed for optical metamaterial applications. A high degree of morphological control is possible through changing oxygen background and frequency in pulsed laser deposition.

3.3 Experimental

3.3.1 Thin film growth

ZnO-Au vertically-aligned nanocomposite films were grown on c-cut Al_2O_3 (0001) in two series, an oxygen background pressure series and a pulse laser frequency series. Across all series, deposition was performed with a KrF excimer laser (Lambda Physik Complex Pro 205, λ

= 248 nm) and substrate temperature was kept constant at 500 ^{o}C. The laser beam was focused with an incident angle of 45^{o} with a laser energy of 420 mJ. The target-substrate distance was kept constant at 4.5 cm and measured before each deposition to ensure accuracy. A nanocomposite target consisting of 1:1 Au:ZnO developed through solid-state sintering was used for laser ablation. Before deposition, the chamber was pumped down to around 10^{-6} mTorr before an oxygen pressure was inflowed. For the background pressure series, deposition occurred from 50 – 200 mTorr with a constant pulse frequency of 5 Hz. The pulse laser frequency series maintained a constant pressure of 100 mTorr while laser frequency repetition was varied from 2 – 10 Hz. The reference sample between the two series was deposited at 5 Hz and 100 mTorr. After all depositions, the chamber was cooled to room temperature at a rate of 15 ^{o}C/min.

3.3.2 Microstructure characterization

Film morphology was characterized through XRD, TEM, and STEM coupled with EDS-mapping. XRD scans of θ-2θ were conducted using a Panalytical X'Pert X-ray diffractometer wit Cu K_{α} radiation. Bright field TEM, STEM, SAED patterns and eds-mapping was performed in a FEI Talos F200X TEM. Samples for electron microscopy were prepared, for both cross-section and plan-view, via a standard grinding procedure which entails manual grinding, polishing, dimpling, and a final ion milling step to achieve electron transparency. (PIPS 691 precision ion polishing system, 5 KeV for cross-section and 4-4.5 KeV for plan-view sample)

3.3.3 Optical measurements

Ellipsometry experiments were carried out on an RC2 Spectroscopic ellipsometer (J.A. Woollam Compnay). Three angles 30^{o}, 45^{o}, and 60^{o} were measured from a spectrum range of 210 – 2500 nm. Psi and delta data were obtained from ellipsometry experiments and then fit with an uniaxial model coupled with B-spline model were used to discern anisotropic permittivity properties of ZnO-Au VAN, an agreeable mean square error (MSE) < 5 was obtained for all film models. Normal incident depolarized transmittance (T%) was measured using an optical spectropherometer (Lambda 1050 UV-vis spectropherometer).

3.4 Results and Discussion

One of the challenges for growing high quality ZnO-Au VAN was the vastly different crystal structures between Au (FCC) and hexagonal ZnO (Wurtzite, HCP). This was surmounted by growing ZnO-Au VAN on α-Al_2O_3 substrate. There have been no reports for growth of oxide-metal VAN in oxygen ambient due to metals hazarding a chance of oxidation upon ablation in an oxygen ambient. Oxidation was determined not to occur, as there was no presence of gold oxide peaks in any X-ray Diffraction (XRD) scans in Figure 3.4e or Figure 3.6e, or any diffraction spots besides those from Au, ZnO or sapphire in Selective Area Electron Diffraction (SAED) patterns in Figure 3.2a-b. Interestingly, successful growth required an oxygen ambient. When growth was performed in vacuum, this led to irregular morphology and films that would easily wipe away caused by poor adhesion, possibly due to high laser plume kinetic energy. The use of a background pressure could create confinement of the plasma plume and modulation of kinetic energy, leading to more regular film growth and morphology. Formation of the ZnO-Au VAN is believed to follow a general three-step mechanism, similar to other oxide-metal VAN [143]. A diagram of the formation mechanism can be found in Figure 3.3. Following the diagram in Figure 3.3, ZnO and Au adatoms arrive to Al_2O_3 substrate and undergo surface diffusion. Second, initial nucleation begins. Owing to the different surface energies, Au nucleates as 3D-islands and ZnO as 2D layers. Growth continues in this manner, with Au 3D-island forming nanopillars and ZnO growing layer-by layer to form the matrix. Finally, ZnO-Au forms as pillar-in-matrix vertically-aligned nanocomposite.

For optimized vertical nanopillar growth, 50 mTorr oxygen background pressure created absolute vertical growth as seen in Figure 3.4a.1. The 50 mTorr film shows strong hexagonal faceted gold nanopillars arranged in hexagonal long-range order, seen in the STEM plan-view image in Figure 3.4a.5. The mesoscale quasi-hexagonal ordering is more obvious in the low-resolution STEM image in Figure 3.5. EDS mapping was performed on the 50 mTorr sample in Figure 3.4a.2 and Figure 3.4.a4 to show there was no significant interdiffusion between Au and ZnO. To further confirm this, high-resolution STEM was performed in Figure 3.4a.3. This image was taken from the <10-10> zone axis of the sapphire substrate and shows the cross-section atomic arrangement of Au and ZnO with distinct heterointerface.

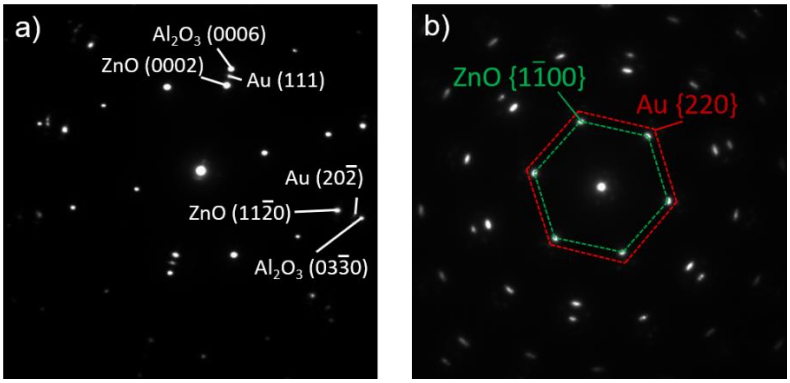

Figure 3.2 SAED patterns obtained through TEM imaging. For a) cross-section and b) plan-view

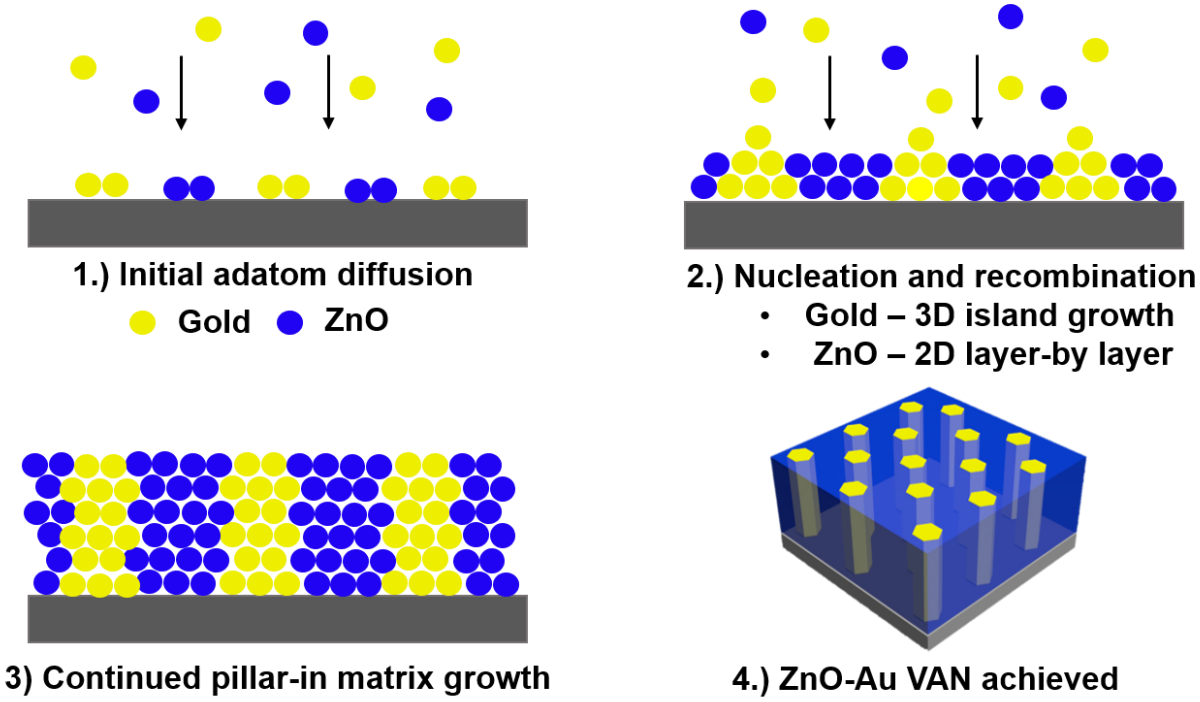

Figure 3.3 General formation mechanism for growth of vertically-aligned ZnO-Au nanocomposite

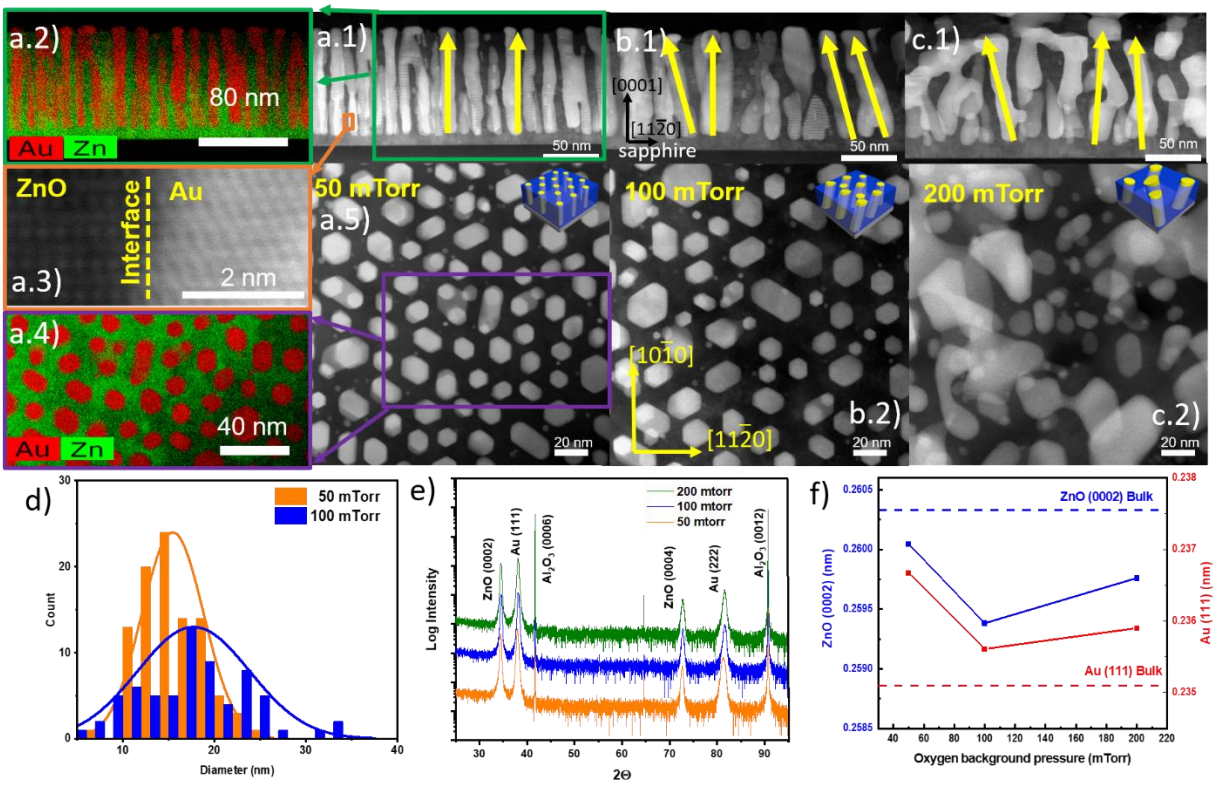

Figure 3.4 Oxygen background pressure study. STEM cross-section images are presented for the samples under the background pressure of a.1) 50 mTorr, b.1) 100 mTorr, and c.1) 200 mTorr. Observed pillar alignment is denoted with yellow arrows in a-c.1). The EDS-mapping for the 50 mTorr sample is shown for the cross-section sample in a.2) and the plan-view sample in a.4). HRSTEM of ZnO-Au interface in cross-section is provided in a.3). STEM plan-view images are shown for a.5) 50 mTorr, b.2) 100 mTorr, and c.2) 200 mTorr. d) Histogram plot of pillar dimensions for the 50mTorr and 100mTorr samples. e) XRD θ-2θ scans for the samples under different oxygen pressure. f) d-spacing calculated from e).

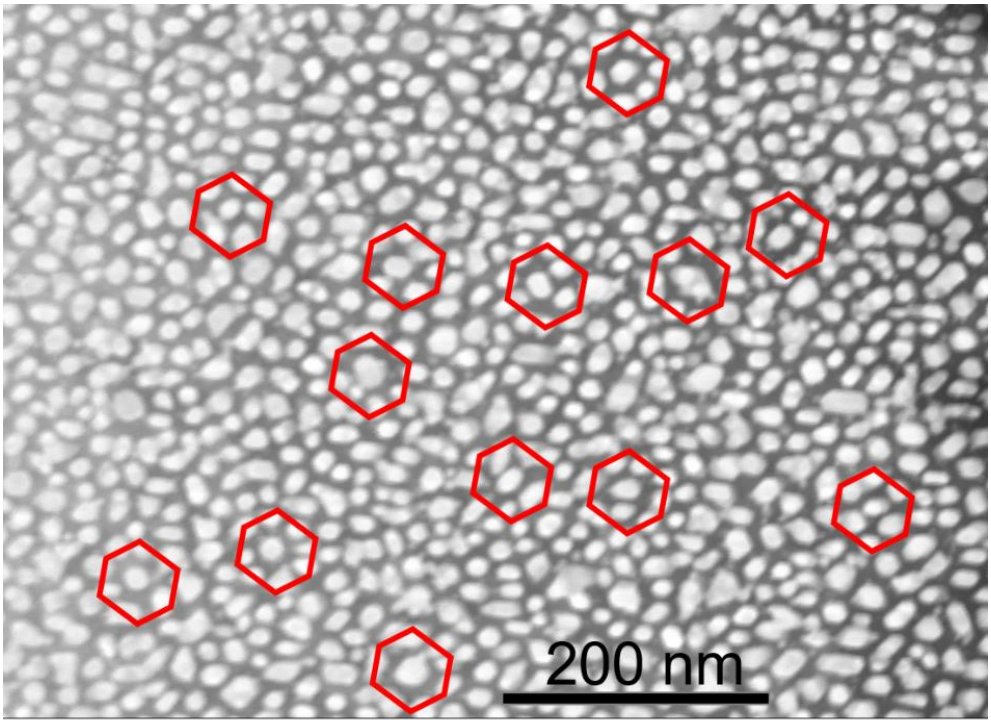

Figure 3.5 A low-magnification STEM image was obtained to show the long-range quasi-hexagonal-close packed ordering. Red hexagons are placed as a visual aid to indicate ordering.

Background pressure was further increased to investigate the effect of kinetic modulation on nanopillar morphology. Films were grown at 100 mTorr and 200 mTorr, as seen in Figure 3.4b.1, c.1. The average pillar diameter was calculated by measuring the diameter of pillars in STEM plan-view images in Figure 3.4a.5 and Figure 3.4b.2. The measured diameters were then plotted as a histogram in Figure 3.4d and the average diameter was taken as the mean value of the histogram. This method is adopted from techniques used to calculate grain size distributions [210,211]. The histogram indicates that the average pillar diameter increases from ~15 nm at 50 mTorr to ~18 nm at 100 mTorr. For the film grown at 200 mTorr in c.1, the cross-section image shows that nanopillars became randomly orientated and the plan-view in Figure 3.4c.2 illustrates the irregular shape and loss of hexagonal ordering. In this case, the average diameter was difficult to calculate due to the irregular shape of the nanopillars. Based on STEM images coupled with the pillar diameter histogram data, the lower background pressure leads to more uniform nanopillar distribution (Figure 3.4a.5) while the higher background pressure leads to a wider diameter distribution (Figure 3.4b.2 and Figure 3.42c.2). The pillar alignment is

denoted in Figure 3.4a.1-c.1 with yellow arrows. Upon increasing to 100 mTorr, the nanopillar alignment appears tuned from vertical to slightly tilted. Increasing further to 200 mTorr, the pillars become more randomly orientated in the ZnO matrix. Overall, it is suggested here that lower background pressure leads to more uniform and vertically aligned pillar morphology.

X-ray diffraction was conducted to investigate the microstructure and epitaxial quality of ZnO-Au VAN. Scans of θ-2θ were performed for films deposited under different oxygen background pressure and shown in Figure 3.4e. These scans show highly textured growth with the preferred out of plane direction for ZnO is (0002) and for gold is (111), growing parallel with the (0006) plane of Al_2O_3. ZnO-Au VAN was found to have an epitaxial relationship of Au (111) || ZnO (0002) || Al_2O_3 (0006). To overcome the vastly different lattice structure, Au rotates to (111) orientation to match both the underlying substrate and the matrix. This (111) plane is the close-packed plane for the face-centered cubic lattice with six-fold symmetry, but different plane stacking sequence compared to the structure of the ZnO matrix or Al_2O_3 substrate. The hexagonal shape of the (111) orientation of Au is also evidenced in the highly-faceted Au pillar shape as seen in plan-view images. Moreover, the in-plane epitaxial relationship is determined from plan-view SAED pattern and cross-section SAED pattern in Supplement 1 and found to be Au {220} || ZnO {1-100} || {1-210}.

To investigate the strain states of the films, the out of plane d-spacing was calculated and plotted in Figure 3.4f. For ZnO matrix, increasing the background pressure decreased the d-spacing value from the bulk value of (0002), which indicated an increased compressive strain. For gold nanopillars, increased background caused d-spacing values to decrease toward the bulk value of (111), which indicated a decreased tensile stress. Interestingly, the tendency of the lattice parameter to decrease with the background pressure corresponded to increased nanopillar diameter and tuned orientation. This lattice strain tuning could be related to the morphology seen in Figure 3.4a-c. At 50 mTorr, the gold nanopillars are in a high strain state and growth is vertically aligned with both local and long-range hexagonal ordering. Gold nanopillars in the 200 mTorr are in a low strain state and have random ordering with little to no hexagonal ordering. Based on the observed morphologies, the tendency of gold to grow into highly ordered, hexagonally faceted structures is believed to be driven by high strain and a desire to reduce interfacial energy with the ZnO matrix.

In parallel to tuning oxygen pressure, a set of laser frequency study were conducted and summarized in Figure 3.6. Cross-section STEM images are shown for each frequency of Figure 3.6a.1) 2 Hz, b.1) 5Hz, and c.1) 10 Hz. Corresponding plan-view STEM image are shown for Figure 3.6a.2) 2 Hz, b.2) 5 Hz, and c.2) 10 Hz. A red hexagon in Figure 3.6c.2) in plan-view denotes the quasi-hexagonal in-plane ordering. EDS-mapping combined with STEM was performed on the plan-view 10 Hz sample to further show the distinct two-phase growth of Au and ZnO as seen in Figure 3.6c.4-6) with corresponding HAADF appearing in Figure 3.6c.3). The EDS-mapping confirms the sufficiently low interdiffusion similar to that of the background pressure series. High resolution TEM was conducted on the 10 Hz sample to demonstrate the hexagonal shape and faceted nanopillars, shown in Figure 3.6c.7), as well as the in-plane atomic arrangement. The 6 sides of the pillar are indexed as {220} family of planes.

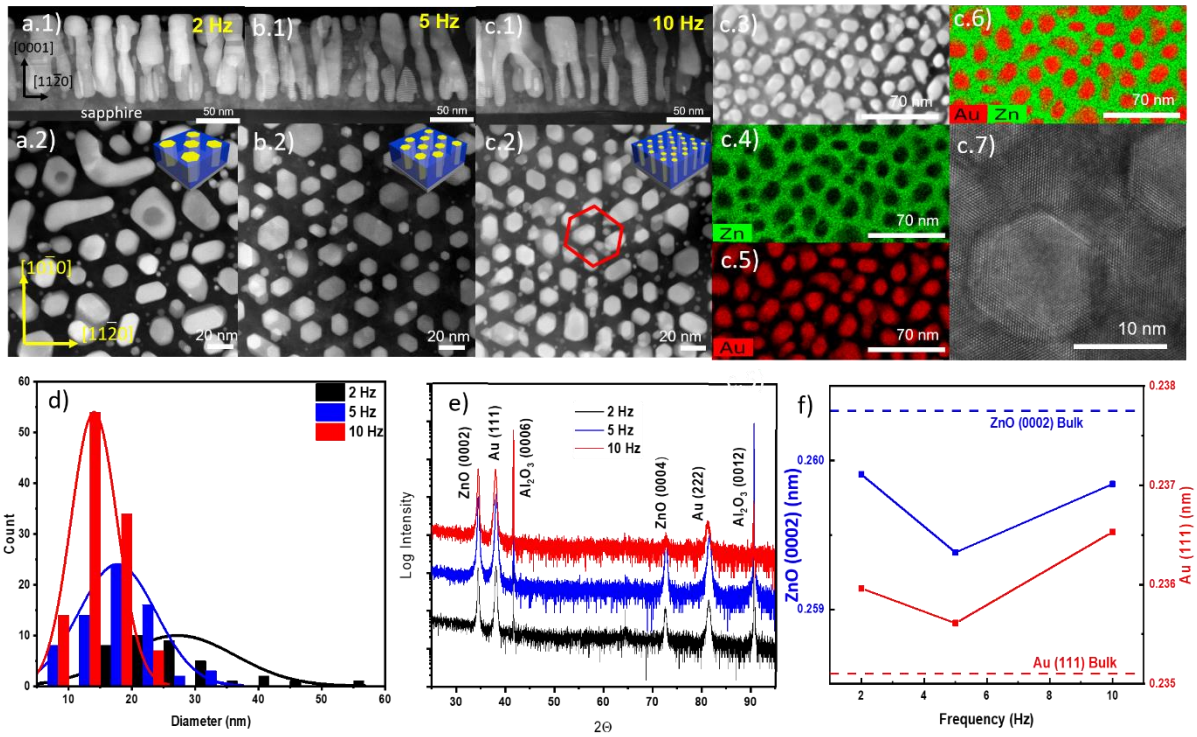

Figure 3.6 The ZnO-Au nanocomposite samples deposited under different deposition frequencies. Cross-section STEM images shown for a.1) 2 Hz, b.1) 5 Hz, c.1) 10 Hz). Plan-view STEM image are shown for a.2) 2 Hz, b.2) 5 Hz, and c.2) 10 Hz. A red hexagon is placed in c.2) to denote quasi-hexagonal ordering. c.3) Corresponding HAADF for EDS-mapping of 10 Hz. EDS-mapping for c.4) Zn, c.5) Au, and c.6) combined. c.7) plan-view HRTEM of individual Au nanopillar and ZnO matrix obtained from 10 Hz sample. d) Calculated histogram of measured pillar diameters. e) XRD study. d) Basal plane d-spacing calculation. f) Basal plane d-spacing calculated from e).

To understand the effect of frequency on epitaxial quality and microstructure, a detailed XRD study was performed with scans shown in Figure 3.6e and out of plane d-spacing values were calculated in Figure 3.6f. The average diameters were calculated by a similar method as highlighted above and plotted as a histogram in Figure 3.6d. The films grown had diameter of 27 nm, 18 nm, and 15 nm for deposition at 2 Hz, 5 Hz, and 10 Hz, respectively. As frequency is increased, statistically the diameter of gold nanopillars is decreased. This is observed from plan-view STEM images in Figure 3.6a.2-c.2. It is suggested here that increasing the pulse frequency will shorten diffusion length of impinged adatoms. Increased frequency will impede the ability of adatoms to reach thermodynamic equilibrium, creating disorder and strain in the film. This is observed with XRD scans in Figure 3.6e and the calculated d-spacing in Figure 3.6f. For the 2 Hz film, ZnO d-spacing is close to the bulk value of (0002) but as frequency is increased to 5 Hz and 10 Hz, the d-spacing decreases, indicating an increase in compressive stress. Conversely, the d-spacing of (111) gold at 2 Hz is greater than the bulk value and gradually increases with frequency, indicating an increase in the out-of-plane tension of nanopillars.

The advantage of the film grown in this report is the inherent anisotropy and strain engineering, which leads to hyperbolic dispersion and epsilon near zero permittivity. Strong plasmonic resonance is expected at the ZnO/Au interface, making the ZnO-Au hybrid material useful for different types of gas sensors and energy harvesting [102,212]. Due to the excellent epitaxial quality, as seen in XRD scans above for deposited ZnO-Au VAN, the optical properties are expected to be enhanced as compared with other metallic nanowire arrays and ZnO-Au nanocomposites. To directly observe plasmonic resonance of ZnO-Au VAN, UV-Vis transmittance spectra were obtained. Results of the films deposited at different background pressure are shown in Figure 3.7 and those for different laser frequency are shown in Figure 3.7b. There is an obvious surface plasmon resonance (SPR) caused by gold in the transmittance spectra, occurring at around 600nm. The red shift of the plasmon resonance in the case of background pressure spectra in Figure 3.7a correlates with randomization of nanopillar orientation and caused by a broadening of the absorption edge. The transmission (T%) overall decreases for films at higher background pressure, possibly due to more light being scattered and absorbed by the film because of increased pillar size and changed orientation. Optical band gap values were calculated via a Tauc plot method to investigate the effect gold inclusion had on ZnO optical band gap. The band gaps calculated for oxygen pressure are shown in Figure 3.8a.

There is no obvious trend in the optical band gap tuning with respect to background pressure tuning.

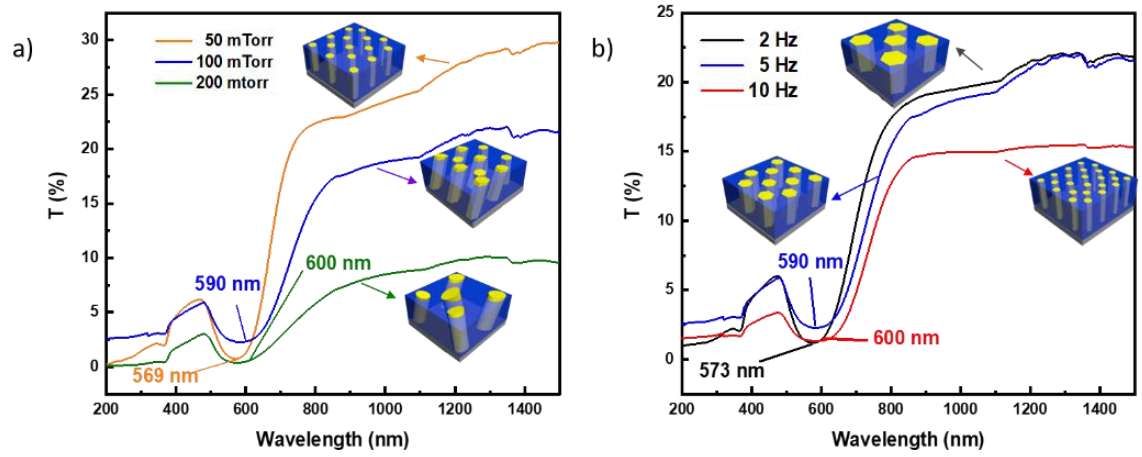

Figure 3.7 UV-Vis transmission (%T) spectra of ZnO-Au VAN in the range of 200-1500 nm with changes of a) oxygen background pressure and b) laser frequency. Insets on each graph are models depicting each nanocomposite. The minimum in the graph represents the plasmonic response of Au and was measured and recorded for each film on the respective graph.

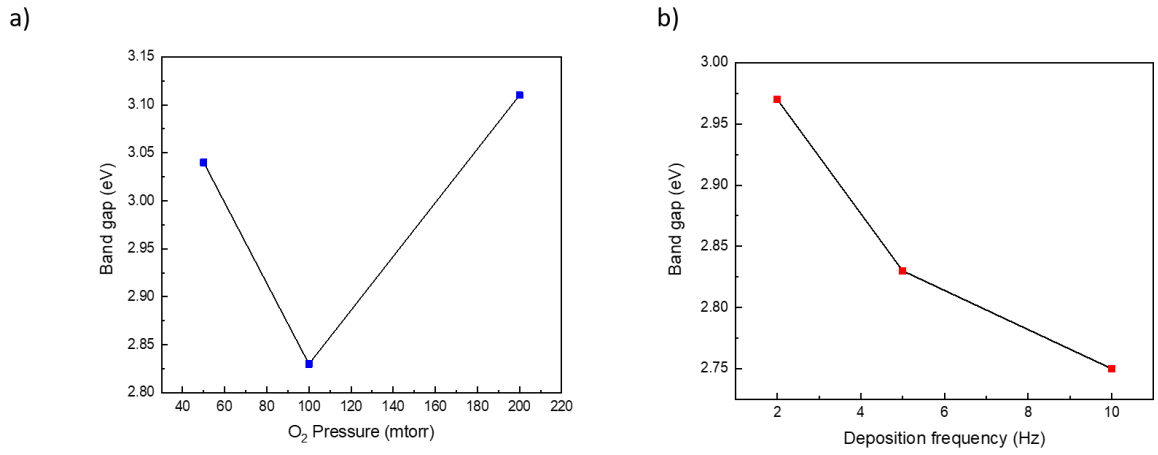

Figure 3.8 Optical band gap were calculated via a Tauc plot method from obtained transmission data. Band gap is shown for a) oxygen background pressure and b) laser frequency.

Transmission spectra were also obtained for films deposited at different laser pulse frequency and presented in Figure 3.7b. Plasmon resonance peak is red shifted as laser pulse frequency is increased from 2 Hz to 10 Hz, which correlates to smaller pillar diameter. The absorption edge

slightly broadens as frequency is increased, possibly due to an increased number of Au nanopillars. The surface plasmon minima also broadens with increasing background pressure, possibly caused by a higher level of strain. Optical band gaps were calculated for frequency variation films and plotted in Figure 3.8b. As frequency increases, optical band gap decreases. The ZnO-Au film deposited at 10 Hz has a higher density of pillars than the film deposited at 2 Hz. A higher density of pillars could create more interfaces, increasing the amount of light that is scattered and decreasing the optical band gap. While there is a general trend of red-shifting of the plasmon resonance peaks, this is based on observation from the measured spectra.

The hyperbolic properties observed in optical metamaterials are a direct result of the isofrequency surface of extraordinary waves, which is given by the following formula:

$$\frac{k_x^2+k_y^2}{\varepsilon_{\parallel}} + \frac{k_z^2}{\varepsilon_{\perp}} = \left(\frac{\omega}{c}\right)^2 \quad [181]$$

The hyperbolic dispersion and ENZ permittivity of ZnO-Au VAN was investigated through spectroscopic ellipsometry. The real part of the dielectric function, related to the permittivity of the film, is presented in Figure 3.9. Representative isofrequency curves, which determine the photonic density of states that can be supported within the material, are shown in each graph. The regions are color coded to their corresponding surface of either a hyperboloid of two sheets (blue shaded color) or a hyperboloid of one sheet (red shaded color). Data was measured from 210nm – 2500 nm at three different angles of 30°, 45°, and 60°. The data was fitted with a uniaxial model to discern the in-plane and out of plane components of the dielectric function. A B-spline model was used on both in-plane and out-of-plane and a reasonable mean square error (MSE) < 5 occurred for all films. Ellipsometry parameters psi and delta are shown in Figure 3.10 and Figure 3.11, respectively. The anisotropy axis is shown for each experimental setup in a,b,c,d with the subscripts || and ⊥ indicating respectively the components parallel (in-plane) and perpendicular (out of plane) to the anisotropy axis.

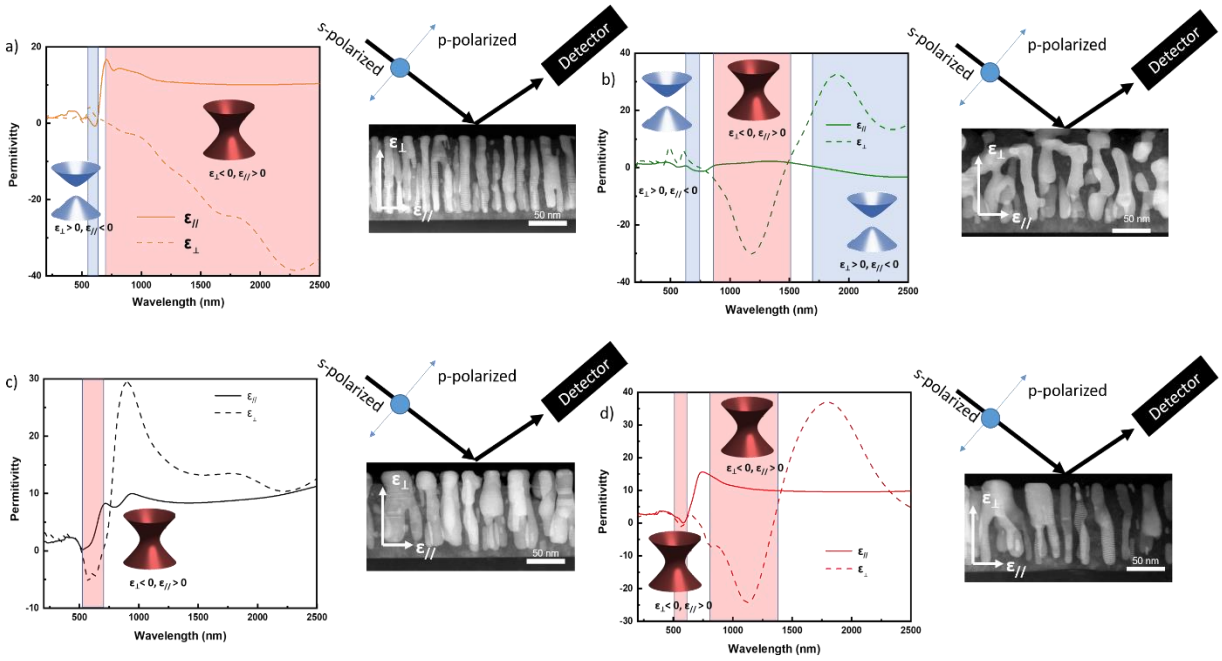

Figure 3.9 The real part of ε// and ε⊥ are graphed for a) 50 mTorr, b) 200 mTorr, c) 2 Hz, and d) 10 Hz. Regimes of hyperbolicity are marked on the graphs in both red and blue corresponding to the respective isofrequency curve of either a hyperboloid of two sheets (blue) or hyperboloid of one sheet (red). In a, b, c, d is shown the polarization of the beam experiment with respect to the microstructure of each film. Marked on the cross-section STEM image are the parallel and perpendicular direction of permittivity.

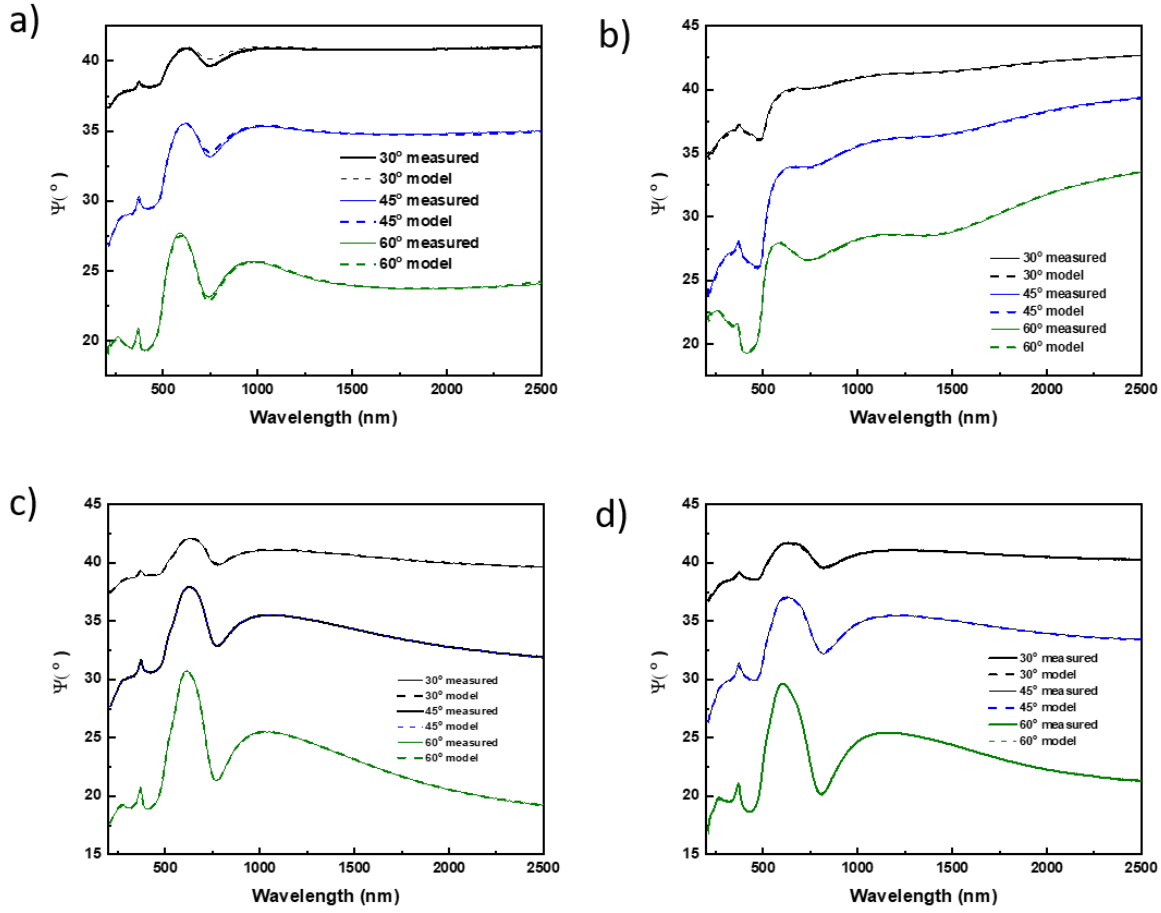

Figure 3.10 Measured and model fitting for psi obtained from spectroscopic ellipsometry. Graph are for a) 50 mTorr, b) 200 mTorr, c) 2 Hz, and d) 10 Hz.

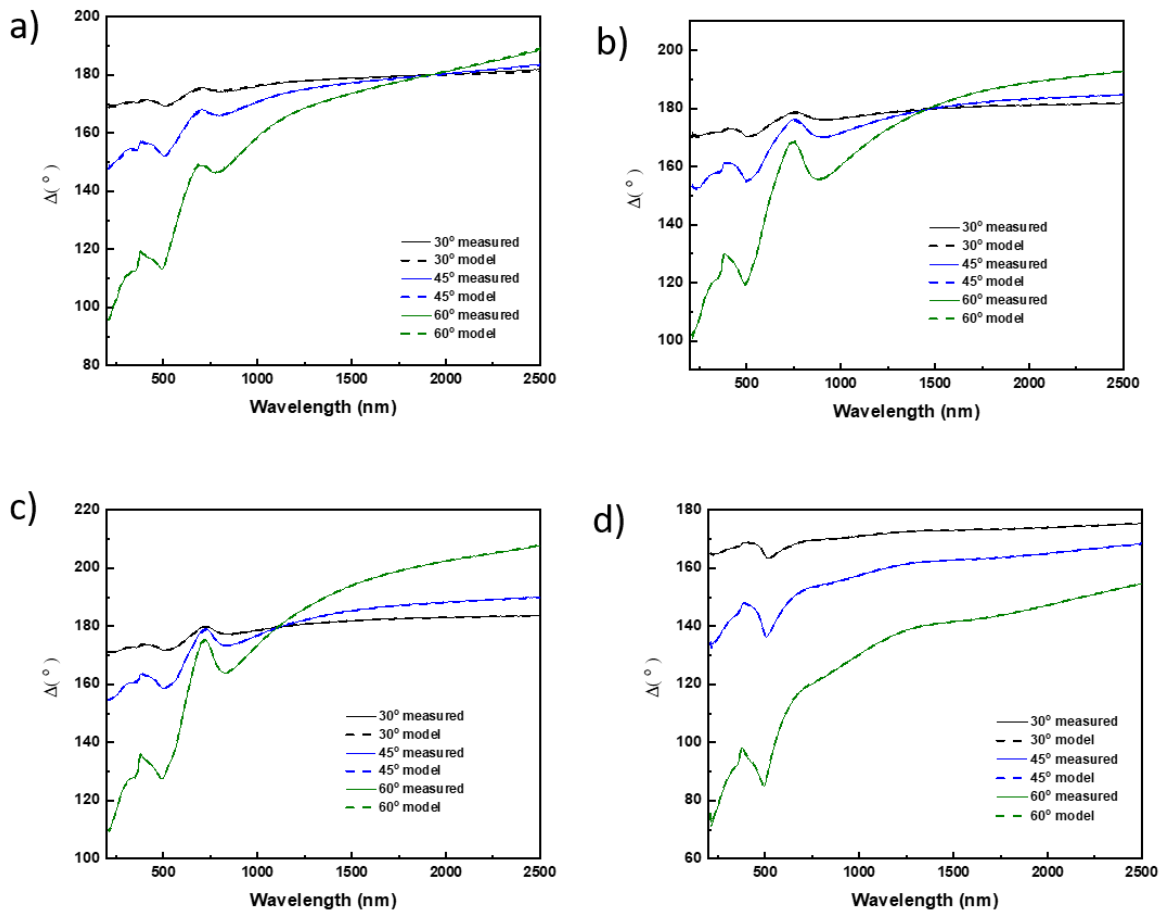

Figure 3.11 Measured and model fitting for delta obtained from spectroscopic ellipsometry. Graph are for a) 50 mTorr, b) 200 mTorr, c) 2 Hz, and d) 10 Hz.

The ZnO-Au films grown in this work all have hyperbolic dispersion and ENZ points across many different ranges, but most interestingly they all have it in shorter wavelength (visible) regime. The permittivity of the film deposited at 50 mTorr is shown in Figure 3.9a and permittivity of the 200 mTorr film is shown in Figure 3.9b. The film grown at 50 mTorr shows hyperbolic dispersion in the visible spectrum and in the near infrared regime up to the far end of the measured spectrum. In the 50 mTorr film, $\varepsilon_{//}$ (in-plane component) behaves mostly as a dielectric material except for in the visible regime from around 500-700nm, where $\varepsilon_{//}$ is driven negative, caused by the surface plasmon resonance. The perpendicular component $\varepsilon_{\perp}$ (out of plane) has a permittivity with strictly metallic behavior. The 50 mTorr film in the visible regime has hyperbolic dispersion with an isofrequency surface of a hyperboloid of two sheets (blue shaded color) and in the near infrared regime, the surface is tuned to become a hyperboloid of one sheet (red shaded color). The 50 mTorr film also has three ENZ points, two in the parallel direction in the visible regime at 520 nm and 625 nm and the perpendicular component has one ENZ point in the visible regime at 715 nm. The hyperbolic properties of the 50 mTorr film correlate well with the overall hexagonal ordered, vertically aligned morphology. Vertically aligned gold metallic nanopillars cause the perpendicular permittivity to be negative and the ZnO dielectric media is expressed in the parallel component having positive permittivity. When gold nanopillar morphology is tuned by growth at 200 mTorr to be randomly arranged in Figure 3.9b, this leads to an increased number of epsilon-near zero (ENZ) points in the visible and infrared spectrum. The parallel component has ENZ points of 657, 835, and 1762 nm, while the perpendicular component has ENZ points at 744 and 1468 nm. It is also possible to change the hyperbolic isofrequency surface in the long range (above 1500nm) from a hyperboloid of one sheet in the 50 mTorr film to a hyperboloid of two sheets in the 200 mTorr film. The 200 mTorr film has an interesting parallel component with almost near zero permittivity for the entire measured spectrum regime. It oscillates between being slightly negative and slightly positive while crossing zero permittivity at three different points, though it never has a permittivity outside of +/- 3. A material with epsilon near zero permittivity and hyperbolic dispersion across a broad-spectrum range is of particular interest for sub-diffraction imaging or other hyperbolic metamaterial application [213].

The effect of frequency tuning on hyperbolic dispersion was also investigated. The permittivity of the film grown at 2 Hz is shown in Figure 3.9c, in which the film only has a small

hyperbolic regime in the visible spectrum and the perpendicular component has ENZ points at 515 and 697 nm. Upon increasing laser frequency, the number of ENZ points increases and the film demonstrates hyperbolic dispersion in the near infrared. The perpendicular component has ENZ points at 542, 595, 716, and 1348 nm. Tuning pulse laser deposition frequency changes the size and number of hyperbolic regimes, but it does not tune the overall isofrequency surface geometry. As compared with the background pressure series of films, the pulse laser frequency series does not have as good of hyperbolic properties, but the series does have significant epsilon-near zero permittivity points.

Parallel systematic tuning experiments of pulsed laser frequency and oxygen background pressure were designed to investigate the effect on strain states and morphology in ZnO-Au VAN structure, as per Figure 3.1. Frequency dependence was selected as one of studies because it is well known to affect oxide-metal VAN diameter [207], where the diameter of nanowires has been highly-correlated with optical properties [214]. Conversely, background pressure was studied because its effect on oxide-metal VAN has not yet been studied. Individual gold nanopillars in matrix grown at high strain states were shown to have beautiful, faceted, hexagonal structure and long-range quasi-hexagonal in-plane order. Of the two series of films of oxygen background pressure and laser frequency, each series demonstrated an ability to tune the hyperbolic properties of the films in unique ways. There are a few key conclusions that can be surmised when considering the background pressure series and the pulse laser frequency series. Overall, the background pressure series shows broader hyperbolic properties in both shorter and longer wavelengths compared with the pulse laser frequency series, which is ideal for tunable hyperbolic metamaterials application. Changing the background pressure from 50 mTorr to 200 mTorr allows the isofrequency surface to be tuned. Easily controllable isofrequency curve in the visible and infrared regime is something not previously demonstrated. Manipulating the isofrequency surface is important because it is useful in application for focusing in hyperlenses and subdiffraction imaging [215]. In the pulse laser frequency series, by changing the deposition frequency from 2 Hz to 10 Hz, this created a hyperbolic regime in the infrared and increased the number of epsilon near-zero permittivity points. Overall, the background pressure series demonstrated superior hyperbolic metamaterials properties and wider application when compared with the pulse laser frequency series. The key issue facing hyperbolic metamaterial in their application include small hyperbolic regimes, controllability, and lack of properties in

visible regimes. The background pressure series solves most of these key issues; it demonstrates broad hyperbolicity in both short and long wavelengths, and through manipulation of morphology and the quasi-hexagonal in-plane ordering in these films, it is possible to easily control metamaterial properties.

3.5 Conclusion

Two-phase ZnO-Au VAN films have been grown through a simple, self-assembly one-step PLD method. ZnO-Au nanocomposites morphology demonstrated beautiful, vertically aligned gold pillars with quasi-hexagonal in-plane ordering that were embedded in a ZnO matrix. The effect of PLD parameters on film morphology and strain was investigated through different experimental growth series, an oxygen background pressure series and a pulse laser frequency series. Background pressure showed an ability to tune the orientation and ordering of the gold nanopillars, while pulse frequency was able to tune the size of pillars. High strain states lead to small pillar size and a high degree of quasi-hexagonal in-plane ordering, while low strain states induce decreased ordering and large pillar size. ZnO-Au VAN due to its anisotropy and strain driven hexagonal-closed packed ordering demonstrate interesting hyperbolic dispersion and epsilon near zero (ENZ) permittivity in both the visible and near-infrared regimes. Plasmonic properties are shown to be easily controlled through morphology. As well, ZnO-Au VAN was found to have excellent epitaxial quality, lending to enhanced optical properties and potential energy and sensor application. Future work will focus on application of the ZnO-Au VAN in sensor and metamaterials technologies.

4. VERTICALLY-ALIGNED AG_X-AU_{1-X} ALLOYED NANOPILLARS EMBEDDED IN ZNO AS NANOENGINEERED LOW-LOSS HYBRID PLASMONIC METAMATERIALS

4.1 Overview

Hybrid plasmonic metamaterials offer a pathway to exotic properties and technologically important applications including subdiffraction imaging and plasmonic energy harvesting. Challenges remain towards practical application including high absorption losses of noble metals and tedious growth / fabrication processes. In this work, a self-assembled hybrid plasmonic metamaterial consisting of anisotropic Ag_xAu_{1-x} alloy nanopillars embedded in a ZnO matrix has been successfully grown. Chemical composition of the nanoalloy was determined to be $Ag_{61}Au_{39}$. The microstructure and optical properties arising from ZnO-$Ag_{61}Au_{39}$ alloyed hybrid systems were investigated and compared with that of the ZnO-Ag particle-in-matrix nanocomposite and the ZnO-Au vertically aligned nanocomposite. ZnO-$Ag_{61}Au_{39}$ hybrid system demonstrates anisotropic morphology, excellent epitaxial quality, and enhanced optical properties including surface plasmon resonance, hyperbolic dispersion, low absorption losses, and numerous epsilon-near zero permittivity points making it a promising candidate for practical applications of hybrid plasmonic metamaterials.

4.2 Introduction

Hyperbolic metamaterials are a class of materials demonstrating unique dielectric function owing to their anisotropic nanostructure. The nanostructures consist of periodic arrangements of negativity leading to hyperbolic dispersion, in which one direction the dielectric function will have as a metal and as a dielectric material in the opposite direction. Potential applications of hyperbolic metamaterials include subwavelength wave-guides [170], subdiffraction imaging [165,216], cloaking [171], and platforms for studying fundamental physical

phenomenom [168,185]. The most popular approaches for realizing practical hyperbolic metamaterials are through layered dielectric-metal nanocomposites [179,213,216] and nanowire arrays [141,169,187,214]. Owing to the plasmonic-coupling at the metal-dielectric heterointerface, nanostructured hyperbolic metamaterials have multifunctionalities not only as metamaterials but also in energy harvesting and sensor technologies [181,217–220], i.e. hybrid plasmonic metamaterials. Layered dielectric-metal nanocomposites have the advantage of being well-studied, but require top-down multi-step depositions and are limited by materials selection [155,213]. Conversely, nanowire arrays offer a promising bottom-up approach for realizing practical applications by the recently demonstrated oxide-metal vertically-aligned nanocomposite (VAN) morphology [143,145,221]. Two-phase (VAN) thin films are functional materials consisting of nanopillars of one phase embedded in the matrix of the second phase, leading to unique multifunctionalities and highly anisotropic morphology and properties [104–106,111,114,115,143,206,207,222]. The VAN approach offers benefits over top-down nanowire array growth methods [153,202–204] including one-step self-assembly through pulsed laser deposition (PLD) technique, robust materials selection, and extensive tailorable morphology.

The major limitation of metallic plasmonic metamaterials in practical applications is the high absorption losses of plasmonic noble metals such as Ag and Au [143,181]. Using nanostructured low-loss metals is proposed as one way to overcome absorption losses. Some promising candidates include nanostructured aluminum [223,224] and copper [225]. While these metals are promising, they suffer from chemical and thermal instability issues. Another proposed but less studied way is utilizing nanoalloys [154,226–228]. Nanoalloys are a strong candidate for hybrid plasmonic metamaterials, however they also suffer from chemical and thermal instability issues [229,230]. It could be possible to achieve a stable nanoalloy by combining it with a chemically stable oxide matrix.

In this work, we propose nanoscale alloying of the metallic constituent of oxide-metal VAN for a two-fold effect. The first is to create enhanced hybrid plasmonic metamaterials by utilizing nanoalloys for improved optical response and tunability [227,231] in oxide-metal VAN. Nanoalloys suffer from thermal stability issues in high temperatures, preventing them from advanced application [229]. Encapsulation in an oxide matrix will provide a platform for plasmonic hybridity and enhanced chemical and thermal stability. The second purpose of alloying the oxide-metal hybrid material is to enable vertically aligned nanocomposite (VAN)

growth to overcome the typical particle-in-matrix oxide-metal form. Exotic functionalities of metamaterials depend on the strong anisotropy in the VAN nanostructures while many of the oxide-metal hybrid materials prefer to grow as isotropic particle-in-matrix structure [145,232], limiting their anisotropic nature. By properly selecting the alloy composition with a metal preferring pillar structure, it is possible to facilitate the pillar-in-matrix growth for superior combined properties and microstructure.

For this demonstration, we have selected Ag_xAu_{1-x} alloyed nanopillars embedded in ZnO matrix as a VAN through a single-step pulsed laser deposition (PLD) technique, schematically shown in Figure 4.1. Ag_xAu_{1-x} was chosen as the nanoalloy for this demonstration because of the widely studied plasmonic properties of Au and Ag [233]. Ag has lower optical losses than Au [234], however it is chemically unstable [231]. Alloying Ag together with Au helps combine the optical properties of Ag with the chemical stability of Au [226,227]. ZnO was selected as the dielectric medium as it is widely-available and a well-studied photocatalytic and energy-harvesting material [72,209]. As shown in Figure 4.1, ZnO-Ag and ZnO-Au were grown and compared to ZnO-Ag_xAu_{1-x}. ZnO-Ag has a preferred particle-in-matrix microstructure while ZnO-Au grows as a pillar-in-matrix structure. Alloying Ag with Au in the ZnO matrix will grow ZnO-Ag_xAu_{1-x} with vertical, anisotropic microstructure as seen in Figure 4.1. The microstructure of ZnO-Ag, ZnO-Au, and ZnO-Ag_xAu_{1-x} were carefully investigated and compared. The optical properties were measured and compared with single metal cases to demonstrate the structure and property tunability.

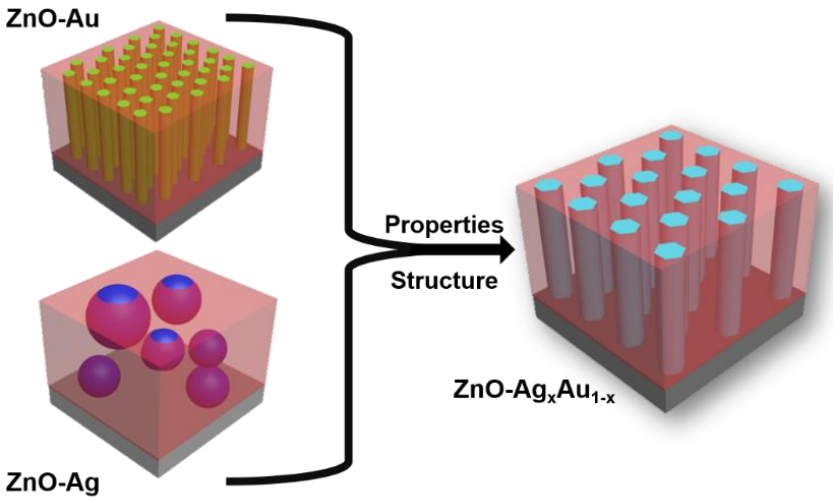

Figure 4.1 Schematic diagram of oxide-alloyed metal vertically aligned nanocomposite. The alloy VAN approach enables the growth of ZnO-Ag type nanoalloy pillar-in matrix to produce a new meta-film with anisotropic morphology and broad optical properties.

4.3 Experimental

4.3.1 Thin film growth

ZnO-Au, ZnO-Ag, and ZnO-$Ag_{61}Au_{39}$nanocomposite films were grown on c-cut Al2O3 (0001). Deposition was performed with a KrF excimer laser (Lambda Physik Complex Pro 205, λ = 248 nm) and substrate temperature was kept constant at 500 ^{o}C. The laser beam was focused with an incident angle of 45o with a laser energy of 420 mJ. The target-substrate distance was kept constant at 4.5 cm and measured before each deposition to ensure accuracy. Three nanocomposite targets consisting of ZnO-Ag, ZnO-Au, and ZnO-$Ag_{50}Au_{50}$were developed through solid-state sintering used for laser ablation. Before deposition, the chamber was pumped down to around 10-6 mTorr before an oxygen pressure was inflowed. Oxygen background pressure was maintained at 20 mTorr and laser pulse frequency was set to 5 Hz for all deposition After all depositions, the chamber was cooled to room temperature at a rate of 15 ^{o}C/min.

4.3.2 Microstructure Characterization

Film morphology was characterized through XRD, TEM, and STEM coupled with EDS-mapping. XRD scans of θ-2θ were conducted using a Panalytical X'Pert X-ray diffractometer wit Cu Kα radiation. Bright field TEM, STEM, SAED patterns and EDS-mapping was performed in a FEI Talos F200X TEM. Samples for electron microscopy were prepared, for both cross-section and plan-view, via a standard grinding procedure which entails manual grinding, polishing, dimpling, and a final ion milling step to achieve electron transparency. (PIPS 691 precision ion polishing system, 5 KeV for cross-section and 4-4.5 KeV for plan-view sample)

4.3.3 Optical measurements

Ellipsometry experiments were carried out on an RC2 Spectroscopic ellipsometer (J.A. Woollam Company). Three angles 30o, 45o, and 60o were measured from a spectrum range of 210 – 2500 nm. Psi and delta data were obtained from ellipsometry experiments and then fit with an uniaxial model coupled with B-spline model were used to discern anisotropic permittivity properties of ZnO-Au, ZnO-Au, and ZnO-Ag_xAu_{1-x}, an agreeable mean square error (MSE) < 5 was obtained for all film models. Normal incident depolarized transmittance (T%) was measured using an optical spectrophotometer (Lambda 1050 UV-vis spectrophotometer).

4.4 Results and Discussion

The challenge of alloying at the nanoscale was overcome by selecting compatible alloy constituents that were immiscible in the ZnO matrix. For comparison, ZnO-Ag and ZnO-Au hybrid materials were grown at the same parameters as ZnO-Ag_xAu_{1-x} on α-Al_2O_3 [0001] substrate (see 4.3.1). The chemical composition of the nanoalloy was determined through Energy Dispersive Spectroscopy (EDS) and found to be $Ag_{61}Au_{39}$, the resulting table can be found in Table 4.1. ZnO-Ag particle-in matrix can be seen in the cross-section scanning transmission electron microscopy (STEM) image in Figure 4.2a and plan-view in Figure 4.2d. Depicted in STEM images, the morphology of ZnO-Ag is particle-in matrix. The inset SAED pattern in Figure 4.2a shows low epitaxial quality of ZnO-Ag particle-in matrix nanocomposite. There are satellite diffraction peaks, caused by minor orientations of Ag and ZnO. Figure 4.2b shows vertical and well-ordered Au nanopillars inside a ZnO matrix. Plan-view STEM in Figure 4.2e shows individual Au nanopillars with hexagonal shape and mesoscale quasi-hexagonal in-plane

ordering. The inset image shows the SAED pattern, with diffraction spots from Au, ZnO, and Al_2O_3, indicating the high epitaxial quality, with the out-of plane epitaxial relationship being Al_2O_3 (0006) || ZnO (0002) || Au (111) and in-plane relationship is Al_2O_3 || ZnO (01-10) || Au (20-2) . High epitaxial quality like in ZnO-Au is preferred as it leads to enhanced optical properties [234]. EDS chemical mapping of ZnO-Au and ZnO-Ag can be found in Figure 4.3, showing no inter-diffusion between phases. Successful oxide-nanoalloy ZnO- $Ag_{61}Au_{39}$VAN growth is presented in Figure 4.2c,f. The cross-section STEM indicates vertical growth of the alloyed phase while the inset SAED pattern shows the high epitaxial quality and same out-of plane and in-plane epitaxial relationship maintained from ZnO-Au nanocomposite. Comparing microstructure indicates that alloying is an effective approach to induce pillar-in matrix morphology for materials like Ag that grow with preferred particle-in matrix morphology. Furthermore, it is possible to tune the alloy composition through varying the target stoichiometry or through growth parameters. For demonstration, the background pressure was tuned and besides the $Ag_{61}Au_{39}$ nanoalloy deposited at 20 mTorr, two other composition of $Ag_{33}Au_{67}$ and $Ag_{67}Au_{33}$ were determined for deposition in vacuum and 150 mTorr, respectively. The graph of the Ag/Au ratio vs deposition pressure of these films can be seen in Figure 4.4a, which was calculated from EDS data shown in Table 4.1,

Table 4.2, and Table 4.3.A ratio of Ag/Au < 1 implies the alloy is Au-rich while a ratio of Ag/Au > 1 implies the alloy is Ag-rich.

Table 4.1 Tabulation of silver, gold, and zinc composition for ZnO-$Ag_{61}Au_{39}$ by energy dispersive spectroscopy (EDS).

Element	series	Net	[wt.%]	[norm. wt.%]	[norm. at.%]	Error in wt.% (3 Sigma)
Silver	K-series	8	26.00447	26.00447	28.84612	32.00971
Gold	L-series	112	52.56009	52.56009	31.92977	25.43802
Zinc	K-series	79	21.43544	21.43544	39.22411	8.10837
		Sum:	100	100	100	

Table 4.2 The compositions of Ag, Au, and Zn for the ZnO-Ag_xAu_{1-x} film deposited in vacuum by energy dispersive spectroscopy (EDS).

Element	series	Net	[wt.%]	[norm. wt.%]	[norm. at.%]	Error in wt.% (3 Sigma)
Silver	K-series	8	26.00447	26.00447	28.84612	32.00971
Gold	L-series	112	52.56009	52.56009	31.92977	25.43802
Zinc	K-series	79	21.43544	21.43544	39.22411	8.10837
		Sum:	100	100	100	

Table 4.3 Compositions of Ag, Au, and Zn for the ZnO-Ag_xAu_{1-x} film deposited in 150 mTorr by energy dispersive spectroscopy (EDS).

Element	series	Net	[wt.%]	[norm. wt.%]	[norm. at.%]	Error in wt.% (3 Sigma)
Gold	L-series	192	26.0194	26.0194	13.84054	10.90774
Silver	K-series	49	51.3143	51.3143	49.84183	24.5564
Zinc	K-series	287	22.6663	22.6663	36.31763	4.842717
		Sum:	100	100	100	

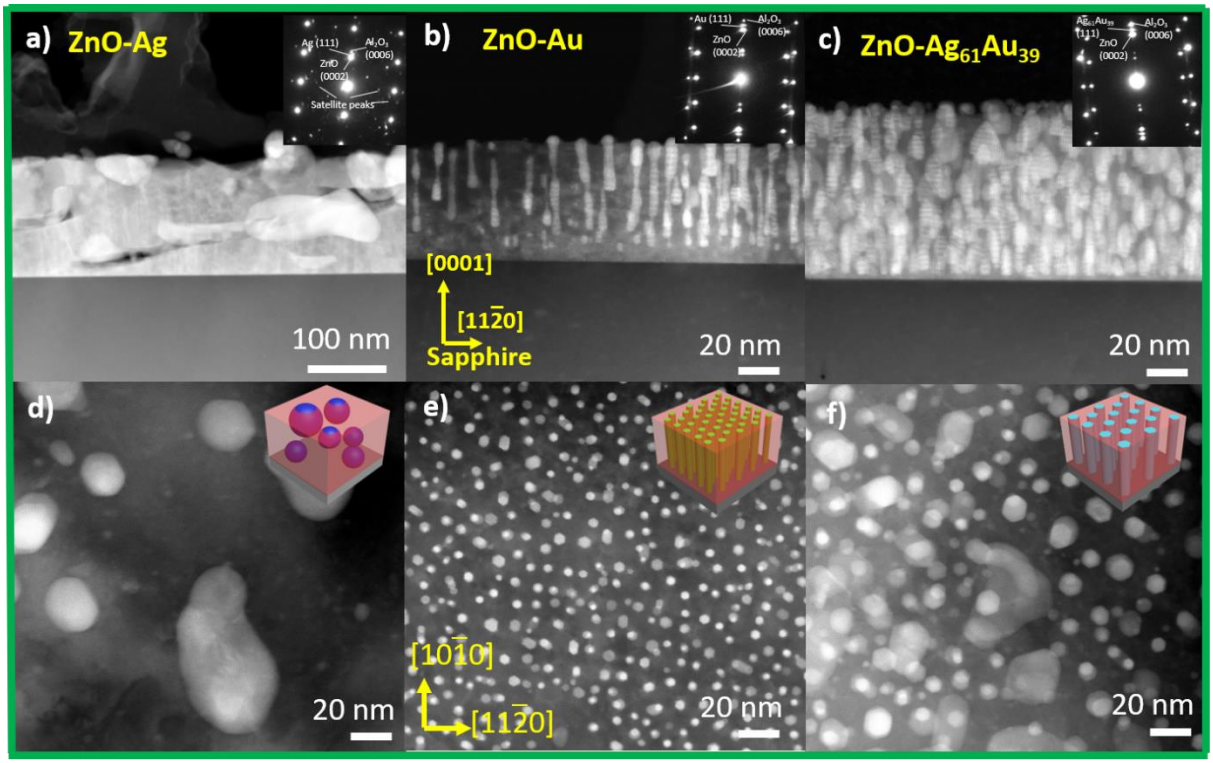

Figure 4.2 Comparison study of ZnO-Ag, ZnO-Au, ZnO- $Ag_{61}Au_{39}$. Cross section images of a) ZnO-Au, b) ZnO-Ag, and b) ZnO- $Ag_{61}Au_{39}$. Inset are the corresponding SAED patterns. The bottom row of plan-view images corresponds to d) ZnO-Au, e) ZnO-Ag, and f) ZnO- $Ag_{61}Au_{39}$. Inset are models of corresponding films.

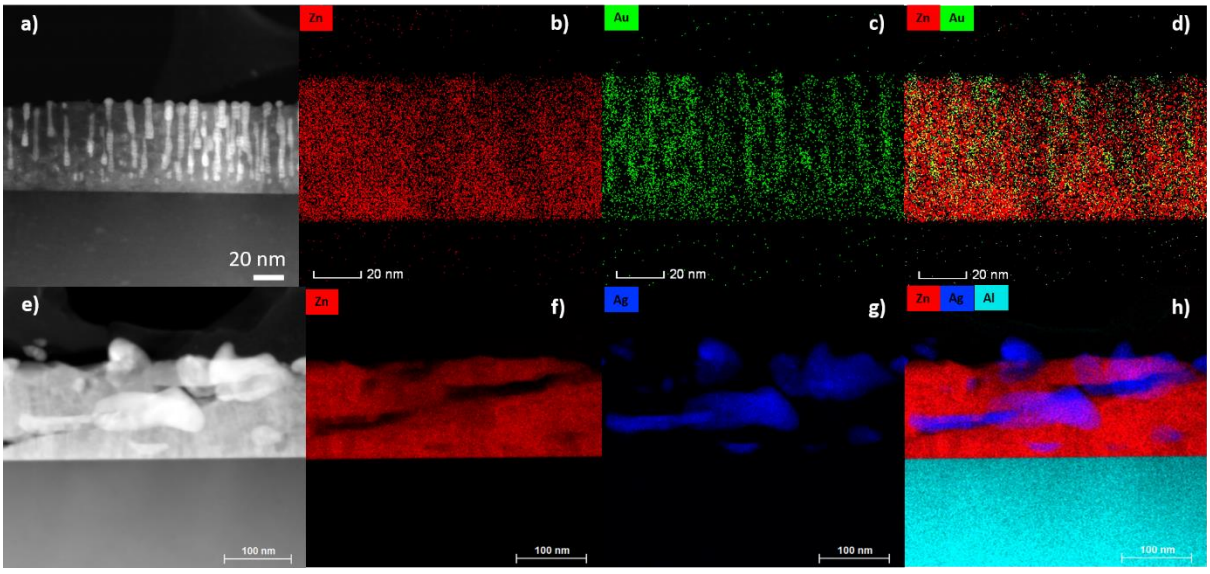

Figure 4.3 EDS mapping of ZnO-Au and ZnO-Ag. A) HAADF cross-section image of ZnO-Au, VAN, b) Zn map for ZnO-Au, c) Au map in ZnO-Au, c) combined map for ZnO-Au. E) HAADF image of ZnO-Ag, f) Zn map for ZnO-Ag, g) Ag map for ZnO-Ag h) combined ZnO-Ag map.

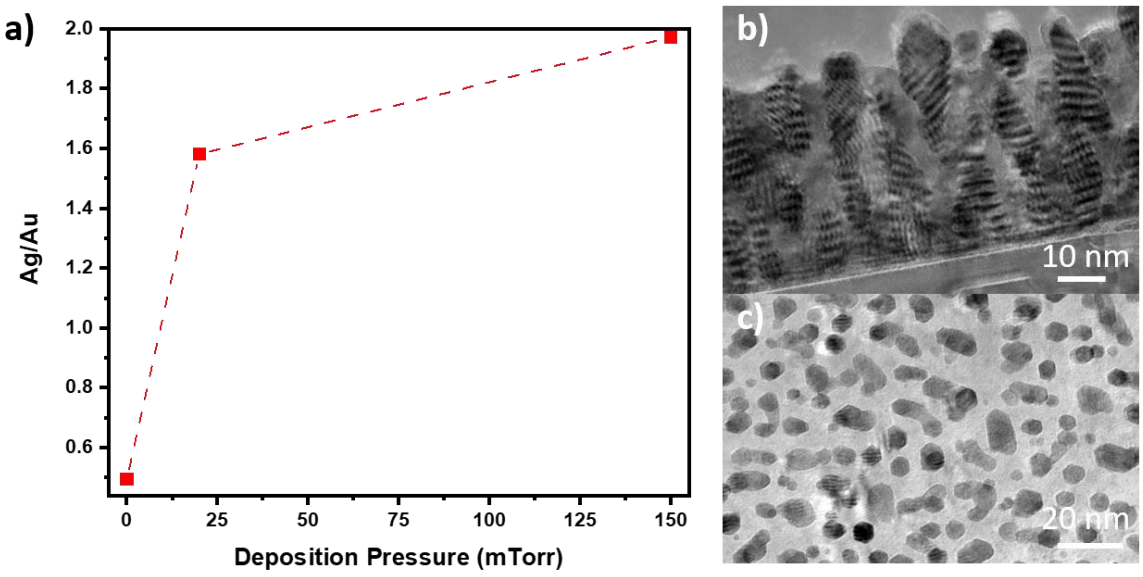

Figure 4.4 A) Graph of Ag/Au ratio vs deposition pressure for different ZnO-Ag_xAu_{1-x} thin films. b) Cross-section TEM of vacuum deposited ZnO-$Ag_{33}Au_{67}$ VAN. c) Plan-view TEM image of vacuum deposited ZnO-$Ag_{33}Au_{67}$ VAN.

X-ray diffraction (XRD) scans of the films and their targets were performed to investigate the microstructure and epitaxial quality, to discern at what stage alloying occurred, in the target or during PLD growth. Scans of θ-2θ were conducted and presented in Figure 4.5, all films show epitaxial quality aligned along the underlying substrate. ZnO grows in a wurtzite structure with preferred orientation (0002) out-of plane and aligned with the (0006) plane of Al_2O_3. Both Au and Ag have face-centered cubic (fcc) structure and rotate with respect to the matrix and substrate to expose and grow the cubic close packed (111) out-of plane. The epitaxial relationship can be surmised as ZnO (000l) || Ag or Au (lll) || Al_2O_3 (000l). This epitaxial relationship carries over to the alloyed ZnO-$Ag_{61}Au_{39}$ VAN, indicating as well that the alloy sample maintains the same fcc structure as either the Au and Ag. Scans were also performed on the individual targets to compare the alloy target in b). The purpose of investigating the targets was to determine if alloying occurred pre- or post-deposition. Comparing the target scans in b) was inconclusive, since the XRD peaks of Ag and Au occur at approximately the same position.

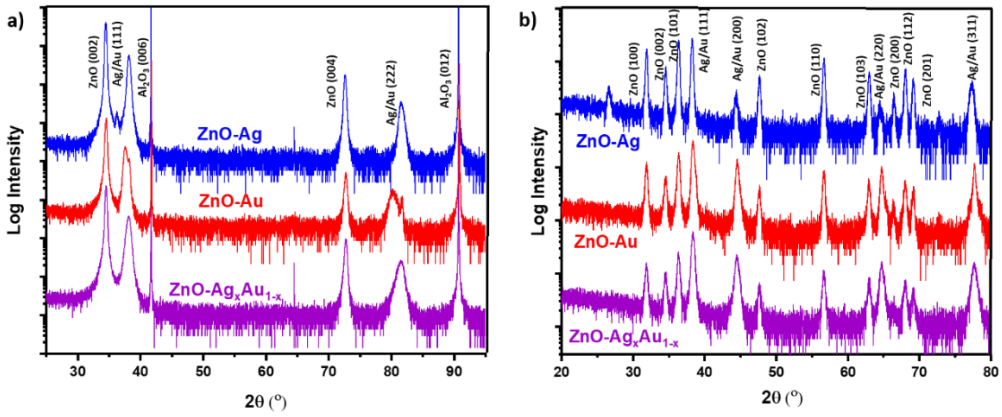

Figure 4.5 Scans performed through X-ray diffraction of θ-2θ on a) nanocomposite films and b) PLD targets.

The alloyed growth in Figure 4.2c has a few interesting microstructural characteristics compared to the vertical ZnO-Au growth. The major difference when comparing ZnO-Au and ZnO- $Ag_{61}Au_{39}$ is apparent in the plan-view image. The alloyed pillars of ZnO- $Ag_{61}Au_{39}$ maintained a similar hexagonal shape and quasi-hexagonal ordering, however nanoalloy pillars were larger than Au pillars in the ZnO-Au nanocomposite. The average diameter of ZnO-Au and ZnO- $Ag_{61}Au_{39}$ pillars was calculated, and the distribution of the pillar diameter is plotted in Figure 4.6. Diameter calculations were conducted by measuring the diameter of nanopillars via 3DS micrograph software in plan-view images in Figure 4.2 and plotting them as a histogram in Figure 4.6. This method is adopted from calculation of particle size distributions [235]. ZnO-Au pillars have an average diameter of 6.14 nm while ZnO-$Ag_{61}Au_{39}$ pillars have an average diameter of 13.7 nm. Diameter for the ZnO-Ag was not calculated due to irregular morphology. Comparing the growth of the alloy film to that of the ZnO-Au film indicates including Ag has increased pillar diameter. Moreover, some particles appear in the alloy film, most likely influenced by Ag. Ag tends to have intraplanar diffusion, leading to large particle growth as seen in the ZnO-Ag sample in this work or even leads to tilted pillar growth in other VAN [205]. It is possible to tune the morphology of ZnO-Ag_xAu_{1-x} to make the pillars more uniform in the matrix, similar to ZnO-Au growth. This was achieved by tailoring the growth parameters and performing the deposition under vacuum. The new optimized morphology can be seen in TEM cross-section micrograph in Figure 4.4b, where pillars are more uniformly distributed in matrix.

Moreover, the TEM plan-view image in Figure 4.4c depicts more well-ordered pillar distribution.

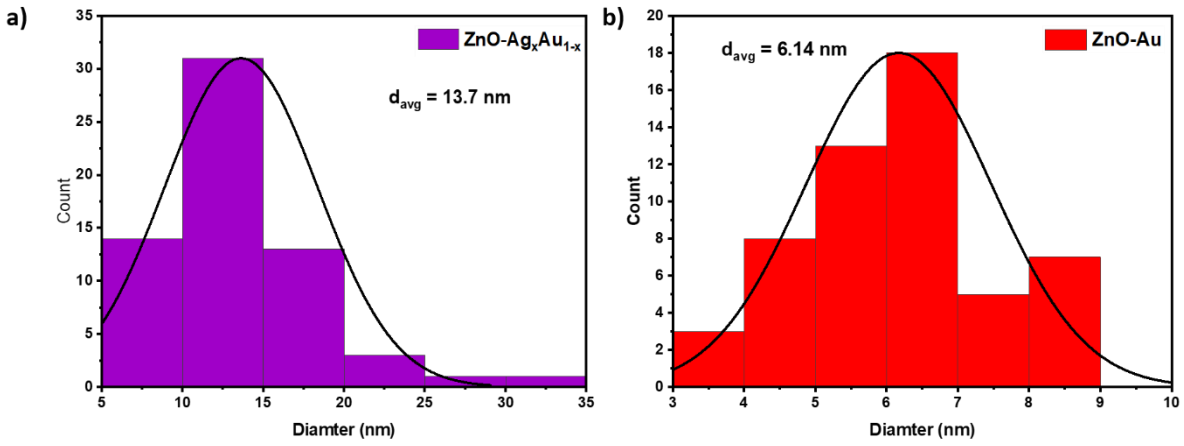

Figure 4.6 Diameter calculation. Calculated average diameter for a) ZnO-$Ag_{61}Au_{39}$ and b) ZnO-Au.

A detailed microstructure characterization study was performed on the ZnO-$Ag_{61}Au_{39}$ VAN and presented in Figure 4.7. Figure 4.7a shows a high-resolution plan-view transmission electron micrograph (HRTEM), indicating the hexagonal shape of nanopillars and the (111) in-plane stacking arrangement. The sides of nanopillars are of {220} planes. Figure 4.7b presents a STEM plan-view image, showing the quasi-hexagonal ordering maintained from the ZnO-Au microstructure. The EDS maps coupled with STEM images, shown in Figure 4.7c-f, depicts the chemical composition of the nanoalloy VAN. Figure 4.7c shows a composite of all measured maps with no overlap between the alloy or ZnO, indicating phase separation between the matrix and nanopillars. Figure 4.7d and f present the EDS map of Ag and Au, respectively. From the plan-view EDS map, the Au and Ag signal appear evenly mixed, indicating no significant phase separation in the nanopillars and that the nanopillars are well alloyed. Figure 4.7m shows a cross-section STEM image with the corresponding EDS elemental mapping shown in Figure 4.7i-l. The maps for Ag and Au appear in Figure 4.7j,l, respectively, and confirm that there is no phase separation and interdiffusion to the matrix in the alloy, as seen in the plan-view EDS maps. Figure 4.7i is a composite of the measured maps, and like the plan-view EDS, indicates no overlap between the nanopillars and the oxide matrix. High-resolution STEM was performed on

the cross-section sample in Figure 4.7n to discern the atomic structure and stacking arrangement. The alloy nanopillars grow with out-of plane [111] direction and have an FCC stacking sequence. The growth direction of nanopillars matches with HCP atomic stacking of ZnO and [0002] out-of plane growth direction.

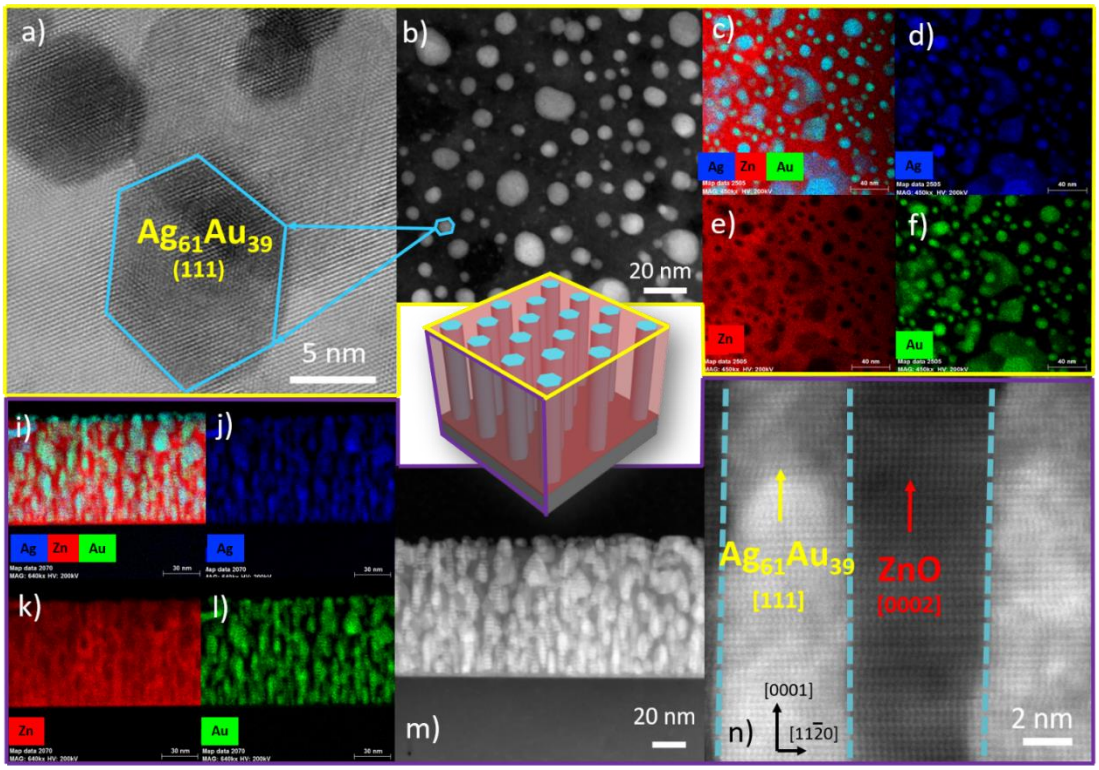

Figure 4.7 Detailed microstructural characterization of ZnO- $Ag_{61}Au_{39}$. At center is model of VAN, the images outlined in yellow and correspond to plan-view and are of a) HRTEM plan-view image of individual nanopillars b) STEM image showing plan-view morphology. EDS chemical mapping is shown in c) combined map, d) Ag map, e) Zn map, f) Au map. Bottom row outlined in purple related to cross-section and eds mapping is shown of i) combined map j) Ag map, k) Zn map, and l) Au map. M) STEM cross-section image showing VAN morphology and n) HRSTEM cross-section showing atomic stacking

The optical properties of ZnO-$Ag_{61}Au_{39}$, ZnO-Ag, and ZnO-Au were compared using UV-Vis spectroscopy as shown in Figure 4.8. Images of the bulk thin films are shown in Figure 4.8a, where ZnO-Ag has a film color of dark-gray and ZnO-Au has red-blue appearance and ZnO-$Ag_{61}Au_{39}$ is a deep-scarlet red color. The physical appearance of plasmonic films depends on different factors including particle size, composition, and density [236]. Bimetallic alloys of Ag_xAu_{1-x} have been predicted to hybridize their plasmonic resonance and produce a deep, scarlet

red color [223], similar to the color observed in the ZnO-$Ag_{61}Au_{39}$ VAN. UV-vis spectroscopy was performed on each film to measure the transmission and plasmonic resonance, the resulting responses are presented in Figure 4.8b. ZnO-Au has a plasmonic resonance at around 565 nm, ZnO-Ag has resonance at 504 nm, and ZnO-$Ag_{61}Au_{39}$ has resonance at 512 nm. The observed SPR of ZnO-Ag_xAu_{1-x} falls within the range predicted of effective medium theory for Ag_xAu_{1-x} nanoalloys [223]. The plasmonic properties coupled with chemical and thermal stability of ZnO makes the ZnO-$Ag_{61}Au_{39}$ VAN a potential candidate for applications in chemical- and bio-sensing [153] and energy harvesting. [152,218]

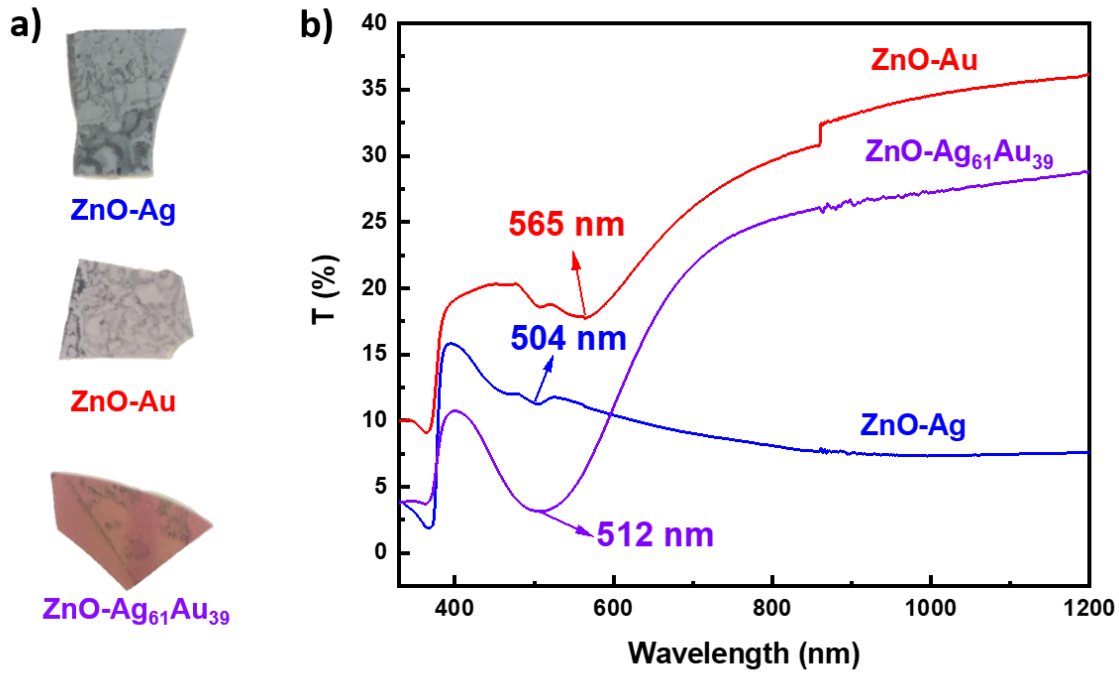

Figure 4.8 Transmission. Images of bulk films presented in a) and in b) the measured transmission from UV-Vis spectroscopy.

The anisotropic microstructure of the oxide-metal VAN can be used to engineer a hyperbolic dispersion [143]. To investigate the anisotropic dielectric function of the ZnO-$Ag_{61}Au_{39}$ VAN, spectroscopic ellipsometry was performed from 210 to 2500 nm to measure the dielectric permittivity as shown in Figure 4.9. The perpendicular and parallel components of permittivity were resolved by using a uniaxial model coupled with B-spline model. The measured

ellipsometry data and fitted models for psi and delta of each film can be found in Figure 4.10. Moreover, the dielectric response of the alloy VAN was compared with ZnO-Ag and ZnO-Au. Experimental setup with respect to the microstructure is inset in Figure 4.9d-f. The real part of ZnO-$Ag_{61}Au_{39}$, ZnO-Ag, and ZnO-Au are plotted in Figure 4.9a-c respectively while the imaginary part are plotted in Figure 4.9d-f, respectively. Hyperbolic regimes are highlighted on the real permittivity graph color-coded to the type of hyperbolic metamaterial, indicating their photonic density of k-states and isofrequency curve. Type I ($\varepsilon_{//} > 0$, $\varepsilon_{\perp} < 0$) hyperbolic regimes are highlighted with yellow and type II ($\varepsilon_{//} < 0$, $\varepsilon_{\perp} > 0$) hyperbolic regime are highlighted green. The isofrequency curve of type I hyperbolic metamaterial can described as a hyperboloid of two sheets, indicating support of high and low k-states. The isofrequency curve of type II hyperbolic metamaterial can be described as a paraboloid of one-sheet and supports only high k-states [179]. To confirm the surface plasmon resonance calculated from the UV-Vis transmission spectra, angular reflectivity measurements were also performed on the ellipsometer and presented in Figure 4.11 at angles of 40°, 50°, 60°, and 70°. To confirm the validity of the model used to derive the complex dielectric function, the same uniaxial b-spline model was fitted to the measured angular reflectivity. The measured reflectivity demonstrated SPR at 520 nm for ZnO-Ag at 520 nm for ZnO-$Ag_{61}Au_{39}$, 500 nm for ZnO-Ag, and 610 nm for ZnO-Au. Simulated reflectivity models demonstrated SPR within ~20nm, confirming a good agreement between the simulation and measurement.

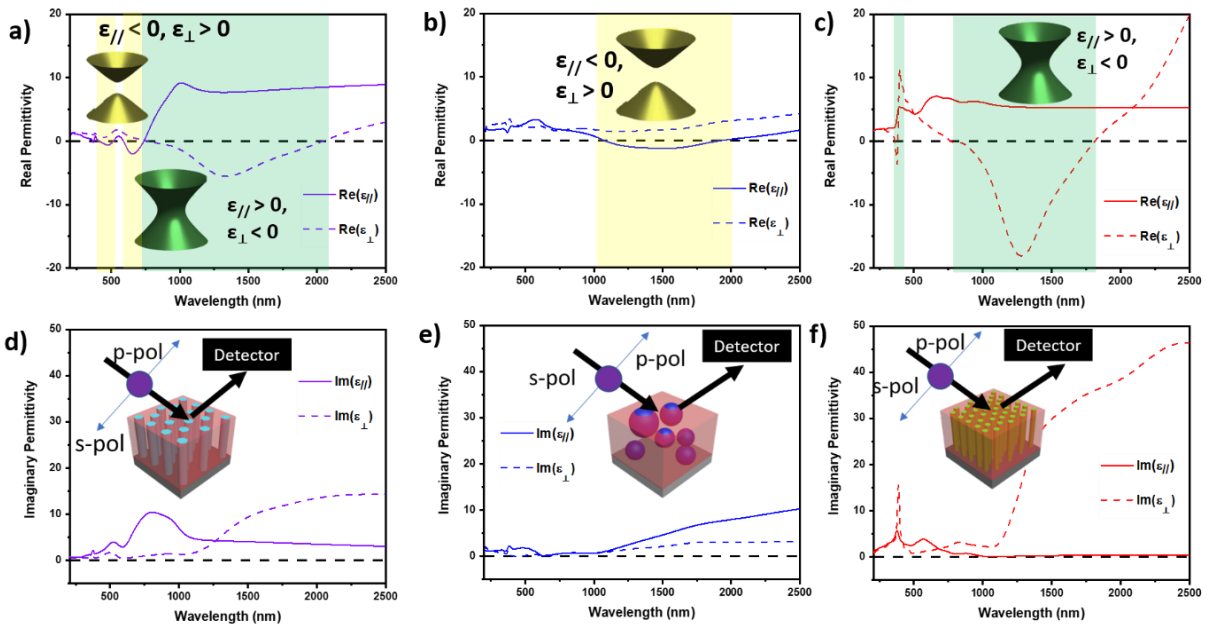

Figure 4.9 Dielectric function. Real part of permittivity for a) ZnO-Ag_xAu_{1-x} , b) ZnO-Ag, and c) ZnO-Au Imaginary permittivity for part of permittivity for d) ZnO- $Ag_{61}Au_{39}$, e) ZnO-Ag, and f) ZnO-Au. Inset in a-c) are representative isofrequency curve for type I hyperbolic metamaterial (yellow regime) and type II hyperbolic metamaterial (green regime). Inset in d-c) are experimental setup for ellipsometry measurement for respective nanocomposite thin film.

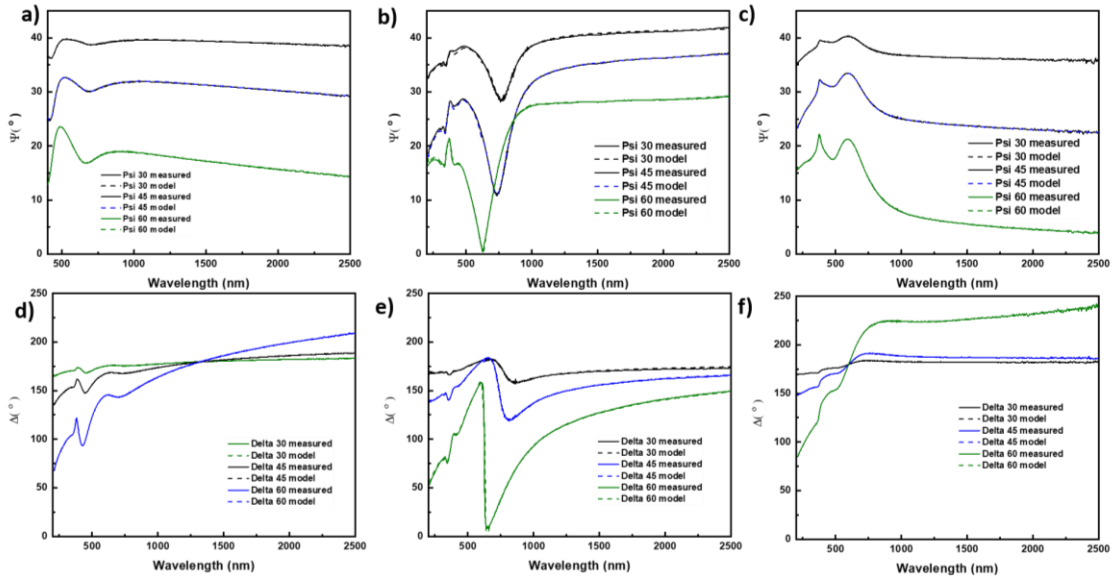

Figure 4.10 Experimental data and model fitting for measured Ψ and Δ. Top row shows Ψ for a) ZnO-Au, b) ZnO-Ag, and c) ZnO-$Ag_{61}Au_{39}$. Bottom row shows Δ for d) ZnO-Au, e) ZnO-Ag, and f) ZnO-$Ag_{61}Au_{39}$.

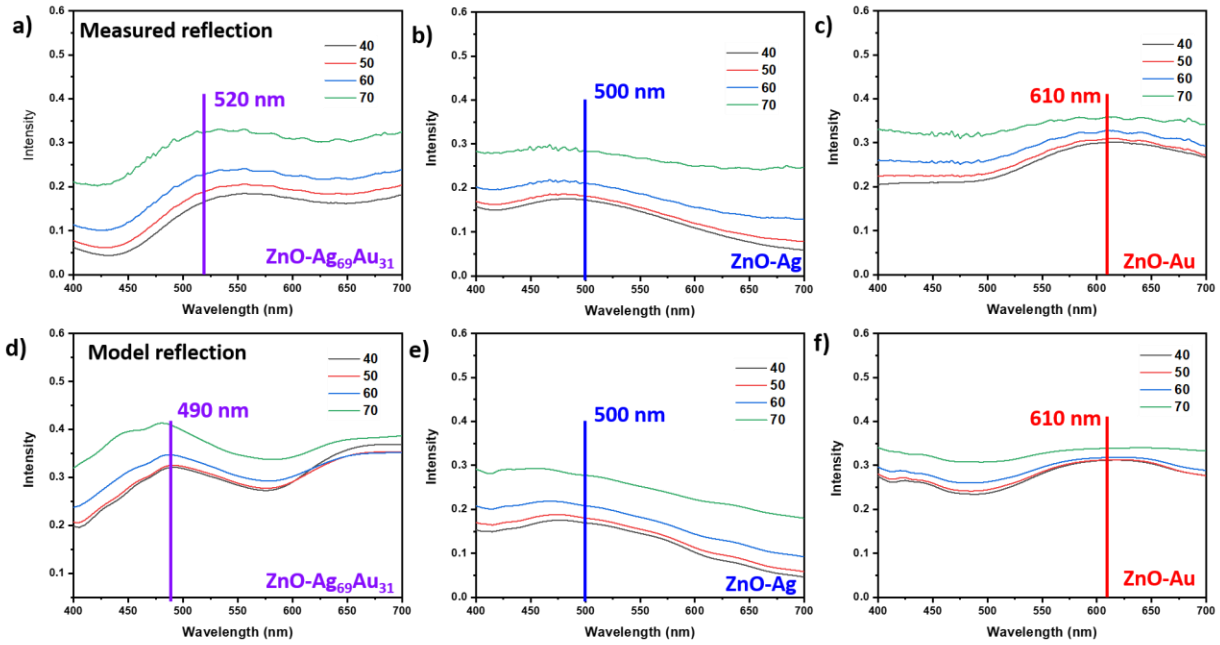

Figure 4.11 Measured and model angular reflectivity for 40°, 50°, 60°, and 70°. Measured reflection for a) ZnO-$Ag_{61}Au_{39}$, b) ZnO-Ag, and c) ZnO-Au. Model reflectivity determined from uniaxial b-spline model for d) ZnO-$Ag_{61}Au_{39}$, e) ZnO-Ag, and f) ZnO-Au.

The real and imaginary part of dielectric permittivity of ZnO-$Ag_{61}Au_{39}$ VAN are plotted in Figure 4.9a and Figure 4.9d, respectively. ZnO-Ag real and imaginary permittivity are depicted in Figure 4.9b,e, respectively, while the data of ZnO-Au are presented in Figure 4.9c,f, respectively. Anisotropy of the VAN microstructure is obvious when comparing $\varepsilon_{//}$ and $\varepsilon_{\perp}$ components for ZnO-Au and ZnO-$Ag_{61}Au_{39}$. The more isotropic particle-in matrix microstructure of ZnO-Ag is evident in $\varepsilon_{//}$ and $\varepsilon_{\perp}$ components having similar plot, minor differences due to irregular particle shape as seen in plan-view in Figure 4.9d. ZnO-$Ag_{61}Au_{39}$ out-of plane ($\varepsilon_{\perp}$) component has epsilon-near zero permittivity at 736 nm and 2060 nm, while the in-plane ($\varepsilon_{//}$) component has epsilon-near zero permittivity at 400 nm, 520 nm, 590 nm, and 736 nm. Moreover, ZnO-$Ag_{61}Au_{39}$ hybrid material demonstrates three hyperbolic regime, type 1 hyperbolic regimes occur from 400-520 nm and 590-736 nm and a type II hyperbolic region occurs from 736-2050 nm. Interestingly, ZnO-Ag has hyperbolic regime ranging from 1000 – 2100 nm with ENZ permittivity occurring at 1000 and 2100 nm. ZnO-Au has hyperbolic regime from 362-382 nm and 758-1820 nm with ENZ permittivity occurring at 362 nm, 382 nm, 758

nm, and 1820 nm in $\varepsilon_{\perp}$ component. Both ZnO-Ag and ZnO-Au have similar hyperbolic regime in the near-infrared occurring from 1000-2100 nm for ZnO-Ag and 758-1820 nm for ZnO-Au, but ZnO-Ag is a type I hyperbolic metamaterial while ZnO-Au is a type II hyperbolic metamaterial. ZnO-$Ag_{61}Au_{39}$ has inherited the hyperbolic properties of ZnO-Au in this regime and has a type II hyperbolic regime from 736-2050 nm. ZnO-Au demonstrates high absorption losses in its near-infrared hyperbolic regime (758-1820 nm), depicted in Figure 5e. This contrast with imaginary permittivity of ZnO-Ag in Figure 4.9f, which has overall much lower values in the near-infrared hyperbolic regime. By alloying Ag and Au, ZnO-$Ag_{61}Au_{39}$ VAN has maintained similar hyperbolic regimes in near-infrared as ZnO-Au and has much lower values of imaginary permittivity as seen in Figure 4.9f. While ZnO-Ag does demonstrate hyperbolic regime in the near-infrared, it does not have visible regime hyperbolic regions. Alloying in the ZnO-$Ag_{61}Au_{39}$ hybrid material has improved and rectified the shortcomings of both ZnO-Au and ZnO-Ag nanocomposite. ZnO-$Ag_{61}Au_{39}$ has lower absorption losses than ZnO-Au and demonstrates hyperbolicity in the visible regime, where ZnO-Ag is lacking. All of this coupled together indicates that alloying is an effective approach for tuning optical functionality. Moreover, the ZnO-$Ag_{61}Au_{39}$ VAN has demonstrated more significant hyperbolic dispersion and ENZ permittivity across a broad range of wavelength with low associated imaginary permittivity as compared with other Ag/Au nanowire hyperbolic metamaterial in the both the near-infrared and visible regimes [139,140,143,179,188,214,237,238]. Through the unique one-step self-assembly alloy approach in this report, it is possible to grow pillar-in matrix ZnO-Ag type hyperbolic metamaterials, where ZnO-Ag usually prefers particle-in matrix morphology due to complex growth conditions. Furthermore, this approach allows for thin film integration across various substrates and surfaces, broadly expanding the application of HMM and nanoalloys.

Oxide-alloyed metal-based VANs open an entire new paradigm of multifunctionality, as it combines the field of nanoalloys with the VAN platform. The ZnO-$Ag_{61}Au_{39}$ film demonstrated a broad range of hyperbolic properties and SPR when compared with other Ag/Au nanowire arrays. Therefore, the ZnO-$Ag_{61}Au_{39}$ VAN is envisioned as an ideal candidate for multifunctional applications in both the fields of hyperbolic metamaterials and plasmonics, specifically in the application of sub-diffraction imaging and far-field hyperlenses [179,217]. The optical losses and properties in this work could be further engineered by varying the alloy composition and incorporating other metals in alloy form, such as the inclusion of other low-loss

metals like Cu or Al. As seen in Figure 4.12, it is possible to achieve ZnO-Au_xCu_{1-x} with nanopillar morphology e from cross-section STEM images with well-ordered in-plane structure. The investigation on the effect of Cu alloying with Au in ZnO dielectric matrix on optical properties is currently ongoing. Further improvements could be achieved by alloying with other optically interesting metals and exotic functionalities could be realized through magnetic alloy compositions with Fe, Co, and Ni.

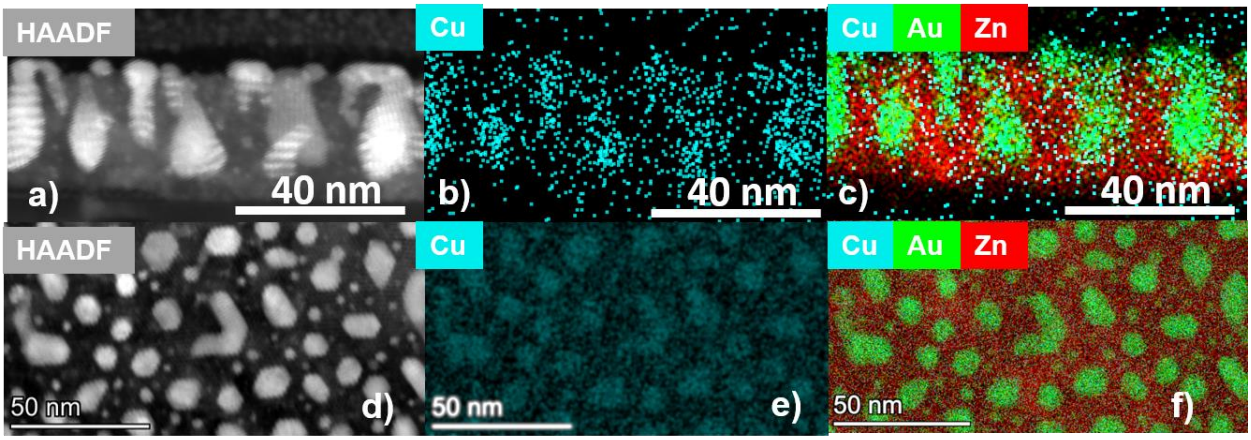

Figure 4.12-ZnO-Au_xCu_{1-x}. a) Cross-section STEM image of ZnO-Au_xCu_{1-x}, b) cross-section EDS-map of Cu c) Cross-section combined EDS map of Cu, Au, and Zn. d) STEM plan-view of ZnO-Au_xCu_{1-x}, b) plan-view EDS map of Cu alloyed nanopillars, c) combined EDS plan-view map of Cu, Au, Zn.

4.5 Conclusions

In this work, a new oxide-metallic alloy-based VAN consisting of ZnO and $Ag_{61}Au_{39}$ alloy nanopillars was presented. ZnO-$Ag_{61}Au_{39}$ was deposited through a one-step pulsed laser deposition method and compared with that of single-case ZnO-Ag and ZnO-Au nanocomposite. Microstructural characterization shows that the new alloyed VAN inherits the epitaxy and anisotropy of the ZnO-Au VAN. Spectroscopic ellipsometry was performed to investigate the anisotropic dielectric response of ZnO-$Ag_{61}Au_{39}$ and compared to ZnO-Au and ZnO-AgThe alloy VAN has demonstrated interesting hyperbolic dispersion and ENZ permittivity as compared with anisotropic ZnO-Au and other Ag/Au nanowire array hyperbolic metamaterials. UV-vis spectroscopy measurements discerned the plasmon response of all films. Angular reflectivity measurements were conducted to confirm the plasmon resonance compare the plasmonic response of the alloy VAN and compared to ZnO-Ag and ZnO-Au. From

measurements, the ZnO-$Ag_{61}Au_{39}$ alloy film possessed broad optical properties for metamaterial application, indicating the potential of nanoalloys in the field of nanophotonics to produce multifunctional hybrid plasmonic metamaterials and opening a new route for property tuning in the oxide-metal hybrid materials. Future work will include the investigation and systematic study of new alloy-based nanocomposites including optical ZnO-Au_xCu_{1-x}, magneto-optical ZnO-Ni_xCu_{1-x}, and magnetic ZnO-Co_xNi_{1-x}. Systematic growth parameter studies and the resulting effect on morphology and properties will be discerned.

5. DEPOSITION PRESSURE-INDUCED MICROSTRUCTURE CONTROL AND PLASMONIC PROPERTY TUNING IN HYBRID ZNO-AG_XAU_{1-X} THIN FILMS

Reproduced from R. L. Paldi, X. Sun, X. L. Phuah, J. Lu, X. Zhang, A. Siddiqui, and H. Wang, " Deposition pressure-induced microstructure control and plasmonic property tuning in hybrid ZnO–Ag x Au 1−x thin films ," Nanoscale Adv. 3, 2870–2878 (2021) DOI: 10.1039/D0NA00887G with permission from the Royal Society of Chemistry.

5.1 Overview

Self-assembled oxide-metallic alloyed nanopillars as hybrid plasmonic metamaterials (e.g., ZnO-Ag_xAu_{1-x}) in a thin film form are grown using a pulsed laser deposition method. The hybrid films were demonstrated to be highly tunable via systematic tuning of the oxygen background pressure during deposition. The pressure effects on morphology and optical properties have been investigated and found to be critical to the overall properties of the hybrid films. Specifically, low background pressure results in the vertically aligned nanocomposite (VAN) form while the high-pressure results in more lateral growth of the nanoalloys. Strong surface plasmon resonance was observed in the UV-Vis regime and a hyperbolic dielectric function is resulted due to the anisotropic morphology. The oxide-nanoalloy hybrid material grown in this report presents a highly effective approach for tuning binary nanoalloy morphology and properties through systematic parametric changes, important for their potential applications in integrated photonics and plasmonics such as sensors, energy harvesting, and beyond.

5.2 Introduction

Bimetallic nanoalloys are a class of materials poised to present promising applications in nanotechnology [229,230,233,239]**.** For example, Ag_xAu_{1-x} [240] and Au_xCu_{1-x} [241] are capable of use for optical and plasmonic applications, where the plasmon resonance is easily controlled through manipulation of the composition and morphology. Other promising nanoalloys are magnetic compositions such as Fe_xCo_{1-x} [242] for magnetic storage memory, where properties can be tuned by composition and morphology [243]. Furthermore, plasmonic and magnetic coupled nanoalloys can be created such as Au_xFe_{1-x} [160] and Co_xPt_{1-x} [244] for interesting

magneto-optic coupling. Currently, most nanoalloys are grown through chemical synthesis methods which can produce effective nanoalloys. However, the nanoalloys grown through these methods suffer from stability issues including dealloying and phase segregation [233,245]. Another major issue plaguing nanoalloys is the inability to easily tune size, morphology, composition and properties [229,230]. To overcome the stability issues, multicomponent nanoalloys can be created but they also eventually succumb to dealloying [246]. Another way is to create nanocomposites that encapsulate the nanoalloy in a more chemically stable nanocomposite form [227].

Oxide-based nanocomposites present a promising platform for increasing long-term stability [100]. Oxides are typically chemically stable and have a wide range of functional properties like ferromagnetism in lanthanum strontium manganite (LSMO) or ferroelectricity in barium titanate (BTO). Combining different nanoalloys with different oxides could provide a pathway for achieving new, multifunctional hybrid materials with enhanced properties and stability. Growing these hybrid oxide-nanoalloy materials could be achieved through a pulsed laser deposition technique. The PLD technique is a highly versatile physical vapor deposition method that has demonstrated a bottom-up, one-step method of growth for self-assembled oxide-metal hybrid materials such as BZO-Co, BTO-Au, ZnO-Au, and recently the oxide-nanoalloy composites [143,145,207,208,221,247,248]. The PLD technique has already been used to achieve stability in oxide-metal and nitride-metal hybrid materials [108,144,249]**.** The critical issue to overcome for the oxide-nanoalloy system is achieving a sufficiently mixed alloy without segregation.

In this work, zinc oxide (ZnO) matrix support has been combined with the Ag_xAu_{1-x} nanoalloy to form an oxide-nanoalloy hybrid plasmonic material of ZnO-Ag_xAu_{1-x}. The tunability of the oxide-nanoalloy ZnO-Ag_xAu_{1-x} hybrid material was investigated through manipulation of the oxygen background pressure during pulsed laser deposition. ZnO was selected as the matrix as it is a well-known wide-band gap semiconductor (E_g ~ 3.37 eV) that is useful for photocatalysis and transparent electrodes materials [250–252]. Furthermore, ZnO is chemically and thermally stable, earth abundant, and generally non-toxic, making it a promising candidate to form stable nanoalloy nanocomposites. Ag_xAu_{1-x} is chosen as the nanoalloy in this report due to being extensively studied for its plasmonic resonance and usefulness in energy and sensor applications [230,253]. Varying the oxygen background pressure provides a successful

method for tailoring optical properties and morphology of the ZnO-Ag_xAu_{1-x} nanocomposite. A highly tunable morphology can be achieved by systematic variation in background pressure per the schematic presented in Figure 5.1. As the background pressure varies from low pressure (vacuum and 20 mTorr) to high pressure (100 and 150 mTorr), the oxide-nanoalloy morphology could be effectively tuned. A systematic microstructural characterization of ZnO-Ag_xAu_{1-x} hybrid thin films was performed through XRD, STEM, EDS-mapping and the corresponding effect on optical properties was investigated through Spectroscopic Ellipsometry and UV-Vis Spectroscopy.

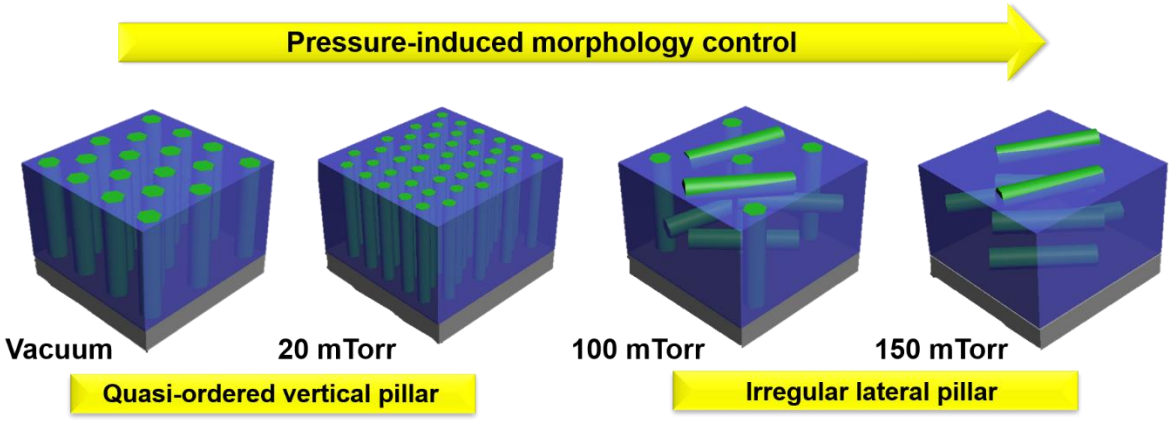

Figure 5.1 Schematic diagram of oxygen pressure microstructure tuning in ZnO- Ag_xAu_{1-x} nanocomposite. In the diagram, ZnO matrix is colored blue while Ag_xAu_{1-x} nanoalloy is colored green. Deposition in low pressure produces vertically aligned alloyed nanopillars, while increasing oxygen pressure induces irregular lateral growth.

5.3 Experimental

5.3.1 Thin film growth

ZnO-Ag_xAu_{1-x} nanocomposite films were grown on c-cut Al_2O_3 (0001) using pulsed laser deposition. Growth was performed with a KrF excimer laser (Lambda Physik Complex Pro 205, $\lambda = 248$ nm) and substrate temperature was kept constant at 500°C. The laser energy was 420 mJ focused at an incident angle of 45°. The target-substrate distance was kept constant at 4.5 cm and measured before each deposition to ensure accuracy. A composite target consisting of ZnO-Ag_xAu_{1-x} were developed through solid-state sintering used for laser ablation. Before deposition, the chamber was pumped down to around 10^{-6} mTorr before an oxygen pressure was inflowed. Oxygen background pressure was varied from vacuum to 150 mTorr and laser pulse frequency

was set to 5 Hz for all deposition After all depositions, the chamber was cooled to room temperature at a rate of 15 ^{o}C/min.

5.3.2 Microstructure characterization

Film morphology was characterized through XRD, TEM, and STEM coupled with EDS-mapping. XRD scans of θ-2θ were conducted using a Panalytical X'Pert X-ray diffractometer wit Cu K_{α} radiation. Bright field TEM, STEM, SAED patterns and EDS-mapping was performed in a FEI Talos F200X TEM. Samples for electron microscopy were prepared, for both cross-section and plan-view, via a standard grinding procedure which entails manual grinding, polishing, dimpling, and a final ion milling step to achieve electron transparency. (PIPS 691 precision ion polishing system, 5 KeV for cross-section and 4-4.5 KeV for plan-view sample)

5.3.3 Optical measurements

Ellipsometry experiments were carried out on an RC2 Spectroscopic ellipsometer (J.A. Woollam Company). Three angles 30^{o}, 45^{o}, and 60^{o} were measured from a spectrum range of 210 – 2500 nm. Measured values of psi and delta data were obtained and then fit with a uniaxial model coupled with B-spline model to discern anisotropic dielectric function of ZnO-Ag_xAu_{1-x} nanocomposite thin films, an agreeable mean square error (MSE) < 5 was obtained for all film models. Normal incident depolarized transmittance (T%) was measured using an optical spectrophotometer (Lambda 1050 UV-Vis spectrophotometer).

5.4 Results and Discussion

X-ray diffraction analysis was performed to elucidate the effect of oxygen background pressure on morphology of ZnO-Ag_xAu_{1-x} nanocomposites. The results are summarized in Figure 5.2. Scans of θ-2θ are depicted in Figure 5.2a for all films deposited at different background pressures, indicating the high degree of epitaxial quality for all the films. ZnO matrix grew in hexagonal wurtzite structure with preferred out-of-plane c-axis orientation along (0002) direction, parallel with underlying c-axis Al_2O_3 substrate (0006) plane. Both Ag and Au have a face-centered cubic (FCC) structure, and their alloys also form an FCC lattice [254]. Therefore, based on measured θ-2θ, the alloyed nanopillars were determined to have face-centered cubic (FCC)

structure with out-of-plane aligned with (111) direction and parallel to (0006) plane of substrate. To match both hexagonal-shape of wurtzite ZnO and c-axis orientated Al_2O_3 substrate, the alloyed lattice rotates so that out-of-plane direction has hexagonal shape. This created an out-of-plane alignment of Ag_xAu_{1-x} (*lll*) || ZnO (000*l*) || Al_2O_3 (000*l*).

To determine if there was peak splitting in the alloy, which could imply phase separation, high-resolution θ-2θ scans were performed across a small range near the (111) peak of Ag_xAu_{1-x}, depicted in Figure 5.2b. There is no obvious peak splitting, which implies that the nanoalloy grown in this work is well mixed for all samples. Interestingly, there are variations of peak position and d-spacing with respect to background pressure tuning. In Figure 5.2b, the value for location of bulk Ag ($2\theta_{111}$ = 38.116°) and bulk Au ($2\theta_{111}$ = 38.252°) peak is denoted. For the nanoalloy deposited under vacuum, the peak was located near bulk Ag, with $2\theta_{111}$ = 38.11°. As the background pressure was increased to 20 mTorr, the peak was shifted downward to below bulk Ag with $2\theta_{111}$ = 38.08°. As the pressure was further increased to 100 mTorr and 150 mTorr, the peak shifted upward from $2\theta_{111}$ = 38.2° and to $2\theta_{111}$ = 38.23°. Interestingly, as the pressure was increased, the peak location shifted from near the Ag peak at low pressure toward the Au peak at high pressure. The relationship for tuning of the alloy lattice was more clearly demonstrated when investigating the d-spacing in Figure 5.2d. For the films deposited under vacuum, the alloy d-spacing d_{111} is measured to be 0.2359 nm, which is the same as the bulk Ag d-spacing (d_{111} = 0.2359 nm). When background pressure increases to 150 mTorr, the alloy d-spacing d_{111} is measured to be 0.2352 nm, which is more comparable to bulk Au d-spacing (d_{111} = 0.2351 nm). When background pressure increases, compressive stress on the alloy lattice increases, as d-spacing was tuned smaller from vacuum at d_{111} = 0.2359 nm to d_{111} = 0.2352 nm in the 150 mTorr ambient. The ZnO (0002) peak was also investigated to determine pressure variation, with high-resolution scans of (0002) peak shown in Figure 5.2c. There appeared to be some peak shifting with respect to background pressure, but no specific trend. This was further confirmed based on d-spacing of ZnO (0002) peak in Figure 5.2d, which appeared to be no trend and little to no change in the ZnO lattice. This is contrary to the usual relationship between ZnO and oxygen background pressure in PLD growths [50,250,255–258]. The lack of general trend for the ZnO may be related to the nanoalloy formation driving the lattice strain in the nanocomposite.

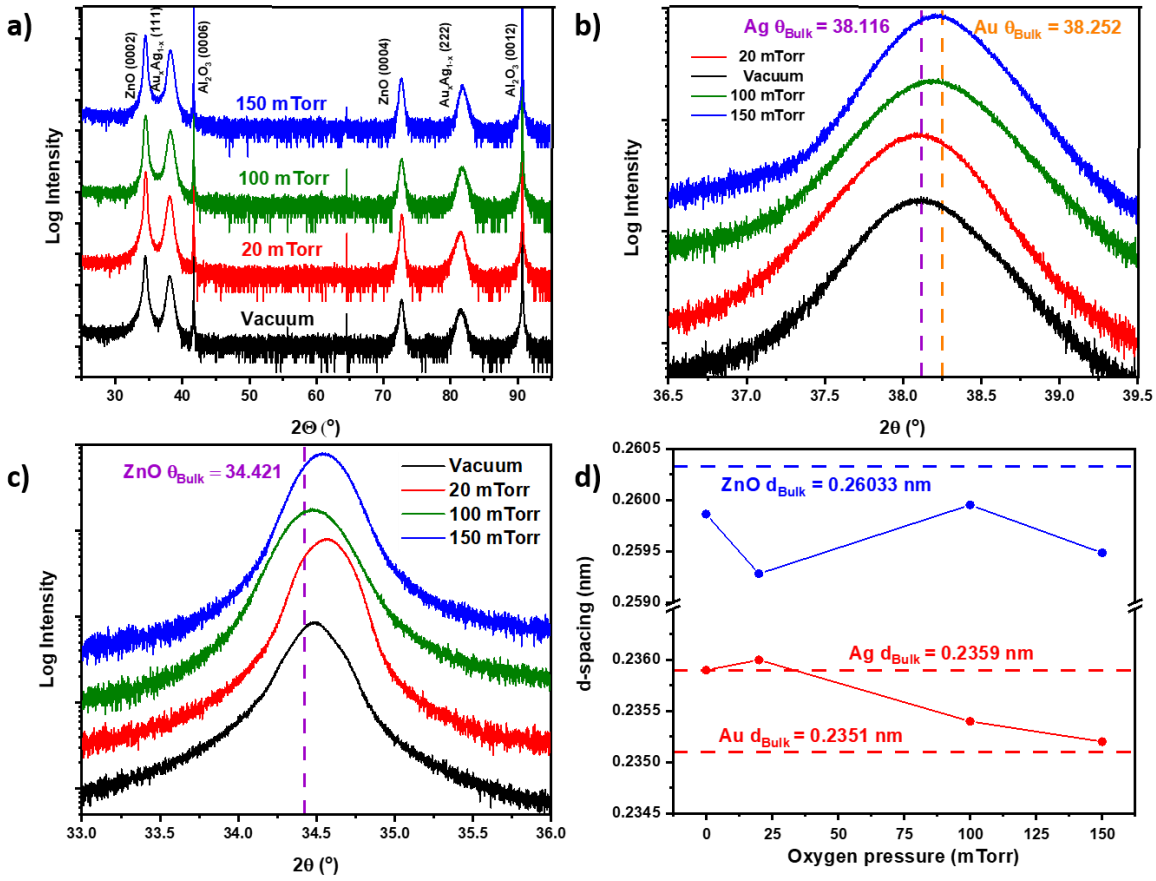

Figure 5.2 X-ray diffraction. A) Scans of θ-2θ for all films deposited at different oxygen pressure, b) scans in the region of Ag/Au (111) peak, c) scans showing region near ZnO (0002) peak, and d) d-spacing calculation for Ag_xAu_{1-x} (111) and ZnO (0002).

The composition of each nanoalloy was calculated from EDS-spectrum and plotted as a ratio between Ag/Au vs. background pressure in Figure 5.3a - Ag/Au > 1 implies Ag-rich alloys and Ag/Au < 1 implies Au-rich alloys. The resulted compositions from EDS-spectra were tabulated in Figure 5.3b-e and the Ag/Au vs. deposition pressure graph in Figure 5.3a was calculated using the wt% values from the tables in Figure 5.3b-e. The x-value for each nanoalloy composition was also calculated for each oxygen pressure deposition. Composition of the nanoalloys were $Ag_{33}Au_{67}$, $Ag_{61}Au_{39}$, $Ag_{55}Au_{45}$, and $Ag_{67}Au_{33}$ for deposition at vacuum, 20 mTorr, 100 mTorr, and 150 mTorr, respectively. Results of the composition tuning, and EDS shows an overall trend of Ag content increasing with respect to increasing background pressure but there was a decrease in Ag content between 20 mTorr and 100 mTorr. The increase of Ag

content in the film and decrease of Au could be related to the mass of Au and Ag. Ag is a lighter species than Au so it will have higher kinetic energy on initial ablation. Au will have less kinetic energy than Ag and therefore as the pressure is increased, Au species will either be knocked out of the arriving plume due to the reduced plume size or they will not have enough kinetic energy to diffuse into the film.

a)

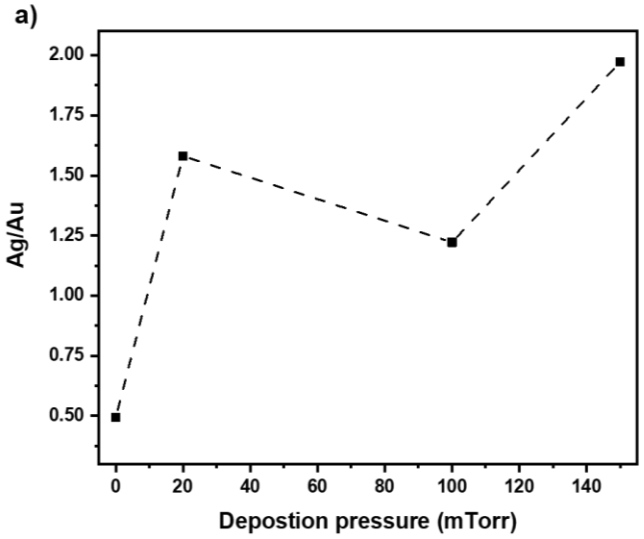

b)

Element	series	Net	[wt.%]	[norm. wt.%]	[norm. at.%]	Error in wt.% (3 Sigma)
Silver	K-series	8	26.00447	26.00447	28.84612	32.00971
Gold	L-series	112	52.56009	52.56009	31.92977	25.43802
Zinc	K-series	79	21.43544	21.43544	39.22411	8.10837
		Sum:	100	100	100	

c)

Element	series	Net	[wt.%]	[norm. wt.%]	[norm. at.%]	Error in wt.% (3 Sigma)
Silver	K-series	42	47.10525	47.10525	46.39546	24.33502
Gold	L-series	204	29.79326	29.79326	16.07032	12.29608
Zinc	K-series	271	23.10149	23.10149	37.53423	5.042388
		Sum:	100	100	100	

d)

Element	series	Net	[wt.%]	[norm. wt.%]	[norm. at.%]	Error in wt.% (3 Sigma)
Gold	L-series	91	34.17448	34.17448	18.68453	17.71614
Zinc	K-series	110	24.05267	24.05267	39.61181	7.788252
Silver	K-series	14	41.77285	41.77285	41.70366	36.44618
		Sum:	100	100	100	

e)

Element	series	Net	[wt.%]	[norm. wt.%]	[norm. at.%]	Error in wt.% (3 Sigma)
Gold	L-series	192	26.0194	26.0194	13.84054	10.90774
Silver	K-series	49	51.3143	51.3143	49.84183	24.5564
Zinc	K-series	287	22.6663	22.6663	36.31763	4.842717
		Sum:	100	100	100	

Figure 5.3 Ag/Au ratio for ZnO-Ag_xAu_{1-x} calculated from EDS-spectra. Table showing composition from EDS-map for b) vacuum, c) 20 mTorr, d) 100 mTorr, e) 150 mTorr.

For a more detailed microstructural characterization, the ZnO-$Ag_{33}Au_{67}$ vertically-aligned nanocomposite (VAN) deposited in vacuum was selected for a microscopy analysis. The full characterization results using STEM coupled with EDS-mapping and TEM are depicted in Figure 5.4. A model of the structure can be seen in Figure 5.4a of the VAN. A STEM image of the cross-section sample is shown in Figure 5.4b. HR-STEM was performed in Figure 5.4c to determine the atomic arrangement of $Ag_{33}Au_{67}$ and ZnO. The blue-dashed line indicates heterointerface between the ZnO matrix and nanopillars. The out-of-plane atomic arrangement of $Ag_{33}Au_{67}$ grows with the out-of-plane direction [111] and ZnO grows with out-of-plane direction [0002], confirming the orientation from XRD in Figure 5.2. STEM coupled with EDS-mapping was performed on the cross-section image in Figure 5.4d-g. The map for Au can be seen in Figure 5.4d and Ag is in Figure 5.4e. Mapping for Ag and Au only occurred from the nanopillar and mapping for Zn only occurred in matrix, indicating the well separated nanopillar and matrix

phases. A STEM image of plan-view is shown in Figure 5.4h, depicting hexagonal shape of alloyed nanopillars and quasi-hexagonal in-plane ordering. Plan-view EDS-mapping was performed in Figure 5.4j-m to confirm the well-separated phases of Ag_xAu_{1-x} pillars and the ZnO matrix, evidenced by the Ag, Au and Zn maps and the combined EDS-map in Figure 5.4l. A HR-TEM plan-view image in Figure 5.4m shows the in-plane atomic arrangement of nanopillars and the matrix. The (111) stacking arrangement of the alloy pillars can be seen and wurtzite structure of matrix, the sides of the nanoalloy nanopillars are indexed as {220} planes. The out-of plane epitaxial relationship is determined from the cross-section SAED pattern in Figure 5.5 as $Ag_{33}Au_{67}$ (220) || ZnO (10-10) || Al_2O_3 (11-20); the in-plane epitaxial relationship was determined as $Ag_{33}Au_{67}$ (20-2) || ZnO (11-20) || Al_2O_3 (01-10). Moreover, the in-plane diffraction pattern of the alloy demonstrated interesting double-diffraction in the SAED pattern relating to the alloy formation.

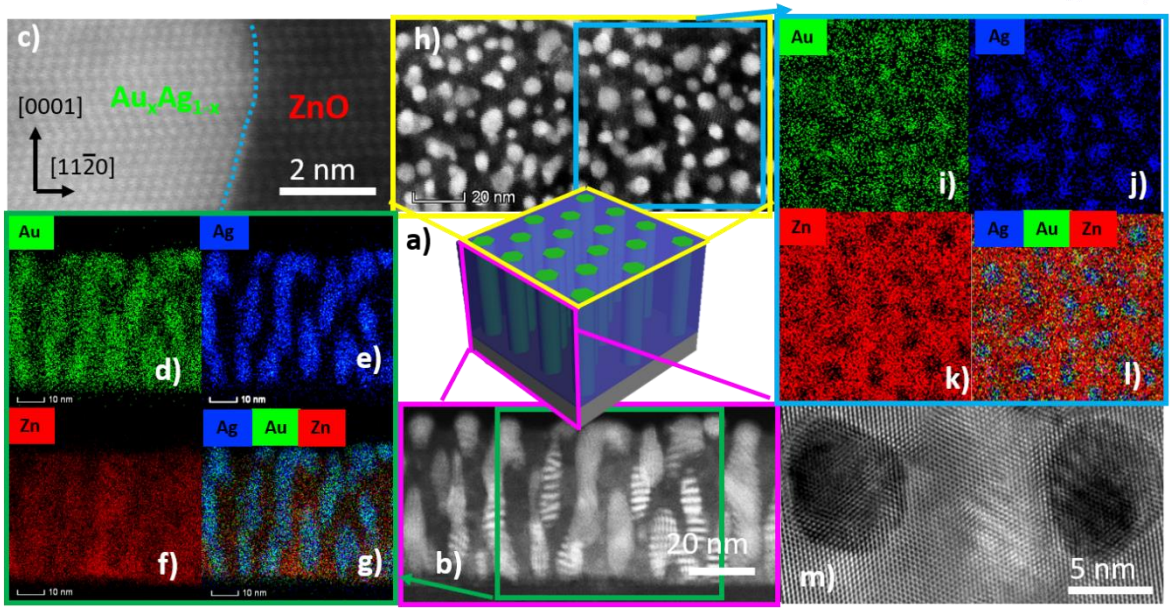

Figure 5.4 Microstructure characterization of vacuum deposition sample. A) schematic diagram of microstructure, b) representative cross-section STEM micrograph, c) HRSTEM micrograph at heterointerface of alloy/oxide. EDS-chemical map of d) Au, e) Ag, f) Zn, g) combined. H) representative plan-view micrograph. EDS-mapping of i) Au, j) Zn, k) combined. m) HRTEM of plan-view stacking arrangement.

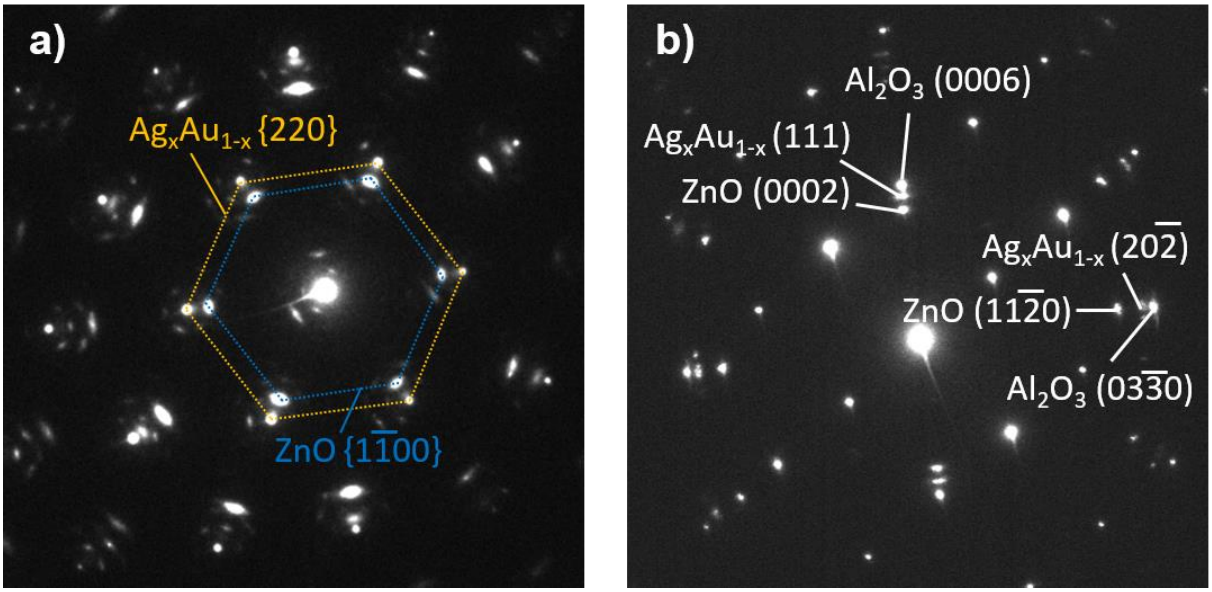

Figure 5.5 Selective area electron diffraction (SAED) pattern for a) plan-view and b) cross-section.

The effect of oxygen background pressure on the morphology of ZnO-Ag_xAu_{1-x} nanocomposites was investigated through scanning transmission electron microscopy (STEM) analysis of both cross-section and plan-view samples for all films for comparison in Figure 5.6. STEM under high angle annular dark field mode (HAADF) was chosen as it provides excellent composition related contrast due to Z-contrast imaging (i.e., contrast ~$Z^{1.7}$). Furthermore, cross-section EDS-mapping was also performed on the other nanoalloy samples deposited at different background pressure and presented in Figure 5.7. The EDS-map for each film shows that the nanoalloy remained sufficiently mixed despite systematic increases in background deposition pressure. Moreover, the nanoalloy and the oxide matrix remained a distinctly two-phase nanocomposite material. The cross-section STEM image of the film deposited under vacuum is shown in Figure 5.6a. The morphology was comprised of vertically aligned alloyed nanopillars embedded in ZnO matrix. The plan-view STEM image for vacuum is shown in Figure 5.6e, and indicated that alloyed nanopillars have hexagonal shape, which followed from the XRD of the alloy having out-of-plane (111) direction. Interestingly, as background pressure was increased to 20 mTorr in Figure 5.6b, the pillars remained vertically aligned but are higher density and some particles become interspersed in the matrix. The plan-view of 20 mTorr film in Figure 5.6f indicated nanopillars retained hexagonal shape and confirmed the increase in small particles

when compared to the film grown at vacuum in Figure 5.6e. When background pressure was increased to 100 mTorr in Figure 5.6c, the morphology became more irregular and included a combination of vertical and lateral growth. It suggests that morphology tuning could be caused by the increased background pressure reducing the kinetic energy and results in plasma plume cluster nucleation as reported previously [32]. In the plan-view image shown in Figure 5.6g, the 100 mTorr growth retained some hexagonal morphology of nanopillars and increased in size. Background pressure was further increased to 150 mTorr in Figure 5.6d, where the morphology became more regular and lateral. This is confirmed in Figure 5.6h, where the growth is depicted as irregularly shaped lateral nanopillars. As background pressure was increased, the ordering of the nanopillars appears to become more irregular within the matrix. At elevated pressure, there is a reduction in kinetic energy and consequently, irregular nanopillar growths. Moreover, as the background pressure is increased, cluster nucleation begins to occur in the plasma plume [33,39,46,47]. This cluster nucleation and reduction in kinetic energy could be accounted for the transition from vertical pillars at low pressure to lateral pillars under high pressure. The reduction in kinetic energy inhibits the ability for ordered and vertically-aligned pillar formation. Moreover, the reduction in kinetic energy in the plasma plume causes the ejection of heavier elements like Au, which could explain the observed composition tuning in Figure 5.3 such that Ag content increases in the nanoalloy as pressure is increased.

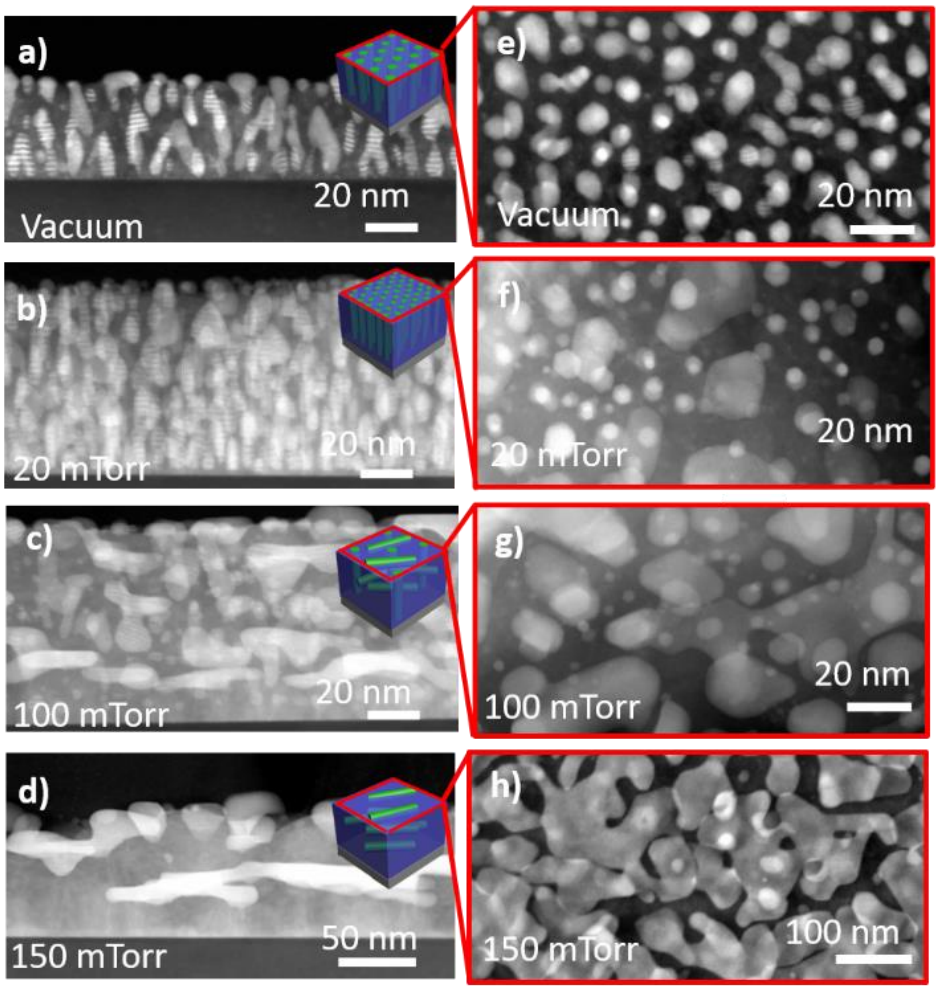

Figure 5.6 Morphology tuning through oxygen pressure. Cross-section STEM image for a) vacuum, b) 20 mTorr, c) 100 mTorr, and d) 150 mTorr. Corresponding plan-view image for e) vacuum, f) 20 mTorr, g) 100 mTorr, and h) 150 mTorr.

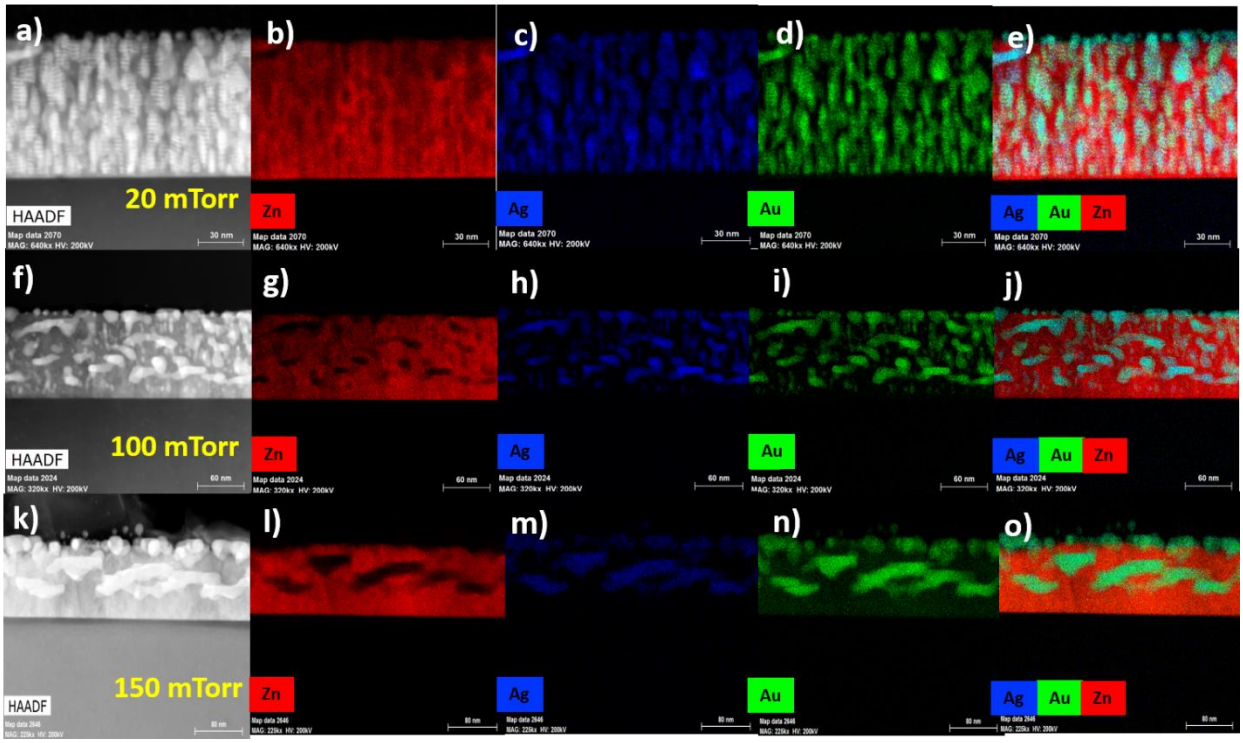

Figure 5.7 EDS mapping of different films and corresponding HAADF. a-e) mapping for 20 mTorr. f-j) mapping of 100 mTorr. k-o) mapping of 150 mTorr.

Bimetallic Ag_xAu_{1-x} nanoalloys are beneficial for their plasmonic response. The optical properties of ZnO-Ag_xAu_{1-x} oxide-alloyed nanocomposite deposited at different background pressure were investigated through UV-Vis spectroscopy, depicted in Figure 5.8. The surface plasmon resonance of each film is indicated by a minimum in each plot and marked in the figure. For the nanocomposite deposited under vacuum, there is a surface plasmon resonance at 492 nm. As the background pressure increases to 20 mTorr, the plasmonic resonance is 512 nm. At 150 mTorr, the surface plasmon is further red shifted to 545 nm and the plasmonic resonance at 150 mTorr is 595 nm. Here, a red shifting of the plasmonic resonance with increasing background pressure is observed. The tuning of the plasmon resonance from 492 nm at vacuum to 595 nm at 150 mTorr could be related to the effective microstructure and morphology tuning as discussed above. Specifically, increasing the background pressure will cause a red shift of the plasmon resonance. Interestingly, the red-shift with increasing Ag content is converse to what is usually observed. Therefore, the morphology tuning might be one of the dominant factors in terms of plasmon resonance tuning as growing more lateral pillars from vacuum to 150 mTorr resulted in the red-shifted plasmon resonance. The significant morphology variation from vertically-aligned

pillars at low pressure to the lateral pillar at high pressure could result in a transition of different plasmon excitation [259]. In the UV-Vis measurement, the light beam is traveling through the film, such that at low pressure the transverse plasmon resonance is more dominantly excited. As the pressure increases and the morphology of the pillars becomes lateral, it could be that the longitudinal plasmon resonance is more dominantly excited. On the other hand, composition tuning could also play a role in the tuning effect, as Au content is found to drop with increasing background pressure, as evidenced in the Figure 5.3. More detailed studies are needed to clearly understand the mechanism of plasmon tuning in this system.

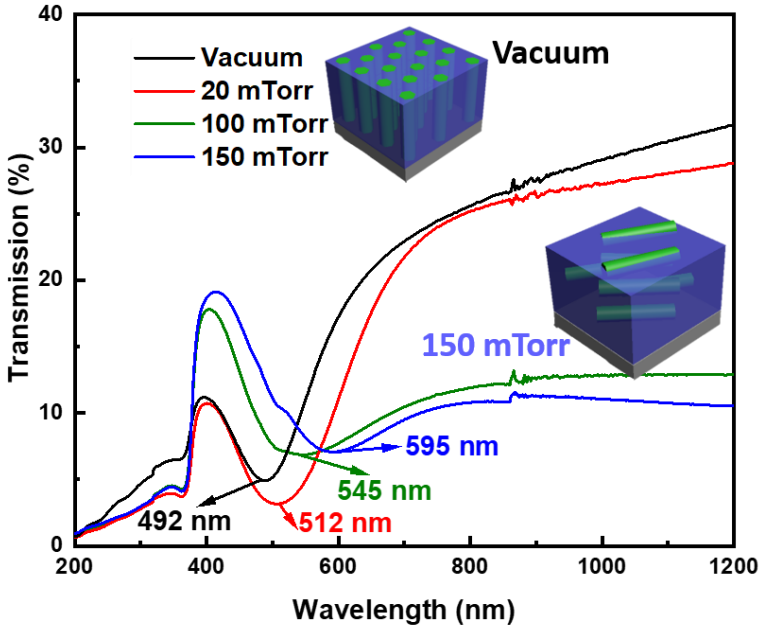

Figure 5.8 Transmission UV-Vis spectrum showing optical tuning, numbers on graph indicate plasmonic peak.

Because of the anisotropic nature of the hybrid nanoalloy morphology, the dielectric function and anisotropic optical properties through spectroscopic ellipsometry (see methods) have been explored. Experimental setup and the imaginary permittivity for each film can be found in Figure 5.9. Data for the measured ellipsometry parameters of psi and delta and corresponding models can be found in Figure 5.10 and Figure 5.11. The real part of the permittivity for each hybrid thin film deposited at different background pressure is plotted in Figure 5.12. All films demonstrate the properties of hyperbolic metamaterials (HMM) and the

hyperbolic dispersion is coupled with epsilon near zero permittivity (ENZ). HMMs have a dielectric function that acts as a metal in one direction and a dielectric in the perpendicular direction [181]. In Figure 5.12, the regime for hyperbolic dispersion is marked on each graph. A Type I HMM with isofrequency curve of a hyperboloid of two sheets and can support only high k states, is denoted on the graphs in Figure 5.12 as a purple region. The Type II HMM with isofrequency curve of a paraboloid of one sheet that can support both high and low k states, is denoted with a yellow shading. Representative isofrequency curves are inset into the graphs of Figure 5.12.

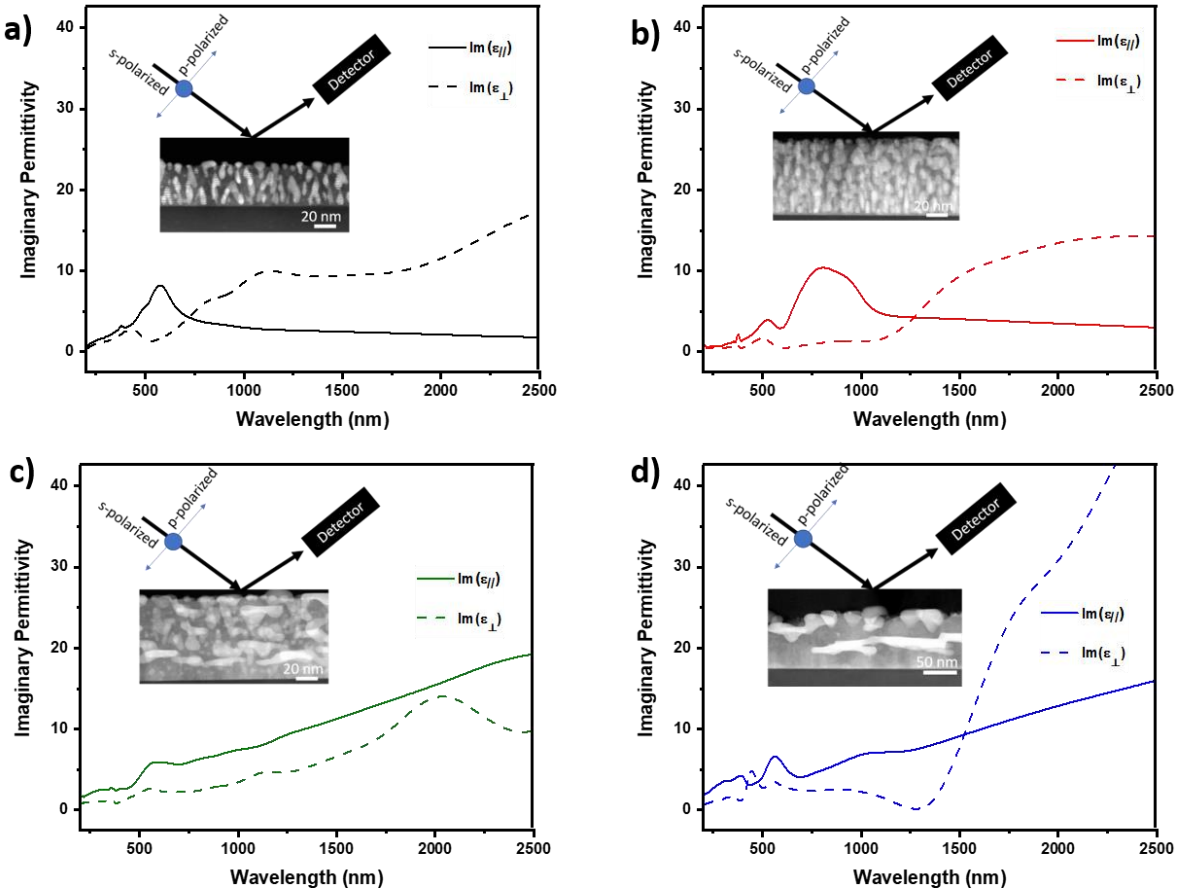

Figure 5.9 Dielectric function tuning. In-plane and out-of-plane imaginary permittivity for films deposited under a) vacuum, b) 20 mTorr, c) 100 mTorr, and d) 150 mTorr. Inset is the experimental setup.

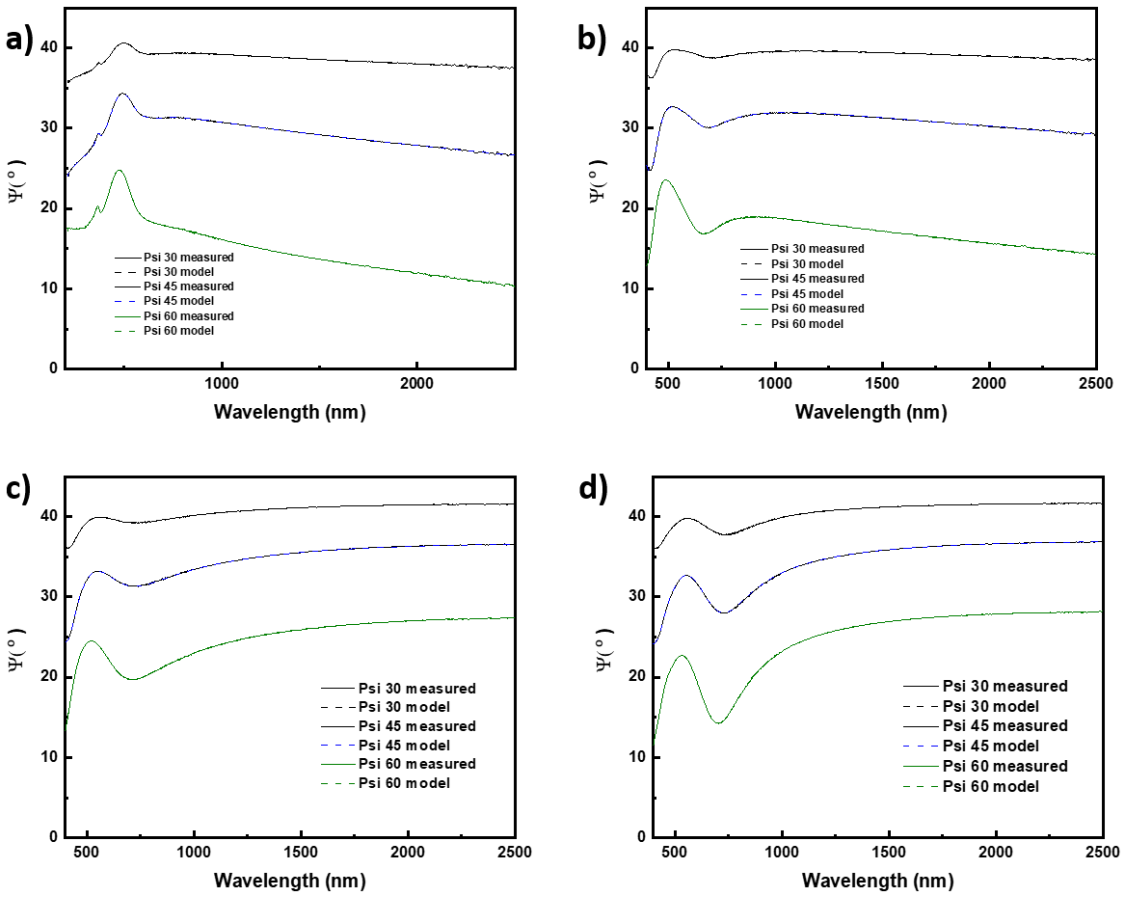

Figure 5.10 Psi. Measured and model psi for films deposited under a) vacuum, b) 20 mTorr, c) 100 mTorr, d) 150 mTorr.

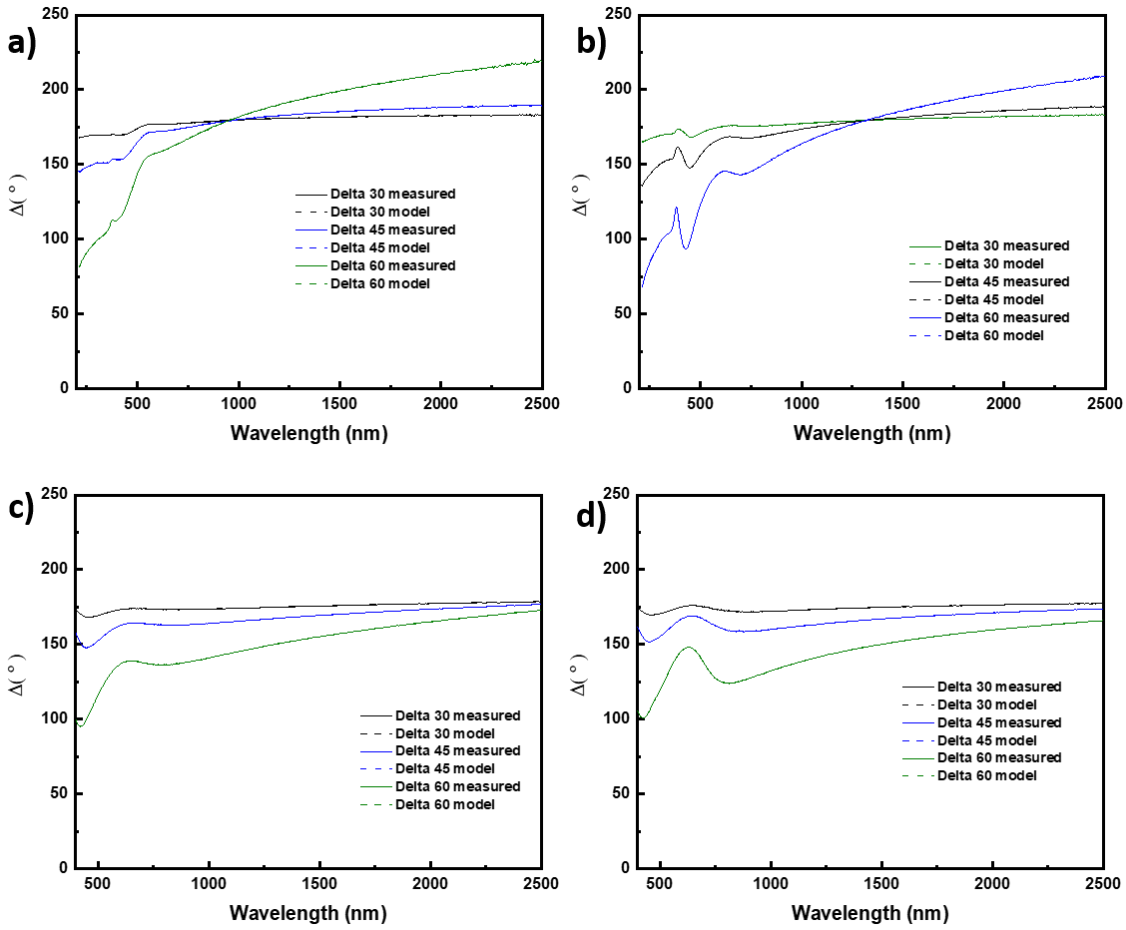

Figure 5.11 Delta. Measured and model data for films deposited at a) vacuum, b) 20 mTorr, c) 100 mTorr, d) 150 mTorr.

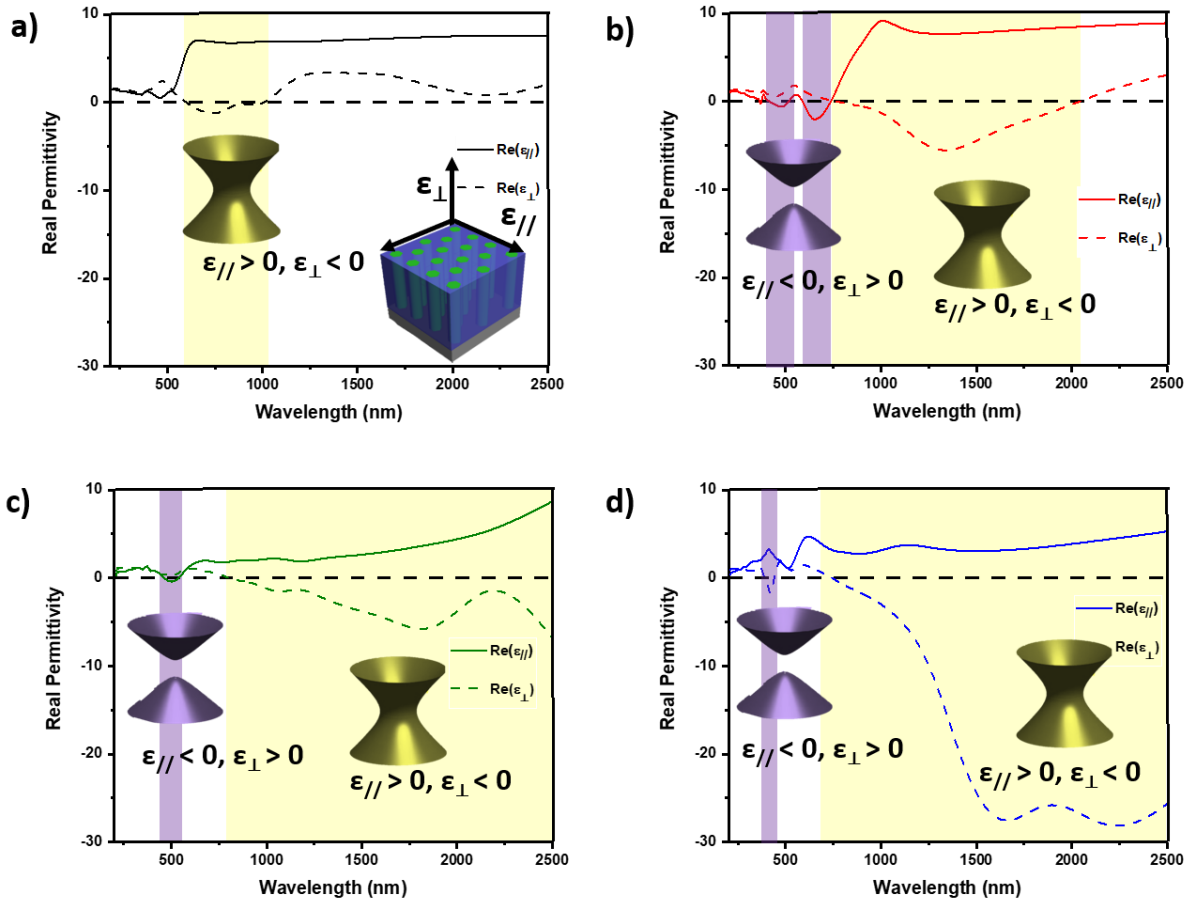

Figure 5.12 Dielectric function tuning. Real part of dielectric function for a) vacuum, b) 20 mTorr, c) 100 mTorr and d) 150 mTorr. Inset are representative isofrequency curves indicating type of hyperbolic metamaterial, yellow represents a type I hyperbolic metamaterial with surface of hyperboloid of one sheet and purple represents type II hyperbolic metamaterial with surface of hyperboloid of two sheets.

Angular dependent ellipsometry data was measured and fitted for all the samples. The real part of permittivity for the vacuum deposited film can be found in Figure 5.12a. This film is a Type II HMM with a hyperbolic regime spanning parts of the visible and near-infrared (NIR) from 593 nm to 1023 nm. In this regime, the components out-of plane to the anisotropy axis $\varepsilon_{\perp} < 0$ and in-plane $\varepsilon_{//} > 0$ and $\varepsilon_{\perp}$ has ENZ permittivity at 593 nm and 1023 nm. The real part of permittivity for the film deposited at 20 mTorr is depicted in Figure 5.12b. Upon increasing the background pressure to 20 mTorr, the Type II hyperbolic regime in the visible – near infrared increases in size to include a range of 736-2050 nm. Moreover, two new Type I hyperbolic regimes occur from 400-520 nm and 590-736 nm, where $\varepsilon_{//} < 0$ and $\varepsilon_{\perp} > 0$. The out-of-plane ($\varepsilon_{\perp}$) component has ENZ permittivity at 736 and 2060 nm and the in-plane ($\varepsilon_{//}$) has ENZ permittivity at 400, 520, 590, and 736 nm. Upon increasing background deposition pressure to 100 mTorr, the hyperbolic properties are further tuned. In the 100 mTorr deposited film, the Type II regime now spans from 788 to 2500 nm, the end of the measured spectrum. Compared with the 20 mTorr film, there is only one Type I regime occurring from 463 – 560 nm. The in-plane component has ENZ at 463 and 560 nm while the out-of-plane component has ENZ permittivity at around 788 nm. Further increasing the background deposition pressure to 150 mTorr maintained the Type II regime and decreased the size of the regime in the visible and is changed to Type II hyperbolic dispersion. The real part of the permittivity for the 150 mTorr sample is plotted in Figure 5.12d. The Type II HMM regime occurs from 740 - 2500 nm and 387 – 440 nm. The in-plane component has ENZ permittivity at 387, 440 nm, and 740 nm. Pressure induced dielectric function tuning has also been observed in the ZnO-Au VAN system [247].

The work in this report demonstrates the robust tunability of the hybrid plasmonic ZnO-Ag_xAu_{1-x} system and the respective effect on morphology and material properties. Thin films grown in vacuum produce vertically aligned nanoalloy pillars that can be tuned more laterally by introducing and increasing an oxygen background pressure during growth. The change in the morphology also leads to a tunability of the optical properties and composition of the nanoalloy, where increasing oxygen pressure will decrease Au and red-shift the plasmonic response. Due to the self-assembled nature of the growth and one-step pulsed laser deposition approach, there are a robust number of parameters that can be tuned to achieve new oxide-nanoalloy morphology and property effects. Future studies could investigate the result of frequency, substrate

temperature, or laser energy tuning on the ZnO-Ag_xAu_{1-x}. Moreover, due to the ZnO support and highly tailorable morphology, the ZnO-Ag_xAu_{1-x} system broadens the applicability of nanoalloy thin films toward future integrations where previous nanoalloys are restricted in their use due to instability. Due to the robustness of the oxide-nanoalloy approach, other nanoalloys can be explored such as magneto-optic candidates like Ni_xCu_{1-x} or Ni_xAu_{1-x} and other plasmonic candidates like Ag_xCu_{1-x} and Ag_xAl_{1-x}. This hybrid ZnO-Ag_xAu_{1-x} system with tunable optical properties, such as tailorable plasmon resonance range, could find applications as optical device components that requiring specific wavelength range in optical absorption, sensing and detection.

5.5 Conclusions

In this work, ZnO-Ag_xAu_{1-x} nanocomposite thin films with highly tunable morphology, composition, and optical properties were demonstrated. Films at different background pressures were deposited, each with unique morphology and properties. The film deposited in vacuum has a vertically aligned nanopillar structure, which was tuned toward irregular lateral nanopillar growth at high background pressure. The hybrid oxide-nanoalloy materials in this report demonstrated strong plasmonic resonance in the UV-Vis regime that was highly tunable. Moreover, due to the inherent anisotropy of the nanocomposite morphology, they have interesting anisotropic dielectric function with hyperbolicity in useful wavelengths. We found the film deposited at 20 mTorr, with high density pillar morphology, to have the most interesting optical properties in terms of practical applications due to a broad wavelength range of hyperbolic dielectric function and relatively low absorption. This work presents the broad tunability in hyperbolicity and plasmonic properties using the design of metallic alloyed nanopillars in oxide matrix to address the versatile optical property needs in optical components and devices.

6. ZNO-FERROMAGNETIC METAL VERTICALLY-ALINED NANOCOMPOSITE THIN FILMS FOR MAGNETIC, OPTICAL, AND ACOUSTIC METAMATERIALS

6.1 Overview

Magnetoacoustic waves generated in piezoelectric and ferromagnetic coupled nanocomposite films through magnetically driven surface acoustic waves present great promise of loss-less data transmissions. In this work, ferromagnetic metals of Ni, Co and Co_xNi_{1-x} are coupled with piezoelectric ZnO matrix in a vertically-aligned nanocomposite (VAN) thin film platform. Oxidation was found to occur in the cases of ZnO-Co, e.g., ZnO-CoO VAN forms. An alloy approach of Co_xNi_{1-x} has been explored to overcome the oxidation during growth. Detailed microstructural analysis reveals distinct phase separation between the ZnO and the metallic phases. Highly anisotropic properties including anisotropic ferromagnetic properties and hyperbolic dielectric functions are found in the ZnO-Ni and ZnO-Co_xNi_{1-x} systems. The magnetic metal ZnO-based hybrid metamaterials in this report present great potential in coupling of optical, magnetic, and piezoelectric properties towards future magnetoacoustic wave devices.

6.2 Introduction

Recently, magnetoacoustic wave devices have been realized as a new avenue for low-loss data transmission and next generation on-chip communication. [260] In the seminal work, interdigitated ferromagnetic Ni film was grown on $LiNbO_3$ substrates and magnetoacoustic waves were generated through the magnetoelastic effect over millimeter distances [260]. The magnetoelastic effect is a change of magnetic field in response to a mechanical stress, or vice versa. In the Ni-$LiNbO_3$ coupled device, ferromagnetic properties in the Ni film were tuned by strain in the piezoelectric $LiNbO_3$ driven by surface acoustic waves. The hybridized piezoelectric-ferromagnetic Ni-$LiNbO_3$platform [260] was used to drive magnetoacoustic waves with high amplitude over long distances, overcoming the magnetic dampening effects usually hindering application of ferromagnets by use of the magnetoelastic effect [260]. magnetoacoustic waves have also been realized in dipolar-coupled bilayer ferromagnetic thin films grown on $LiNbO_3$ substrates towards application in acoustic resonators [261].In this case,

non-reciprocity was also measured, demonstrating breaking of the time reversal symmetry [262,263]. Breakage of time reversal symmetry implies the existence of certain topological states [264] existing in these piezoelectric- ferromagnetic coupled composites and could prove as effective approaches for realizing topological phononic metamaterials which could allow for loss-less transmission of elastic waves in all directions [265].

Very recently, the oxide-metal vertically-aligned nanocomposite (VAN) platform has gained attention as an effective design approach for hybrid plasmonic metamaterials [143,247,248,266]. Moreover, anisotropic magnetic and electrical conductivity can be designed into the platform [142,208]. In the oxide-metal vertically-aligned nanocomposite, two immiscible phases are self-assembled through a co-deposition resulting in the epitaxial growth of nanopillars of the metallic phase in the oxide matrix . The benefits of the VAN are the highly anisotropic microstructure and physical properties in the systems, very uniformly distributed nanopillars, the high-quality and tailorable epitaxial growth, and the ability to couple magnetic, optical, and electrical multifunctionalities [108,145,267,268].

In this letter, piezoelectric ZnO matrix is grown with ferromagnetic metals of Ni, Co, and nanoalloy Co_xNi_{1-x}. ZnO is selected as the matrix due to its strong dielectric and piezoelectric response [68,269,270]. Co and Ni are selected for the pillar phase due to their strong ferromagnetic response and potential plasmonic properties [271–273]. The schematic diagram in Figure 6.1 depicts the design multifunctionalities of the nanocomposite grown in this report, including both hyperbolic metamaterial response due to plasmonic ferromagnetic pillars of Ni and Co embedded into dielectric matrix and for the potential magnetoacoustic wave propagation due to piezoelectric-ferromagnetic coupling. The issues to overcome include the potential oxidation of Ni and Co, in which the nanoalloy Co_xNi_{1-x} is proposed to overcome oxidation issues. Nanocomposite thin films of ZnO-Ni, ZnO-Co, and ZnO-Co_xNi_{1-x} were grown, and their morphology was characterized through X-ray diffraction and transmission electron microscopy. Optical properties are characterized through spectroscopic ellipsometry, and magnetic properties were measured with MPMS SQUID to explore the anisotropic nature of these ZnO-ferromagnetic metal hybrid metamaterials.

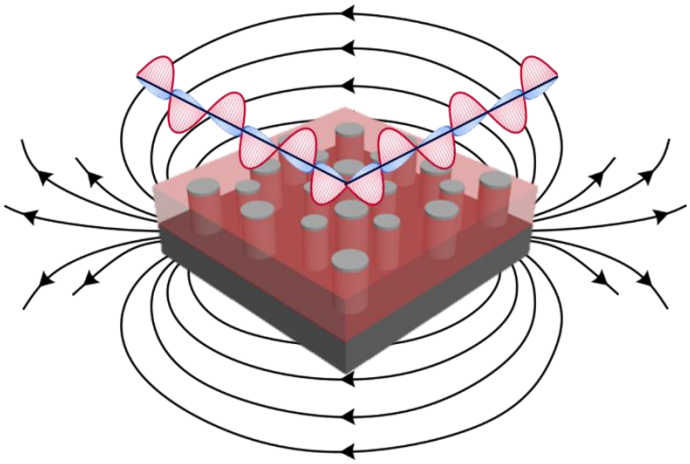

Figure 6.1 Ferromagnetic metal and ZnO nanocomposite design with magnetic and optical response.

6.3 Experimental

6.3.1 Thin Film Growth

Thin films of ZnO-Co, ZnO-Ni, and ZnO-Co_xNi_{1-x} were grown through the pulsed laser deposition method on c-cut sapphire (0001) substrates. ZnO-Ni and ZnO-Co_xNi_{1-x} were grown at 500^{o}C and ZnO-Co was grown at both 500^{o}C and 700^{o}C. A KrF excimer laser (Lambda Physik Complex Pro 205, λ = 248 nm) was used for all depositions with laser energy of 420 mJ focused at an incident angle of 45^o. Target-substrate distance was kept constant at 4.5cm. All films were grown in a vacuum environment which was pumped down to ~10^{-6} mTorr from atmospheric pressure after loading and after each deposition, were cooled at a rate of 15^{o}C/min. The films were ablated from composite targets prepared through a conventionsal sintering method. The ZnO-Ni and ZnO-Co_xNi_{1-x} were consisting of 30% molar ratio of metal with the alloy mixed 1:1 Co:Ni. The ZnO-Co composite target contained 1:1 ZnO:Co composition

6.3.2 Microstructure characterization

Film morphology was characterized through XRD, TEM, and STEM coupled with EDS-mapping. XRD scans of θ-2θ were conducted using a Panalytical X'Pert X-ray diffractometer wit Cu K_α radiation. Bright field TEM, STEM, SAED patterns and eds-mapping was performed in a FEI Talos F200X TEM. Samples for electron microscopy were prepared, for both cross-

section and plan-view, via a standard grinding procedure which entails manual grinding, polishing, dimpling, and a final ion milling step to achieve electron transparency. (PIPS 691 precision ion polishing system, 5 KeV for cross-section and 4-4.5 KeV for plan-view sample)

6.3.3 Optical measurements

Ellipsometry experiments were carried out on an RC2 Spectroscopic ellipsometer (J.A. Woollam Compnay). Four angles 40^o, 50^o, 60^o, and 70^o were measured from a spectrum range of 210 – 2500 nm. Psi and delta data were obtained from ellipsometry experiments and then fit with an uniaxial model coupled with B-spline model were used to discern anisotropic permittivity properties of composite films, an agreeable mean square error (MSE) < 5 was obtained for all film models.

6.3.4 Magnetic Measurements

Magnetic property measurements were carried out on the MPMS SQUID (Quantum design MPMS 3) system at both 10K and 300K. A magnetic field of 5000 Oe was applied perpendicular and in-plane for measuring in-plane and out of plane magnetic response.

6.4 Results and Discussion

Ferromagnetic metals of Ni, Co, and their nanoalloy Co_xNi_{1-x} are combined with dielectric/piezoelectric ZnO matrix to form vertically-aligned nanocomposite thin films. Films are grown on c-cut sapphire substrates. The difficulty in growing ferromagnetic metal/oxide composites comes from tendency of Co and Ni to easily oxidize during the oxide growth. First vacuum deposition was explored to minimize the metal oxidation during growth. Microstructural characterization of the ZnO-Ni nanocomposite is depicted in Figure 6.2. The out-of plane 2θ scan is shown in Figure 6.2a, which peaks from ZnO (0002) and Ni (111) were measured. From the scan, minor oxide peaks of NiO (111) appeared, indicating some oxidation of the Ni. A scanning transmission electron microscopy (STEM) micrograph of the cross-section of ZnO-Ni VAN is shown in Figure 6.2b. STEM contrast is derived from the atomic number, where contrast is ~$Z^{1.4}$, Z_{Ni}=28 and Z_{Zn}=30, leading to very little contrast in the STEM image between ZnO and Ni. Energy dispersive (EDS) elemental mapping was performed in Figure 6.2c-e. The combined

map of Zn and Ni is demonstrated in Figure 6.2c, showing more clearly the morphology of the ZnO-Ni VAN as compared with the STEM image in Figure 6.2b, Ni grows as wide pillars embedded into the ZnO matrix. The individual maps for Ni and Zn are shown in Figure 6.2d and e, respectively and not much overlap is shown as Ni and ZnO grow separate phases without much interdiffusion.

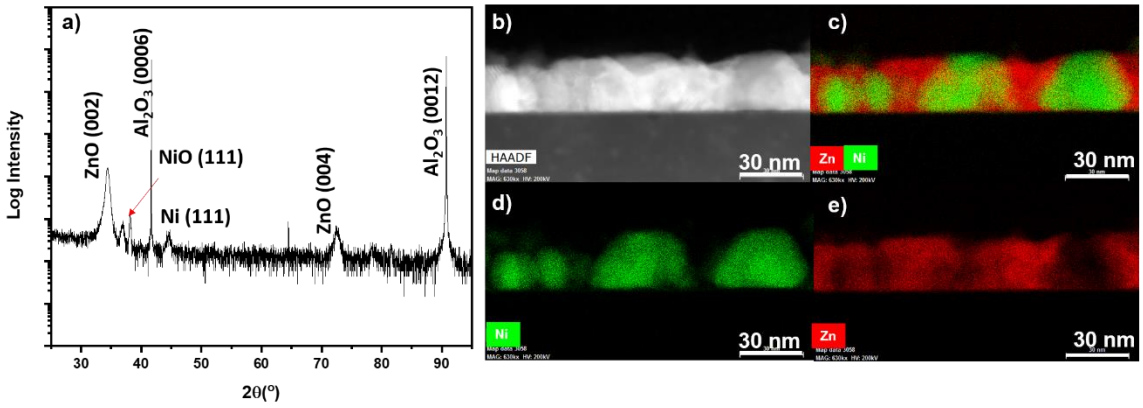

Figure 6.2 Microstructural characterization of ZnO-Ni nanocomposite. a) 2θ scan. b) Cross-section STEM image. c) Combined EDS-mapping. d) EDS-mapping for Ni. e) EDS-mapping for Zn element.

Similarly, a ZnO-Co nanocomposite was explored in this work and the results of the microstructure characterization are shown in Figure 6.3. For ZnO-Co composite, two different substrate temperatures of 500°C and 700°C were explored. The XRD 2θ for 500°C and 700°C are shown in Figure 6.3a and b, respectively. At high temperature growth of 700° in Figure 6.3b, the film grows with ZnO (0002) and CoO (111) out-of plane orientation and no Co peaks were found, indicating the ZnO-Co composite actually grows as a ZnO-CoO oxide-oxide nanocomposite. The temperature was lowered to 500°C in Figure 6.3a to explore if the high substrate temperature of 700°C was leading to oxidation due to diffusion, but in the 500°C 2θ the same peak for CoO (111) is found and no Co peaks were identified. A cross-section STEM image of the 500°C sample is shown in Figure 6.3c, again with little contrast due to the similar atomic number of Z_{Zn} =30 and Z_{Co} = 27. EDS-mapping of the ZnO-Co film grown at 500°C was performed and shown in Figure 6.3d-f. The combined map in Figure 6.3d shows the morphology, with Co rich peaks growing inside ZnO matrix. Individual maps for Zn and Co are shown in Figure 6.3e and f, respectively.

From the EDS-mapping, there is some interdiffusion between the Zn and Co areas, which is consistent with the literature; i.e., Co diffuses easily into ZnO to form phases of Co-doped ZnO [274–277]. The microstructure STEM cross-section image of the ZnO-Co composite grown at 700°C is shown in Figure 6.3g and the EDS mappings are depicted in Figure 6.3h-i. At higher temperature Co rich pillars grow in the ZnO matrix with some interdiffusion between the Co and ZnO, similar to the 500°C growth.

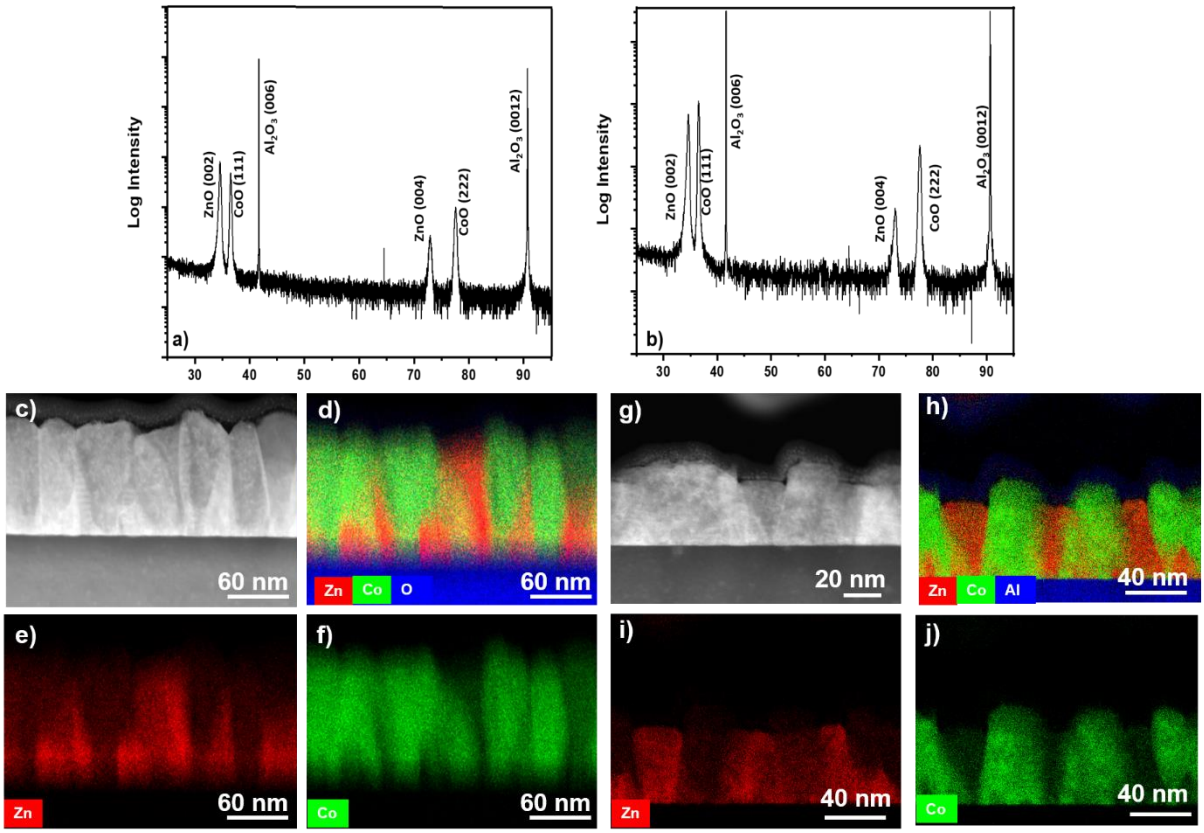

Figure 6.3 Microstructural characterization of ZnO-Co VAN grown at 500 °C and 700 °C. a) 2θ for 500 °C. b) 2θ XRD scan 700 °C.. c) Cross-section STEM for 500°C. d) Combined EDS-mapping at 500°C. e) EDS-mapping for Zn at 500°C. f) EDS-mapping at 500°C for Co. g) Cross-section STEM at 700°C. h) combined EDS-mapping at 700°C. i) EDS-mapping at 700°C for Zn. j) EDS-mapping at 700°C for Co.

To overcome the oxidation issues faced in single phase ferromagnetic metal co-growth with ZnO, a nanoalloy approach was adapted. Recently, the Au_xAg_{1-x} nanoalloy was utilized in the ZnO VAN system to overcome particle-in matrix morphology and oxidation issues in the ZnO-Ag system and improve optical properties [248]. A nanoalloy of Co_xNi_{1-x} was designed to form ZnO-Co_xNi_{1-x} VAN. It is hypothesized that the alloy formation is preferential over diffusion into the ZnO matrix or oxidation. Both Ni and Co are located next to each other on the periodic table (Z_{Ni}=28 and Z_{Co}=27) and have very similar atomic radius, with r_{Co} = 0.135 nm and r_{Ni} = 0.135 nm [278] , making it easy for solid solution alloying. Moreover, it is possible for Co to form a metastable face-centered cubic lattice (FCC) with similar structure to the Ni FCC lattice, with lattice parameter A_{Co}=3.54 nm and A_{Ni}=3.52 nm. [279] Ni can also form a metastable hexagonal close-pack phase with similar lattice parameter as stable HCP Co [280]. The results of microstructure characterization of ZnO-Co_xNi_{1-x} nanocomposite are shown in Figure 6.4. The XRD 2θ scan are presented in Figure 6.4a and peaks from ZnO (0002) and the nanoalloy are shown. Interestingly, two peaks for the alloy were measured, one corresponding to Co_xNi_{1-x} (100) and another at Co_xNi_{1-x} (111). The (100) peak may correspond to a Co-rich hexagonal phase and the (111) peak may correspond to a Ni-rich cubic phase. The cross-section STEM is shown in Figure 6.4b, with similar issue as both ZnO-Ni and ZnO-Co composite having little contrast due to the similar atomic number of Zn, Co, and Ni. The EDS-mapping for cross-section is depicted in Figure 6.4c-e, including combined, Co, and Ni and the EDS mapping of the Zn matrix cross-section is shown in Figure 6.5a. From the EDS-mapping, it is interesting to note that the alloy formation is not homogeneous. Ni-rich particles form at near the sapphire substrate and some pillars appear to be Co-rich. A plan-view STEM is shown in Figure 6.4f with plan-view EDS mapping depicted in Figure 6.4g-I for combined, Ni, and Co; the Zn plan-view EDS-mapping is shown in Figure 6.5b. In the plan-view, Ni-rich particles with cobalt-rich areas forming with much larger and irregular shape. The delineation between the alloy phase and ZnO matrix is evidenced in the Zn plan-view EDX mapping.

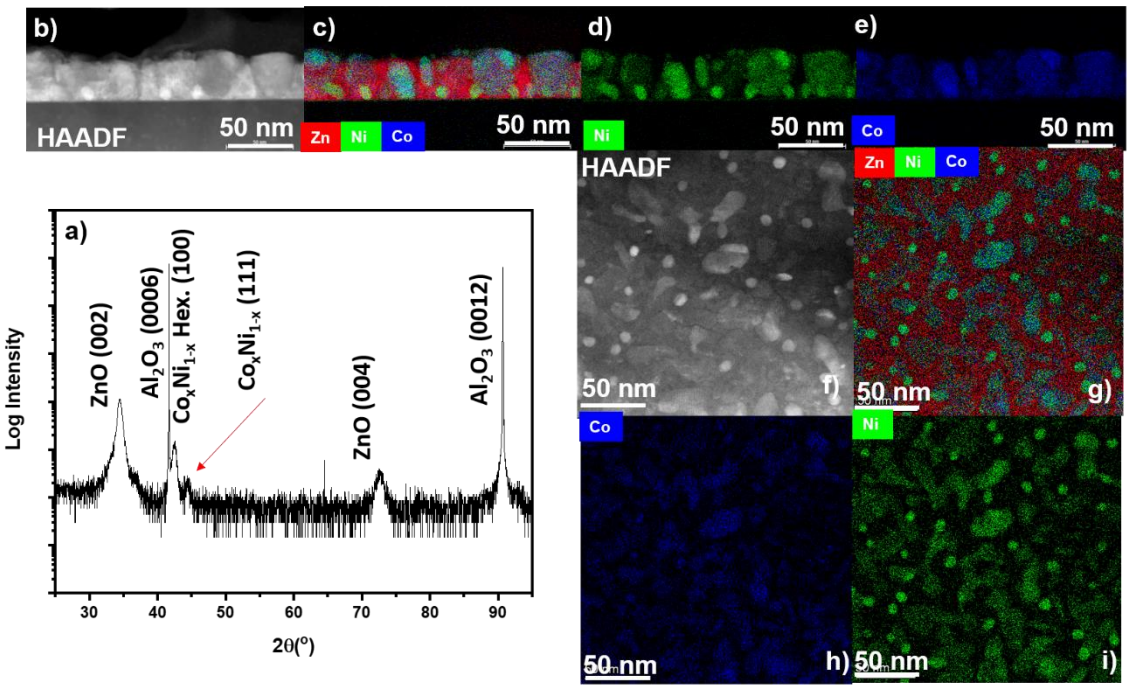

Figure 6.4 Microstructural characterization of ZnO-Co_xNi_{1-x} nanocomposite. a) 2θ scan. b) cross-section STEM. c) Combined EDS-mapping. d) EDS mapping Ni element. e) EDS-mapping element. f) In-plane STEM image. g) Combined EDS-mapping plan-view. h) EDS-mapping Co. j) EDS-mapping Ni element.

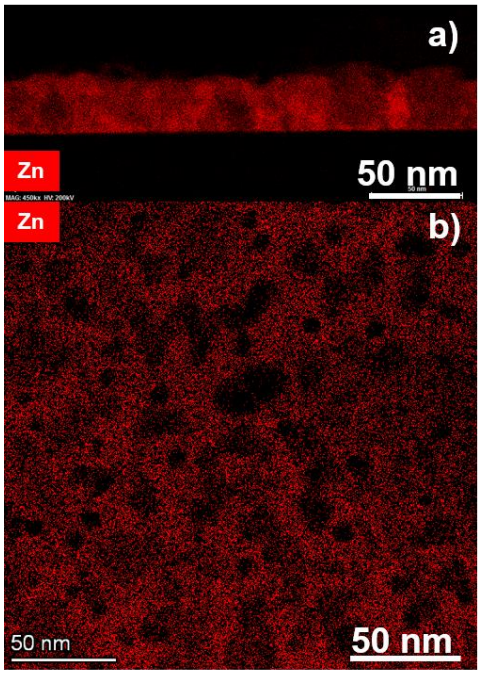

Figure 6.5 EDS-mapping of Zn in ZnO-Co_xNi_{1-x} VAN. a) Cross-section. b) Plan-view.

A main purpose of the films grown in this report is to realize ferromagnetic properties in a piezoelectric and dielectric matrix. Anisotropic magnetic hysteresis loop was measured for ZnO-Ni, ZnO-Co, and ZnO-Co_xNi_{1-x} nanocomposites by SQUID MPMS. The ZnO-Ni and ZnO-Co_xNi_{1-x} were measured at 10K and 300K to investigate ferromagnetic properties at low and room temperatures and presented in Figure 6.6. Magnetic anisotropy is measured by applying a magnetic field parallel and perpendicular to measure the in-plane and out-of plane magnetic response. The resulting hysteresis loops in Figure 6.6 demonstrate strong ferromagnetic response for both direction at 10K and 300K in ZnO-Ni and ZnO-Co_xNi_{1-x} nanocomposites with some interesting difference. The ZnO-Ni composite measurement are shown in the top row at 10K in Figure 6.6a and 300K in Figure 6.6b. At 10K, the hysteresis loop remains somewhat similar in the in-plane and out-of plane direction with the magnetic moment M_s and the magnetic coercivity H_c having similar values. At room temperature, the anisotropy is much more dramatic with the in-plane direction having much higher coercive field H_c but lower magnetic moment M_s.; interestingly, the ZnO-Ni at room temperature behaves as a soft magnet in the out-of plane direction and as a hard magnet in the in-plane direction. The shape-anisotropy seen in the magnetic data at room temperature could be attributed to the morphology seen in Figure 6.3. Ni pillars have greater width than height, therefore it could be that a thicker film could result in more out-of plane magnetic anisotropy.

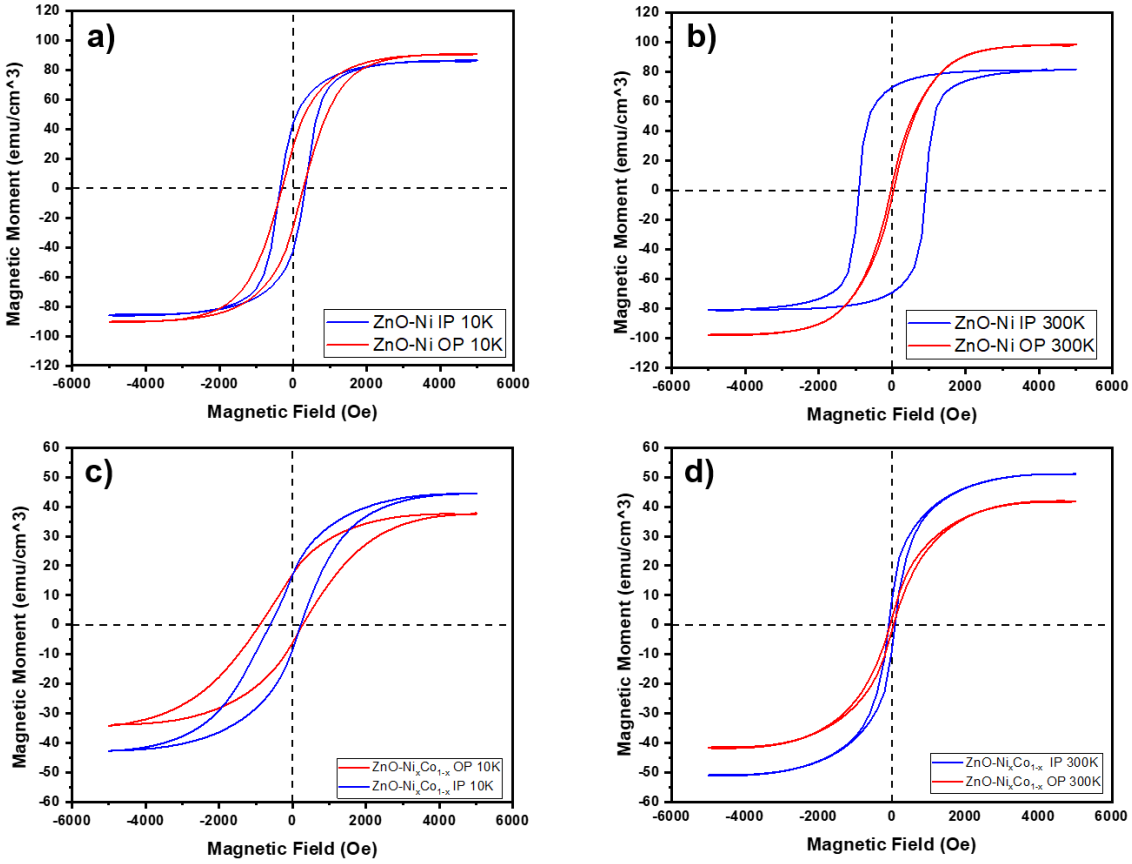

Figure 6.6 Anisotropic magnetic measurement. a) ZnO-Ni at 10K, b) ZnO-Ni at 300K, c) ZnO-Ni_xCo_{1-x} at 10K, d) ZnO-Ni_xCo_{1-x} at 300K.

Magnetic measurements were also performed on the ZnO-Co_xNi_{1-x} composite thin film at 10K in Figure 6.6c and 300K in Figure 6.6d. At 10K, ZnO-Co_xNi_{1-x} demonstrated anisotropic magnetic behavior with the magnetic moment M_s much larger in the in-plane direction than in the out-of plane direction, which was also true for the 300K sample. With increasing the measurement temperature to 300K, the coercive field H_c was decreased. It is interesting to note from the data that the ZnO-Co_xNi_{1-x} displays exchange bias, more noticeable at the 10K measurement than at 300K. An enlarged view of the hysteresis loop is shown in Figure 6.7. The exchange bias indicates the presence of antiferromagnetic domains in the film, which could be the result of the formation of oxide species or Co-doped ZnO. At 10K, the in-plane coercive field H_C is located at -887 and 279 O_e while in the out-of plane direction is located at -607 and 206 O_e. At 300K, the coercive field for the in-plane direction is -83 and 88 O_e while the out of plane is -

46 and 48 O_e. The exchange bias is more noticeable at the lower temperature, as the sample is heated it may pass through the Neel temperature of the antiferromagnet present, leading to disordering of the domains and reducing the exchange bias effect. The exchange bias displayed in the ZnO-Co_xNi_{1-x} nanocomposite may lead to applications in giant magnetoresistance (GMR) device and technologies [281].

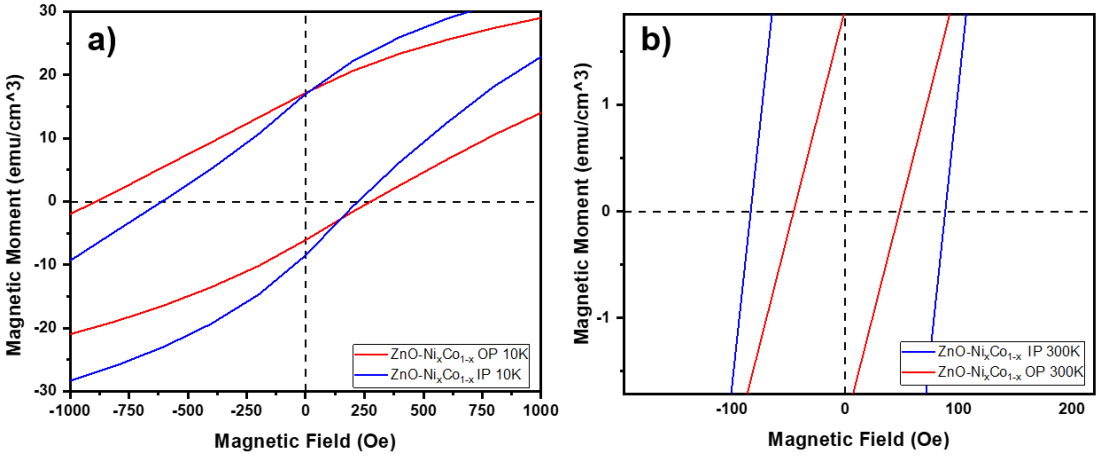

Figure 6.7 Zoomed features for hysteresis loop of ZnO-Co_xNi_{1-x} at a) 10K and b) 300K.

Anisotropic magnetic measurements were also performed at 300K for the ZnO-Co sample in Figure 6.8 for films grown at 500°C and 700°C. Figure 6.8a shows in-plane measurement and Figure 6.8b shows the out-of plane measurement. ZnO-Co demonstrates ferromagnetic response when grown at 700°C and a paramagnetic response when grown at 500°C. The paramagnetic response at 500°C is in line with the microstructure characterization and indicative of the ZnO-CoO oxide-oxide composite growth. When grown at 700°C, the ZnO-Co system demonstrates slightly anisotropic ferromagnetic response, with the coercive field being slightly larger in the out-of plane direction. The induction of ferromagnetic response in the system may be due to small cobalt-rich areas precipitating due to the high growth temperature.

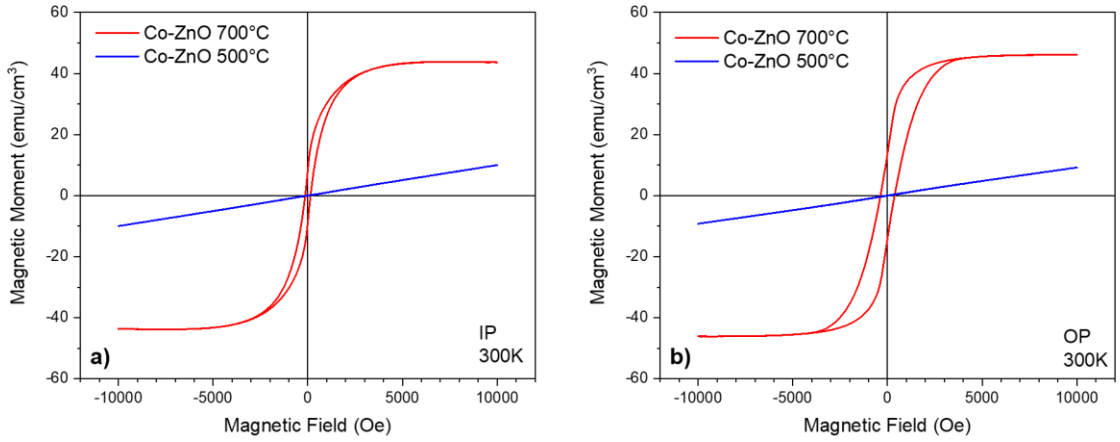

Figure 6.8 Magnetic measurement for ZnO-Co nanocomposite. a) In-plane and b) out-of plane.

Both Ni and Co have been reported to have a plasmonic response in the near-infrared regime [272,273,282,283]. The plasmon resonance is a discrete excitation of the electron cloud of a metal at the interface with a dielectric in response to light absorption [152]. Due to the anisotropic morphology of the metallic inclusions when grown in the dielectric ZnO, it could be possible to realize hyperbolic dielectric response, e.g., behavior as a metal in one-direction and as a dielectric in the opposite direction. Both Ni and Co have been studied as low-loss alternatives for noble Au and Ag in plasmonic sensors and hyperbolic metamaterials [154,282,284]. The complex dielectric function of ZnO-Ni and ZnO-Co_xNi_{1-x} composites were modeled through spectroscopic ellipsometry and presented in Figure 6.9. The dielectric model is based on psi and delta measurements in Figure 6.10 and is a uniaxial b-spline with backside correction. As seen in Figure 6.9, both ZnO-Ni and ZnO-Co_xNi_{1-x} demonstrate hyperbolic response in Figure 6.9a and b, respectively. In Figure 6.9a, ZnO-Ni has an epsilon-near zero (ENZ) permittivity point at around 2100 nm. The ZnO-Co_xNi_{1-x} film in Figure 6.9b displayed its ENZ point near 1700 nm. Both composites are considered type II metallic hyperbolic metamaterial, since in both material $\varepsilon_{zz} > 0$ and $\varepsilon_{\perp} < 0$. Type II hyperbolic metamaterial have isofrequency curve of one sheet and can support high density of k-states, making them highly desirable in application [178]. The imaginary permittivity for ZnO-Ni and ZnO-Co_xNi_{1-x} in Figure 6.9c and d, respectively, is related to the absorption in the film where lower values are more desirable for application. Absorption in the films in the work is relatively

low, demonstrating the ferromagnetic/ZnO composite thin films as alternative low-loss metamaterials.

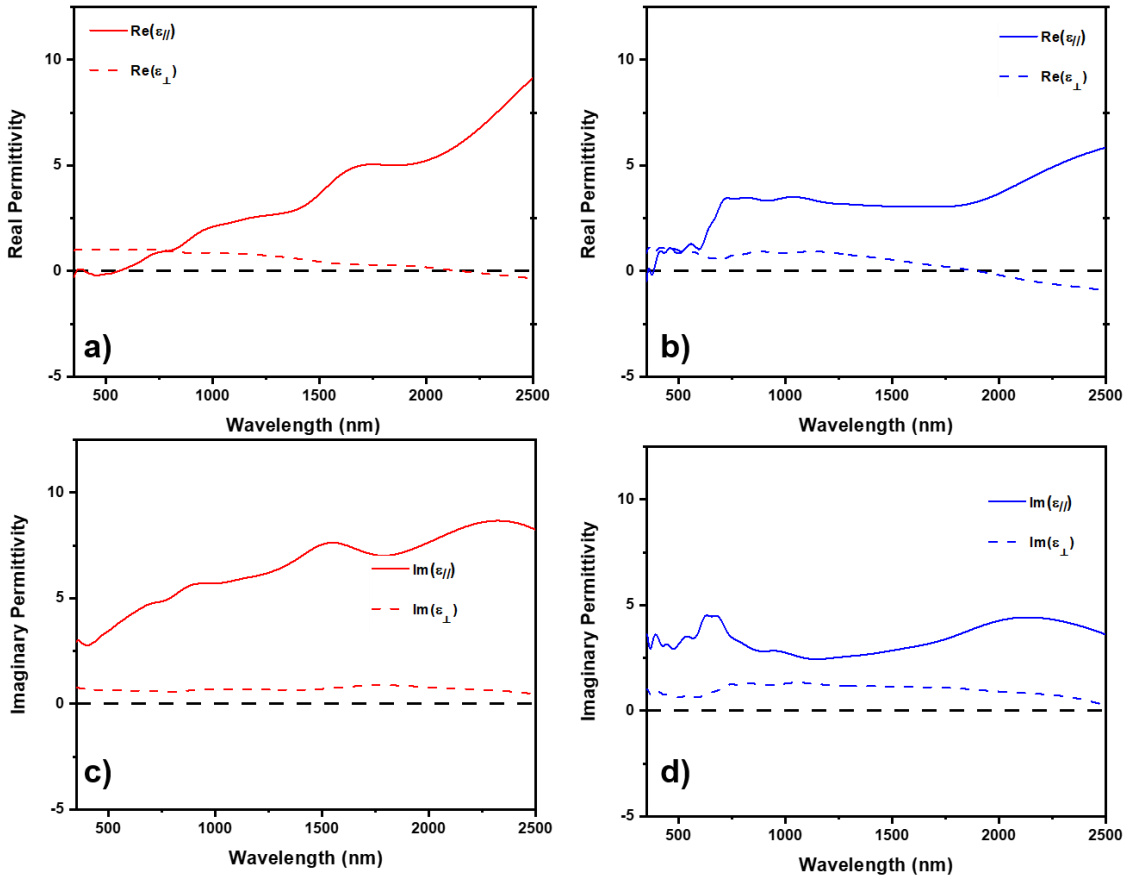

Figure 6.9 Measured and model real and imaginary permittivity. Real permittivity for a) ZnO-Ni and b) ZnO-Co_xNi_{1-x}. Imaginary permittivity for c) ZnO-Ni and d) ZnO-Co_xNi_{1-x}.

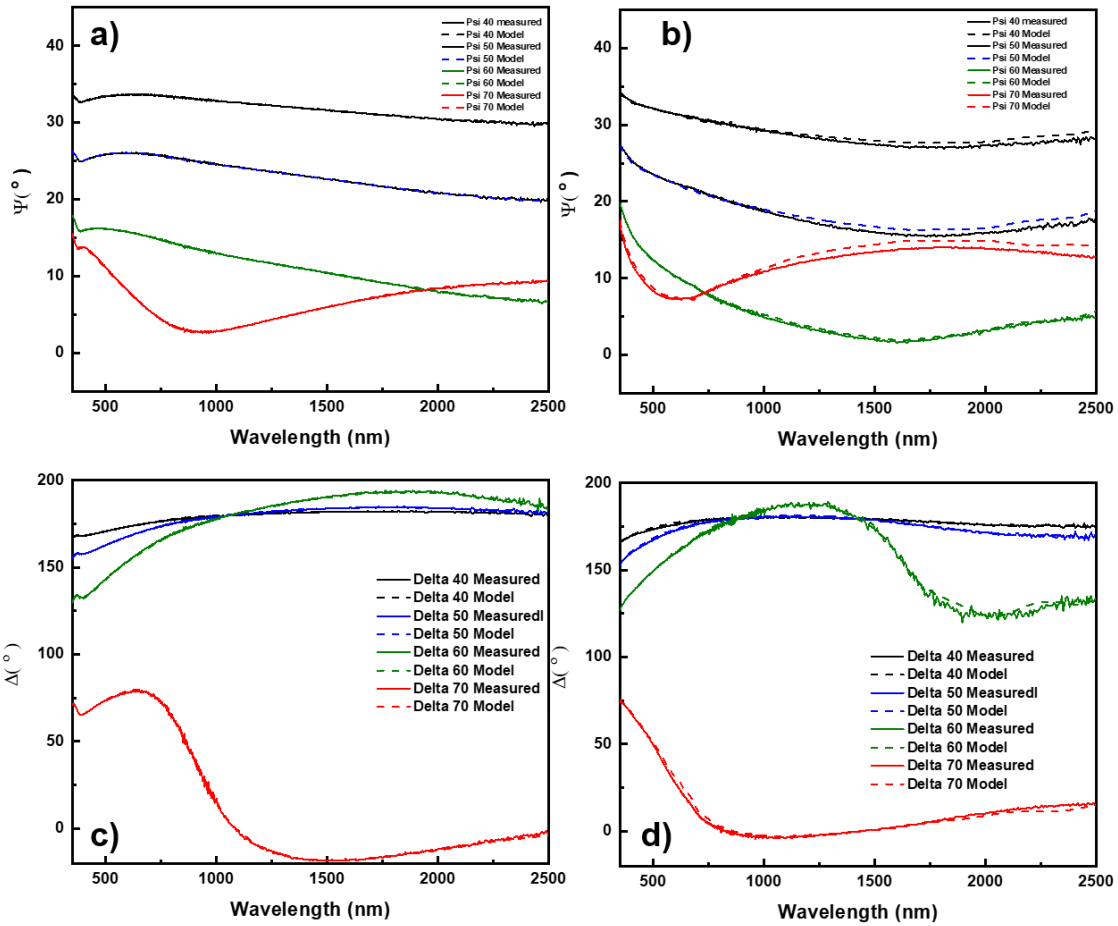

Figure 6.10 Measured and model psi for a) ZnO-Ni and b) ZnO-Co_xNi_{1-x}. Measured and model delta for c) ZnO-Ni and d) ZnO-Co_xNi_{1-x}.

The advantage of the nanocomposites grown in this report are the coupled and tunable ferromagnetic, piezoelectric, and hyperbolic functionalities. The previous device structure of Ni-$LiNbO_3$ [260] is limited in directionality due to the layered morphology. The nanocomposites in this report, due to the anisotropic morphology and properties of the ferromagnetic pillars embedded in the piezoelectric ZnO, maybe able to drive magnetoacoustic waves through the magnetoelastic effect in three dimensions by incorporation of a bottom electrode in a device architecture. Due to the hyperbolic optical response coupled with the magnetoacoustic wave generations, the ZnO-based ferromagnetic VAN may be able to realize devices that can drive both phononic and photonic transmissions. Future work could be in including other

ferromagnetic metals like Fe and the alloys with Ni and Co, as well as other and stronger piezoelectric matrix like $LiNbO_3$. Moreover, future work will be towards device integration and magnetoacoustic wave generation in the piezoelectric/ferromagnetic VAN systems.

6.5 Conclusions

In this work, ferromagnetic metal pillars of Ni, Co, and their nanoalloy were grown in ZnO dielectric matrix. Oxidation was detected in both the ZnO-Ni and ZnO-Co system, with ZnO-Co forming a ZnO-CoO oxide-oxide vertically aligned-nanocomposite. The ZnO-Co_xNi_{1-x} VAN resulted in a morphology of Ni-rich and Co-rich inclusions embedded into ZnO. Magnetic measurements demonstrated anisotropic ferromagnetic properties in both ZnO-Ni and ZnO-Co_xNi_{1-x} samples. The ZnO-Co_xNi_{1-x} also demonstrated an exchange bias effect at low temperatures. The ZnO-Co sample grown at 700^{o}C displayed ferromagnetic properties that may be the result of Co nanoparticles precipitating in the matrix due to the high temperature growth. Optical measurements were performed on ZnO-Ni and ZnO-Co_xNi_{1-x} samples, and both were shown to have a hyperbolic dielectric response. The composites grown in this report due to their combined ferromagnetic and optical response are imagined in magneto-optic applications. Moreover, due to the piezoelectric properties of ZnO, they could be to build devices that rely on a magnetoelastic effect, e.g. the tunability of magnetic field in response to a mechanical force or vice versa. Future work will be in tuning the morphology and towards future device application.

7. CONCLUSION AND FUTURE WORK

In this thesis work, self-assembled oxide-metal vertically-aligned nanocomposites were grown through the pulsed laser deposition in ZnO-based matrix. Specifically, noble metal Au, Ag, and their nanoalloy Ag_xAu_{1-x} along with Ni, Co, and Co_xNi_{1-x}. The ZnO-Au VAN demonstrated through the unique cubic/hexagonal epitaxy an interesting quasi-hexagonal spontaneous in-plane ordering that, along with morphology and properties, was tunable through the deposition parameters including background pressure and laser frequency. ZnO-Au also possessed a strong plasmonic resonance in the visible regime and a complex anisotropic dielectric function portraying hyperbolic dispersion. Due to the Au incorporation in the ZnO-Au hyperbolic metamaterial, absorption losses are high due to joule heating. To overcome this and the particle in-matrix formation of ZnO-Ag nanocomposite, an alloy approach was explored. ZnO-Ag_xAu_{1-x} was the first demonstration of an oxide-nanoalloy VAN. The optical properties were improved over the ZnO-Au and ZnO-Ag single phase composites including stronger plasmonic-coupling and lower absorption losses in the hyperbolic dielectric function. Tunability of the ZnO-Ag_xAu_{1-x} VAN was explored through the background pressure with an effective result on both morphology and optical properties. The morphology was varied from vertically-aligned pillars at low pressure depositions to lateral irregular pillars at high pressure depositions. Moreover, the optical properties were highly varied with respect to the background pressure including the plasmonic resonance and the hyperbolic dispersion. In the last part of this thesis work, new ferromagnetic-piezoelectric ZnO-based nanocomposites were explored for combined photonic and phononic integration. ZnO was combined with Ni, Co, and Co_xNi_{1-x} with both anisotropic optical and ferromagnetic properties.

The nanocomposites developed in this work are mainly for application in optical metamaterial devices with the fourth chapter exploring multifunctional application of optical, magnetic, and acoustical. The future direction of the work in this thesis will be towards different heterostructure and device integrations. For example, coupling the ZnO-ferromagnetic and ZnO-Au VAN into a multilayer optical and magnetic device heterostructure. Another avenue could be in coupling the ZnO-Au VAN with graphene to explore tunable and reconfigurable meta-surfaces in 2D materials. As well, Si-integration of the nanocomposites grown in this thesis

could be investigated for device integration. ZnO is well-known as a component in gas-sensors and for catalysts, and due to the plasmonic metal incorporation, the nanocomposites reported here could be used for sensing and energy-harvesting application.

REFERENCES

1. L. Schmidt-Mende and J. L. MacManus-Driscoll, "ZnO - nanostructures, defects, and devices," Mater. Today **10**, 40–48 (2007).
2. H. Khassaf, N. Khakpash, F. Sun, N. M. Sbrockey, G. S. Tompa, T. S. Kalkur, and S. P. Alpay, "Strain engineered barium strontium titanate for tunable thin film resonators," Appl. Phys. Lett. **104**, (2014).
3. C. Paillard, S. Prokhorenko, and L. Bellaiche, "Strain engineering of electro-optic constants in ferroelectric materials," npj Comput. Mater. **5**, 1–5 (2019).
4. E. J. J. Martin, M. Yan, M. Lane, J. Ireland, C. R. Kannewurf, and R. P. H. Chang, "Properties of multilayer transparent conducting oxide films," Thin Solid Films **461**, 309–315 (2004).
5. M. Finazzi, L. Duò, and F. Ciccacci, "Magnetic properties of interfaces and multilayers based on thin antiferromagnetic oxide films," Surf. Sci. Rep. **64**, 139–167 (2009).
6. A. Bhattacharyya and D. Maurice, "On the evolution of stresses due to lattice misfit at a Ni-superalloy and YSZ interface," Surfaces and Interfaces **12**, 86–94 (2018).
7. A. Stadler, "Transparent Conducting Oxides—An Up-To-Date Overview," Materials (Basel). **5**, 661–683 (2012).
8. Y. Xia, P. Wang, S. Shi, M. Zhang, G. He, J. Lv, and Z. Sun, "Deposition and characterization of AZO thin films on flexible glass substrates using DC magnetron sputtering technique," Ceram. Int. **43**, 4536–4544 (2017).
9. Y. Arimoto and H. Ishiwara, "Current status of ferroelectric random-access memory," MRS Bull. **29**, (2004).
10. H. R. Huff and D. C. Gilmer, *High Dielectric Constant Materials: VLSI MOSFET Applications* (2005).
11. J. Watson, "The tin oxide gas sensor and its applications," Sensors and Actuators **5**, 29–42 (1984).
12. T. Graf, G. Triscone, and J. Muller, "Variation of the superconducting and crystallographic properties and their relation to oxygen stoichiometry of highly homogeneous YBa2Cu3Ox," J. Less-Common Met. **159**, 349–361 (1990).

13. T. Chatterji and P. J. Brown, "Field dependence of the magnetic structure of TbMn2O5," J. Appl. Phys. **116**, (2014).
14. T. Aoyama, K. Yamauchi, A. Iyama, S. Picozzi, K. Shimizu, and T. Kimura, "Giant spin-driven ferroelectric polarization in TbMnO3 under high pressure," Nat. Commun. **5**, 4–10 (2014).
15. M. Čebela, D. Zagorac, K. Batalović, J. Radaković, B. Stojadinović, V. Spasojević, and R. Hercigonja, "BiFeO3 perovskites: A multidisciplinary approach to multiferroics," Ceram. Int. **43**, 1256–1264 (2017).
16. F. Sun, D. Chen, X. Gao, and J. M. Liu, "Emergent strain engineering of multiferroic BiFeO3 thin films," J. Mater. **7**, 281–294 (2021).
17. P. E. Janolin, A. S. Anokhin, Z. Gui, V. M. Mukhortov, Y. I. Golovko, N. Guiblin, S. Ravy, M. El Marssi, Y. I. Yuzyuk, L. Bellaiche, and B. Dkhil, "Strain engineering of perovskite thin films using a single substrate," J. Phys. Condens. Matter **26**, (2014).
18. J. A. Thornton, "The microstructure of sputter-deposited coatings," J. Vac. Sci. Technol. A Vacuum, Surfaces, Film. **4**, 3059–3065 (1986).
19. A. Brewer, K. H. Cho, W. Saenrang, S. H. Baek, J. C. Frederick, and C. B. Eom, "Uniform sputter deposition of high-quality epitaxial complex oxide thin films," J. Vac. Sci. Technol. A Vacuum, Surfaces, Film. **35**, 060607 (2017).
20. H. C. Le, D. E. Zeitoun, J. D. Parisse, M. Sentis, and W. Marine, "Modeling of gas dynamics for a laser-generated plasma: Propagation into low-pressure gases," Phys. Rev. E - Stat. Physics, Plasmas, Fluids, Relat. Interdiscip. Top. **62**, 4152–4161 (2000).
21. T. E. Itina, J. Hermann, P. Delaporte, and M. Sentis, "Laser-generated plasma plume expansion: Combined continuous-microscopic modeling," Phys. Rev. E - Stat. Physics, Plasmas, Fluids, Relat. Interdiscip. Top. **66**, 12 (2002).
22. R. Dittmann, *Stoichiometry in Epitaxial Oxide Thin Films* (2015).
23. R. Eason, *Pulsed Laser Deposition of Thin Films* (2007).
24. S. State and S. C. Unit, "Epitaxial oxide thin films by pulsed laser deposition : Retrospect and prospect," Energy **113**, 445–458 (2001).
25. P. Molian, B. Pecholt, and S. Gupta, "Picosecond pulsed laser ablation and micromachining of 4H-SiC wafers," Appl. Surf. Sci. **255**, 4515–4520 (2009).

26. P. Balling and J. Schou, "Femtosecond-laser ablation dynamics of dielectrics: Basics and applications for thin films," Reports Prog. Phys. **76**, (2013).
27. V. Bhosle and J. Narayan, "Microstructure and electrical property correlations in Ga:ZnO transparent conducting thin films," J. Appl. Phys. **100**, (2006).
28. V. Craciun, J. Elders, J. G. E. Gardeniers, and I. W. Boyd, "Characteristics of high quality ZnO thin films deposited by pulsed laser deposition," Appl. Phys. Lett. **65**, 2963–2965 (1994).
29. L. Guan, D. Zhang, X. Li, and Z. Li, "Role of pulse repetition rate in film growth of pulsed laser deposition," Nucl. Instruments Methods Phys. Res. Sect. B Beam Interact. with Mater. Atoms **266**, 57–62 (2008).
30. A. Sambri, S. Amoruso, X. Wang, F. M. Granozio, and R. Bruzzese, "Plume propagation dynamics of complex oxides in oxygen," J. Appl. Phys. **104**, (2008).
31. T. Ohnishi, M. Lippmaa, T. Yamamoto, S. Meguro, and H. Koinuma, "Improved stoichiometry and misfit control in perovskite thin film formation at a critical fluence by pulsed laser deposition," Appl. Phys. Lett. **87**, 1–3 (2005).
32. M. S. Tillack, D. W. Blair, and S. S. Harilal, "The effect of ionization on cluster formation in laser ablation plumes," Nanotechnology **15**, 390–403 (2004).
33. A. V. Bulgakov and N. M. Bulgakova, "Dynamics of laser-induced plume expansion into an ambient gas during film deposition," J. Phys. D. Appl. Phys. **28**, 1710–1718 (1995).
34. D. R. Crosley, "Laser-induced fluorescence in spectroscopy, dynamics, and diagnostics," J. Chem. Educ. **59**, 446 (1982).
35. F. Claeyssens, A. Cheesman, S. J. Henley, and M. N. R. Ashfold, "Studies of the plume accompanying pulsed ultraviolet laser ablation of zinc oxide," J. Appl. Phys. **92**, 6886–6894 (2002).
36. S. Amoruso, A. Sambri, and X. Wang, "Propagation dynamics of a LaMnO3 laser ablation plume in an oxygen atmosphere," J. Appl. Phys. **100**, 013302 (2006).
37. T. E. Itina, A. A. Katassonov, W. Marine, and M. Autric, "Numerical study of the role of a background gas and system geometry in pulsed laser deposition," J. Appl. Phys. **83**, 6050–6054 (1998).
38. N. Arnold, J. Gruber, and J. Heitz, "Spherical expansion of the vapor plume into ambient gas: An analytical model," Appl. Phys. A Mater. Sci. Process. **69**, 87–93 (1999).

39. A. V. Bulgakov and N. M. Bulgakova, "Gas-dynamic effects of the interaction between a pulsed laser-ablation plume and the ambient gas: Analogy with an underexpanded jet," J. Phys. D. Appl. Phys. **31**, 693–703 (1998).
40. P. Delaporte, M. Sentis, and T. E. Itina, "Laser-generated plasma plume expansion : Combined continuous-microscopic modeling," 1–12 (2002).
41. S. Amoruso, B. Toftmann, and J. Schou, "Thermalization of a UV laser ablation plume in a background gas: From a directed to a diffusionlike flow," Phys. Rev. E - Stat. Physics, Plasmas, Fluids, Relat. Interdiscip. Top. **69**, 6 (2004).
42. M. R. Predtechensky and A. P. Mayorov, "Expansion of Laser-Plasma in Oxygen At Laser Deposition of Htsc Films - Theoretical-Model," Appl. Supercond. **1**, 2011–2017 (1993).
43. A. Sambri, C. Aruta, E. Di Gennaro, X. Wang, U. Scotti Di Uccio, F. Miletto Granozio, and S. Amoruso, "Effects of oxygen background pressure on the stoichiometry of a LaGaO3laser ablation plume investigated by time and spectrally resolved two-dimensional imaging," J. Appl. Phys. **119**, (2016).
44. A. Camposeo, F. Cervelli, F. Fuso, M. Allegrini, and E. Arimondo, "Mechanisms for O2 dissociation during pulsed-laser ablation and deposition," Appl. Phys. Lett. **78**, 2402–2404 (2001).
45. C. Dutouquet and J. Hermann, "Laser-induced fluorescence probing during pulsed-laser ablation for three-dimensional number density mapping of plasma species," J. Phys. D. Appl. Phys. **34**, 3356–3363 (2001).
46. A. Sambri, A. Khare, S. Mirabella, E. Di Gennaro, A. Safeen, F. Di Capua, L. Campajola, U. Scotti Di Uccio, S. Amoruso, and F. Miletto Granozio, "Plasma dynamics and cations off-stoichiometry in LaAlO3films grown in high pressures regimes," J. Appl. Phys. **120**, (2016).
47. S. Wicklein, A. Sambri, S. Amoruso, X. Wang, R. Bruzzese, A. Koehl, and R. Dittmann, "Pulsed laser ablation of complex oxides: The role of congruent ablation and preferential scattering for the film stoichiometry," Appl. Phys. Lett. **101**, (2012).
48. F. Di Fonzo, D. T. A. Li, B. C. S. Casari, M. G. B. C. E. Bottani, D. G. P. Vena, and R. Contro, "Growth regimes in pulsed laser deposition of aluminum oxide films," 765–769 (2008).

49. A. Infortuna, A. S. Harvey, and L. J. Gauckler, "Microstructures of CGO and YSZ thin films by pulsed laser deposition," Adv. Funct. Mater. **18**, 127–135 (2008).
50. J. H. Lee, C.-Y. Chou, Z. Bi, C.-F. Tsai, and H. Wang, "Growth-controlled surface roughness in Al-doped ZnO as transparent conducting oxide.," Nanotechnology **20**, 395704 (2009).
51. S. Heiroth, T. Lippert, A. Wokaun, M. Döbeli, J. L. M. Rupp, B. Scherrer, and L. J. Gauckler, "Yttria-stabilized zirconia thin films by pulsed laser deposition: Microstructural and compositional control," J. Eur. Ceram. Soc. **30**, 489–495 (2010).
52. D. Martoccia and B. D. Patterson, "Energetic Surface Smoothing of Complex Metal-Oxide Thin Films," **176102**, 2–5 (2006).
53. T. Karabacak, "Thin-film growth dynamics with shadowing and re-emission effects," (2018).
54. P. M. Ossi and A. Bailini, "Cluster growth in an ablation plume propagating through a buffer gas," Appl. Phys. A Mater. Sci. Process. **93**, 645–650 (2008).
55. A. Bailini, P. M. Ossi, and A. Rivolta, "Plume propagation through a buffer gas and cluster size prediction," Appl. Surf. Sci. **253**, 7682–7685 (2007).
56. C. Aruta, S. Amoruso, R. Bruzzese, X. Wang, D. Maccariello, F. Miletto Granozio, and U. Scotti di Uccio, "Pulsed laser deposition of SrTiO3/LaGaO3 and SrTiO3/LaAlO3: Plasma plume effects," Appl. Phys. Lett. **97**, 252105 (2010).
57. A. Sarangan, *Nanofabrication* (2016).
58. W. A. Doolittle, A. G. Carver, and W. Henderson, "Molecular beam epitaxy of complex metal-oxides: Where have we come, where are we going, and how are we going to get there?," J. Vac. Sci. Technol. B Microelectron. Nanom. Struct. **23**, 1272 (2005).
59. M. Hata, T. Isu, A. Watanabe, Y. Kajikawa, and Y. Katayama, "Surface diffusion and sticking coefficient of adatoms to atomic steps during molecular beam epitaxy growth," J. Cryst. Growth **114**, 203–208 (1991).
60. F. Baiutti, F. Wrobel, G. Christiani, and G. Logvenov, *Oxide Molecular Beam Epitaxy of Complex Oxide Heterointerfaces* (Elsevier Inc., 2018).
61. J. Zhuang, Q. Sun, Y. Zhou, S. Han, L. Zhou, Y. Yan, H. Peng, S. Venkatesh, W. Wu, R. K. Y. Li, and V. A. L. Roy, "Solution-Processed Rare-Earth Oxide Thin Films for Alternative Gate Dielectric Application," (2016).

62. R. Somoghi, V. Purcar, E. Alexandrescu, I. C. Gifu, C. M. Ninciuleanu, C. M. Cotrut, F. Oancea, and H. Stroescu, "Synthesis of zinc oxide nanomaterials via sol-gel process with anti-corrosive effect for cu, al and zn metallic substrates," Coatings **11**, 1–15 (2021).
63. A. Mitra and G. De, "Sol-Gel Synthesis of Metal Nanoparticle Incorporated Oxide Films on Glass," Glas. Nanocomposites Synth. Prop. Appl. 145–163 (2016).
64. S. Olyaee and A. Naraghi, *Recent Progress in Therapeutic Diagnosis Using Photonic Crystal Nanostructure* (Elsevier Inc., 2017).
65. R. Liu, A. A. Vertegel, E. W. Bohannan, T. A. Sorenson, and J. A. Switzer, "Epitaxial electrodeposition of zinc oxide nanopillars on single-crystal gold," Chem. Mater. **13**, 508–512 (2001).
66. İ. Yılmaz, A. Gelir, O. Yargi, U. Sahinturk, and O. K. Ozdemir, "Electrodeposition of zinc and reduced graphene oxide on porous nickel electrodes for high performance supercapacitors," J. Phys. Chem. Solids **138**, 3–8 (2020).
67. R. Saidi, F. Ashrafizadeh, K. Raeissi, and M. Kharaziha, "Electrochemical aspects of zinc oxide electrodeposition on Ti6Al4V alloy," Surf. Coatings Technol. **402**, (2020).
68. A. Janotti and C. G. Van De Walle, "Fundamentals of zinc oxide as a semiconductor," Reports Prog. Phys. **72**, (2009).
69. H. Morkoc and U. Ozgur, *General Properties of ZnO* (2009).
70. V. Srikant and D. R. Clarke, "On the optical band gap of zinc oxide," J. Appl. Phys. **83**, 5447–5451 (1998).
71. A. Janotti and C. G. Van De Walle, "Fundamentals of zinc oxide as a semiconductor," Reports Prog. Phys. **72**, (2009).
72. R. Vittal and K. C. Ho, "Zinc oxide based dye-sensitized solar cells: A review," Renew. Sustain. Energy Rev. **70**, 920–935 (2017).
73. A. Mang, K. Reimann, and S. Rübenacke, "Band gaps, crystal-field splitting, spin-orbit coupling, and exciton binding energies in ZnO under hydrostatic pressure," Solid State Commun. **94**, 251–254 (1995).
74. C. Wöll, "The chemistry and physics of zinc oxide surfaces," Prog. Surf. Sci. **82**, 55–120 (2007).
75. L. Schmidt-Mende and J. L. MacManus-Driscoll, "ZnO - nanostructures, defects, and devices," Mater. Today **10**, 40–48 (2007).

76. J. Han, P. Q. Mantas, and A. M. R. Senos, "Defect chemistry and electrical characteristics of undoped and Mn-doped ZnO," J. Eur. Ceram. Soc. **22**, 49–59 (2002).
77. M. A. Myers, J. H. Lee, Z. Bi, and H. Wang, "High quality p-type Ag-doped ZnO thin films achieved under elevated growth temperatures," J. Phys. Condens. Matter **24**, (2012).
78. J. C. Fan, K. M. Sreekanth, Z. Xie, S. L. Chang, and K. V Rao, "Progress in Materials Science p-Type ZnO materials : Theory , growth , properties and devices," Prog. Mater. Sci. **58**, 874–985 (2013).
79. L. Deposition, T. Yoshida, and Y. Fukami, "Oxygen Pressure Dependences of Structure and Properties of ZnO Films Deposited on Amorphous Glass Substrates by Pulsed Laser Deposition," (2008).
80. A. Kim, Y. Won, K. Woo, C. H. Kim, and J. Moon, "Highly transparent low resistance ZnO/Ag nanowire/ZnO composite electrode for thin film solar cells," ACS Nano **7**, 1081–1091 (2013).
81. M. K. Pathirane, H. H. Khaligh, I. A. Goldthorpe, and W. S. Wong, "Al-doped ZnO/Ag-nanowire Composite Electrodes for Flexible 3-Dimensional Nanowire Solar Cells," Sci. Rep. **7**, 1–7 (2017).
82. C. Liu, F. He, N. Yan, S. Zang, Y. Zuo, and J. Ma, "Influence of deposition pressure on properties of ZnO: Al films fabricated by RF magnetron sputtering," J. Wuhan Univ. Technol. Mater. Sci. Ed. **31**, 1235–1239 (2016).
83. R. Kumar, O. Al-Dossary, G. Kumar, and A. Umar, "Zinc oxide nanostructures for no2 gas–sensor applications: A review," Nano-Micro Lett. **7**, 97–120 (2015).
84. M. L. M. Napi, S. M. Sultan, R. Ismail, K. W. How, and M. K. Ahmad, "Electrochemical-based biosensors on different zinc oxide nanostructures: A review," Materials (Basel). **12**, 1–34 (2019).
85. A. Tsukazaki, A. Ohtomo, T. Onuma, M. Ohtani, T. Makino, M. Sumiya, K. Ohtani, S. F. Chichibu, S. Fuke, Y. Segawa, H. Ohno, H. Koinuma, and M. Kawasaki, "Repeated temperature modulation epitaxy for p-type doping and light-emitting diode based on ZnO," Nat. Mater. **4**, 42–45 (2005).
86. S. H. Jeong and E. S. Aydil, "Heteroepitaxial growth of Cu2O thin film on ZnO by metal organic chemical vapor deposition," J. Cryst. Growth **311**, 4188–4192 (2009).

87. Y. Nishi, T. Miyata, and T. Minami, "The impact of heterojunction formation temperature on obtainable conversion efficiency in n-ZnO/p-Cu2O solar cells," Thin Solid Films **528**, 72–76 (2013).
88. H. D. Jabbar, M. A. Fakhri, and M. Jalal Abdulrazzaq, "Gallium Nitride -Based Photodiode: A review," Mater. Today Proc. **42**, 2829–2834 (2021).
89. Ü. Özgür, Y. I. Alivov, C. Liu, A. Teke, M. A. Reshchikov, S. Doğan, V. Avrutin, S. J. Cho, and H. Morkǫ, "A comprehensive review of ZnO materials and devices," J. Appl. Phys. **98**, 1–103 (2005).
90. K. Liu, M. Sakurai, and M. Aono, "ZnO-based ultraviolet photodetectors," Sensors **10**, 8604–8634 (2010).
91. H. Y. Liu and G. J. Liu, "Investigation of Bandgap Engineering of Gallium Zinc Oxide-Based Ultraviolet Photodetector by Mist Atmospheric Pressure Chemical Vapor Deposition," IEEE Trans. Electron Devices **66**, 2256–2262 (2019).
92. E. Gür, H. Asıl, K. Çınar, C. Coşkun, S. Tüzemen, K. Meral, Y. Onganer, and K. Şerifoğlu, "Oxygen effects on radiation hardness of ZnO thin films," J. Vac. Sci. Technol. B Microelectron. Nanom. Struct. **27**, 2232 (2009).
93. J. F. Cordaro, C. E. Shipway, and J. T. Schott, "Radiation hardness of zinc oxide varistors," J. Appl. Phys. **61**, 429–431 (1987).
94. H. S. Kaushik, A. Sharma, and M. Sharma, "Dilute Magnetic Semiconductor: A Review of Theoretical Status," Int. J. IT, Eng. Appl. Sci. Res. **3**, 5–10 (2014).
95. S. J. Pearton, C. R. Abernathy, G. T. Thaler, R. Frazier, D. P. Norton, J. Kelly, R. Rairigh, A. F. Hebard, Y. D. Park, and J. M. Zavada, "Wide bandgap materials for semiconductor spintronics," Mater. Res. Soc. Symp. - Proc. **799**, 287–298 (2003).
96. M. Opel, S. T. B. Goennenwein, M. Althammer, K.-W. Nielsen, E.-M. Karrer-Mueller, S. Bauer, K. Senn, C. Schwark, C. Weier, G. Guentherodt, and et al. et al., "Zinc Oxide. From Dilute Magnetic Doping to Spin Transport," ChemInform **46**, no-no (2015).
97. S. K. Nayak, M. Ogura, A. Hucht, S. Buschmann, H. Akai, and P. Entel, "Ab initio simulations of diluted magnetic semiconductors: Cobalt-doped zinc oxide," Phys. Status Solidi Appl. Mater. Sci. **205**, 1839–1846 (2008).
98. R. Seshadri, "Zinc oxide-based diluted magnetic semiconductors," Curr. Opin. Solid State Mater. Sci. **9**, 1–7 (2005).

99. H. Guo, W. A. Saidi, and J. Zhao, "Tunability of the two-dimensional electron gas at the LaAlO3/SrTiO3 interface by strain-induced ferroelectricity," Phys. Chem. Chem. Phys. **18**, 28474–28484 (2016).

100. ţefan Neatu, J. A. Maciá-Agullò, P. Concepciòn, and H. Garcia, "Gold-copper nanoalloys supported on TiO2 as photocatalysts for CO2 reduction by water," J. Am. Chem. Soc. **136**, 15969–15976 (2014).

101. A. Ayati, A. Ahmadpour, F. F. Bamoharram, B. Tanhaei, M. Mänttäri, and M. Sillanpää, "A review on catalytic applications of Au/TiO2 nanoparticles in the removal of water pollutant," Chemosphere **107**, 163–174 (2014).

102. F. Zhou, Q. Wang, and W. Liu, "Au@ZnO nanostructures on porous silicon for photocatalysis and gas-sensing: The effect of plasmonic hot-electrons driven by visiblelight," Mater. Res. Express **3**, (2016).

103. T. Tumkur, Y. Barnakov, S. T. Kee, M. A. Noginov, and V. Liberman, "Permittivity evaluation of multilayered hyperbolic metamaterials: Ellipsometry vs. Reflectometry," J. Appl. Phys. **117**, (2015).

104. J. Huang, J. L. MacManus-Driscoll, and H. Wang, "New epitaxy paradigm in epitaxial self-assembled oxide vertically aligned nanocomposite thin films," J. Mater. Res. **32**, 4054–4066 (2017).

105. X. Sun, J. Huang, J. Jian, M. Fan, H. Wang, Q. Li, J. L. Mac Manus-Driscoll, P. Lu, X. Zhang, and H. Wang, "Three-dimensional strain engineering in epitaxial vertically aligned nanocomposite thin films with tunable magnetotransport properties," Mater. Horizons **5**, 536–544 (2018).

106. W. Zhang, A. Chen, Z. Bi, Q. Jia, J. L. Macmanus-driscoll, and H. Wang, "Interfacial coupling in heteroepitaxial vertically aligned nanocomposite thin films : From lateral to vertical control," Curr. Opin. Solid State Mater. Sci. **18**, 6–18 (2014).

107. A. Chen, Z. Bi, Q. Jia, J. L. Macmanus-Driscoll, and H. Wang, "Microstructure, vertical strain control and tunable functionalities in self-assembled, vertically aligned nanocomposite thin films," Acta Mater. **61**, 2783–2792 (2013).

108. J. Huang, X. Wang, N. L. Hogan, S. Wu, P. Lu, Z. Fan, Y. Dai, B. Zeng, R. Starko-Bowes, J. Jian, H. Wang, L. Li, R. P. Prasankumar, D. Yarotski, M. Sheldon, H. T. Chen, Z. Jacob, X. Zhang, and H. Wang, "Nanoscale Artificial Plasmonic Lattice in Self-Assembled Vertically Aligned Nitride–Metal Hybrid Metamaterials," Adv. Sci. **5**, (2018).
109. J. Huang, W. Li, H. Yang, and J. L. MacManus-Driscoll, "Tailoring physical functionalities of complex oxides by vertically aligned nanocomposite thin-film design," MRS Bull. **46**, 159–167 (2021).
110. J. L. M. A. C. Manus-driscoll, P. Zerrer, H. Wang, H. A. O. Yang, J. Yoon, A. Fouchet, R. Yu, M. G. Blamire, and Q. Jia, "Strain control and spontaneous phase ordering in vertical nanocomposite heteroepitaxial thin films," **7**, (2008).
111. X. Sun, Q. Li, J. Huang, J. Jian, P. Lu, X. Zhang, J. L. Macmanus-Driscoll, and H. Wang, "Strain and property tuning of the 3D framed epitaxial nanocomposite thin films via interlayer thickness variation," J. Appl. Phys. **125**, 1–10 (2019).
112. V. Schuler, F. J. Bonilla, D. Demaille, A. Coati, A. Vlad, Y. Garreau, M. Sauvage-Simkin, A. Novikova, E. Fonda, S. Hidki, V. Etgens, F. Vidal, and Y. Zheng, "Huge metastable axial strain in ultrathin heteroepitaxial vertically aligned nanowires," Nano Res. **8**, 1964–1974 (2015).
113. Z. Bi, E. Weal, H. Luo, A. Chen, J. L. MacManus-Driscoll, Q. Jia, and H. Wang, " Microstructural and magnetic properties of (La 0.7 Sr 0.3 MnO 3) 0.7 :(Mn 3 O 4) 0.3 nanocomposite thin films ," J. Appl. Phys. **109**, 054302 (2011).
114. M. Fan, H. Wang, S. Misra, B. Zhang, Z. Qi, X. Sun, J. Huang, and H. Wang, "Microstructure, Magnetic, and Magnetoresistance Properties of La0.7Sr0.3MnO3:CuO Nanocomposite Thin Films," ACS Appl. Mater. Interfaces **10**, 5779–5784 (2018).
115. X. Gao, L. Li, J. Jian, H. Wang, M. Fan, J. Huang, X. Wang, and H. Wang, " Vertically Aligned Nanocomposite BaTiO 3 :YMnO 3 Thin Films with Room Temperature Multiferroic Properties toward Nanoscale Memory Devices ," ACS Appl. Nano Mater. **1**, 2509–2514 (2018).
116. A. Chen, Z. Bi, Q. Jia, J. L. Macmanus-driscoll, and H. Wang, "Microstructure , vertical strain control and tunable functionalities in self-assembled , vertically aligned nanocomposite thin films q," Acta Mater. **61**, 2783–2792 (2013).

117. J. L. MacManus-Driscoll, A. Suwardi, and H. Wang, "Composite epitaxial thin films: A new platform for tuning, probing, and exploiting mesoscale oxides," MRS Bull. **40**, 933–942 (2015).
118. R. O. Prum, T. Quinn, and R. H. Torres, "Anatomically diverse butterfly scales all produce structural colours by coherent scattering," J. Exp. Biol. **209**, 748–765 (2006).
119. J. Teyssier, S. V. Saenko, D. Van Der Marel, and M. C. Milinkovitch, "Photonic crystals cause active colour change in chameleons," Nat. Commun. **6**, 1–7 (2015).
120. R. L. Morrison, W. C. Sherbrooke, and S. K. Frost-mason, "Temperature-Sensitive , Physiologically Active Iridophores in the Lizard Urosaurus ornatus : An Ultrastructural Analysis of Color Change Published by : American Society of Ichthyologists and Herpetologists Temperature-Sensitive , Physiologically Active Ir," Society **1996**, 804–812 (2010).
121. R. A. Ligon and K. J. McGraw, "Chameleons communicate with complex colour changes during contests: Different body regions convey different information," Biol. Lett. **9**, (2013).
122. X. Sun, J. L. MacManus-Driscoll, and H. Wang, "Spontaneous Ordering of Oxide-Oxide Epitaxial Vertically Aligned Nanocomposite Thin Films," Annu. Rev. Mater. Res. **50**, 229–253 (2020).
123. M. Fan, B. Zhang, H. Wang, J. Jian, X. Sun, J. Huang, L. Li, X. Zhang, and H. Wang, "Self-Organized Epitaxial Vertically Aligned Nanocomposites with Long-Range Ordering Enabled by Substrate Nanotemplating," Adv. Mater. **29**, 1–7 (2017).
124. L. Yan, Z. Wang, Z. Xing, J. Li, and D. Viehland, "Magnetoelectric and multiferroic properties of variously oriented epitaxial BiFeO3 - CoFe2 O4 nanostructured thin films," J. Appl. Phys. **107**, 1–6 (2010).
125. N. Dix, R. Muralidharan, J. Guyonnet, B. Warot-Fonrose, M. Varela, P. Paruch, F. Sánchez, and J. Fontcuberta, "On the strain coupling across vertical interfaces of switchable BiFeO 3 - CoFe2 O4 multiferroic nanostructures," Appl. Phys. Lett. **95**, (2009).
126. H. Zheng, F. Straub, Q. Zhan, P. L. Yang, W. K. Hsieh, F. Zavaliche, Y. H. Chu, U. Dahmen, and R. Ramesh, "Self-assembled growth of BiFeO3-CoFe2O4 nanostructures," Adv. Mater. **18**, 2747–2752 (2006).

127. T. Amrillah, A. Hermawan, S. Yin, and J. Y. Juang, "Formation and physical properties of the self-assembled BFO-CFO vertically aligned nanocomposite on a CFO-buffered two-dimensional flexible mica substrate," RSC Adv. **11**, 15539–15545 (2021).
128. H. Zheng, F. Straub, Q. Zhan, P. L. Yang, W. K. Hsieh, F. Zavaliche, Y. H. Chu, U. Dahmen, and R. Ramesh, "Self-assembled growth of BiFeO3-CoFe2O4 nanostructures," Adv. Mater. **18**, 2747–2752 (2006).
129. M. B. S. Hesselberth, S. J. Van Der Molen, and J. Aarts, "The surface structure of SrTiO3 at high temperatures under influence of oxygen," Appl. Phys. Lett. **104**, (2014).
130. Z. Bi, E. Weal, H. Luo, A. Chen, J. L. MacManus-Driscoll, Q. Jia, and H. Wang, "Microstructural and magnetic properties of (La0.7Sr 0.3MnO3)0.7:(Mn3O4) 0.3 nanocomposite thin films," J. Appl. Phys. **109**, 1–7 (2011).
131. Y. Zhu, C. F. Tsai, J. Wang, J. H. Kwon, H. Wang, C. V. Varanasi, J. Burke, L. Brunke, and P. N. Barnes, "Interfacial defects distribution and strain coupling in the vertically aligned nanocomposite YBa 2Cu 3O 7-X/BaSnO 3 thin films," J. Mater. Res. **27**, 1763–1769 (2012).
132. B. J. Yoon, S. Cho, J. Kim, J. Lee, Z. Bi, A. Serquis, X. Zhang, A. Manthiram, and H. Wang, "Vertically Aligned Nanocomposite Thin Films as a Cathode / Electrolyte Interface Layer for Thin-Film Solid Oxide Fuel Cells," **77843**, 3868–3873 (2009).
133. S. Misra, L. Li, X. Gao, J. Jian, Z. Qi, D. Zemlyanov, and H. Wang, "Tunable physical properties in BiAl1-: XMnxO3 thin films with novel layered supercell structures," Nanoscale Adv. **2**, 315–322 (2020).
134. X. Sun, M. Kalaswad, Q. Li, R. L. Paldi, J. Huang, H. Wang, X. Gao, X. Zhang, and H. Wang, "Role of Interlayer in 3D Vertically Aligned Nanocomposite Frameworks with Tunable Magnetotransport Properties," Adv. Mater. Interfaces **7**, 1–7 (2020).
135. W. Li, W. Zhang, L. Wang, J. Gu, A. Chen, R. Zhao, Y. Liang, H. Guo, R. Tang, C. Wang, K. Jin, H. Wang, and H. Yang, "Vertical Interface Induced Dielectric Relaxation in Nanocomposite (BaTiO3)1-x:(Sm2O3)x Thin Films," Sci. Rep. **5**, 1–8 (2015).
136. D. G. Schlom, L. Q. Chen, X. Pan, A. Schmehl, and M. A. Zurbuchen, "A thin film approach to engineering functionality into oxides," J. Am. Ceram. Soc. **91**, 2429–2454 (2008).

137. D. M. Cunha and M. Huijben, "Lithium-based vertically aligned nanocomposites for three-dimensional solid-state batteries," MRS Bull. **46**, 152–158 (2021).
138. X. Wang and H. Wang, "Recent Advances in Vertically Aligned Nanocomposites with Tunable Optical Anisotropy : Fundamentals and Beyond," 1–17 (2021).
139. R. L. Zong, J. Zhou, Q. Li, B. Du, B. Li, M. Fu, X. W. Qi, L. T. Li, and S. Buddhudu, "Synthesis and optical properties of silver nanowire arrays embedded in anodic alumina membrane," J. Phys. Chem. B **108**, 16713–16716 (2004).
140. R. S. T. B. Owes, J. A. Tkinson, W. N. Ewman, T. K. Allos, P. Alikaras, R. F. Edosejevs, S. P. Ramanik, and Z. J. Acob, "Optical Characterization of Epsilon Near Zero, Epsilon Near Pole and Hyperbolic Reponse in Nanowire Metamaterials," J. Opt. Soc. Am. B **32**, 2074–2080 (2015).
141. J. Yao, Y. Wang, K. T. Tsai, Z. Liu, X. Yin, G. Bartal, A. M. Stacy, Y. L. Wang, and X. Zhang, "Design, fabrication and characterization of indefinite metamaterials of nanowires," Philos. Trans. R. Soc. A Math. Phys. Eng. Sci. **369**, 3434–3446 (2011).
142. Q. Su, W. Zhang, P. Lu, S. Fang, F. Khatkhatay, J. Jian, L. Li, F. Chen, X. Zhang, J. L. Macmanus-Driscoll, A. Chen, Q. Jia, and H. Wang, "Self-Assembled Magnetic Metallic Nanopillars in Ceramic Matrix with Anisotropic Magnetic and Electrical Transport Properties," ACS Appl. Mater. Interfaces **8**, 20283–20291 (2016).
143. L. Li, L. Sun, J. S. Gomez-Diaz, N. L. Hogan, P. Lu, F. Khatkhatay, W. Zhang, J. Jian, J. Huang, Q. Su, M. Fan, C. Jacob, J. Li, X. Zhang, Q. Jia, M. Sheldon, A. Alù, X. Li, and H. Wang, "Self-assembled epitaxial Au-oxide vertically aligned nanocomposites for nanoscale metamaterials," Nano Lett. **16**, 3936–3943 (2016).
144. J. Huang, X. Wang, X. L. Phuah, P. Lu, Z. Qi, and H. Wang, "Plasmonic Cu nanostructures in ZnO as hyperbolic metamaterial thin films," Mater. Today Nano **8**, 100052 (2019).
145. S. Misra, L. Li, J. Jian, J. Huang, X. Wang, D. Zemlyanov, J. Jang, F. H. Ribeiro, and H. Wang, "Tailorable Au nanoparticles embedded in epitaxial TiO2 thin films for tunable optical properties," ACS Appl. Mater. Interfaces **10**, 32895–32902 (2018).
146. R. L. Paldi, Z. Qi, S. Misra, J. Lu, X. Sun, M. Kalaswad, J. Bischoff, D. W. Branch, A. Siddiqui, and H. Wang, "Nanocomposite-seeded epitaxial growth of single-domain lithium niobate thin films for surface acoustic wave devices," (2020).

147. J. Mertens, M. E. Kleemann, R. Chikkaraddy, P. Narang, and J. J. Baumberg, "How Light Is Emitted by Plasmonic Metals," Nano Lett. **17**, 2568–2574 (2017).
148. J. M. McMahon, G. C. Schatz, and S. K. Gray, "Plasmonics in the ultraviolet with the poor metals Al, Ga, In, Sn, Tl, Pb, and Bi," Phys. Chem. Chem. Phys. **15**, 5415–5423 (2013).
149. J. Feng, V. S. Siu, A. Roelke, V. Mehta, S. Y. Rhieu, G. T. R. Palmore, and D. Pacifici, "Nanoscale plasmonic interferometers for multispectral, high-throughput biochemical sensing," Nano Lett. **12**, 602–609 (2012).
150. R. Yan, P. Pausauskie, J. Huang, and P. Yang, "Direct photonic–plasmonic coupling and routing in single nanowires," Proc. Natl. Acad. Sci. **106**, 21045–21050 (2009).
151. W. L. Barnes, A. Dereux, and T. W. Ebbesen, "Surface plasmon subwavelength optics," Nature **424**, 824–830 (2003).
152. S. Mubeen, J. Lee, W. R. Lee, N. Singh, G. D. Stucky, and M. Moskovits, "On the plasmonic photovoltaic," ACS Nano **8**, 6066–6073 (2014).
153. A. V. Kabashin, P. Evans, S. Pastkovsky, W. Hendren, G. A. Wurtz, R. Atkinson, R. Pollard, V. A. Podolskiy, and A. V. Zayats, "Plasmonic nanorod metamaterials for biosensing," Nat. Mater. **8**, 867–871 (2009).
154. A. Boltasseva and H. A. Atwater, "Low-Loss Plasmonic Metamaterials," Science (80-.). **331**, 290–292 (2011).
155. L. Lu, R. E. Simpson, and S. K. Valiyaveedu, "Active hyperbolic metamaterials: Progress, materials and design," J. Opt. (United Kingdom) **20**, 1–20 (2018).
156. A. N. Grigorenko, M. Polini, and K. S. Novoselov, "Graphene plasmonics," Nat. Photonics **6**, 749–758 (2012).
157. M. Achermann, "Exciton-plasmon interactions in metal-semiconductor nanostructures," J. Phys. Chem. Lett. **1**, 2837–2843 (2010).
158. S. Tan, A. Argondizzo, J. Ren, L. Liu, J. Zhao, and H. Petek, "Plasmonic coupling at a metal/semiconductor interface," Nat. Photonics **11**, 806–812 (2017).
159. S. Nie, "Probing Single Molecules and Single Nanoparticles by Surface-Enhanced Raman Scattering," Science (80-.). **275**, 1102–1106 (1997).

160. V. Amendola, S. Scaramuzza, S. Agnoli, S. Polizzi, and M. Meneghetti, "Strong dependence of surface plasmon resonance and surface enhanced Raman scattering on the composition of Au-Fe nanoalloys," Nanoscale **6**, 1423–1433 (2014).
161. C. W. Cheng, E. J. Sie, B. Liu, C. H. A. Huan, T. C. Sum, H. D. Sun, and H. J. Fan, "Surface plasmon enhanced band edge luminescence of ZnO nanorods by capping Au nanoparticles," Appl. Phys. Lett. **96**, 2008–2011 (2010).
162. H. M. Bok, K. L. Shuford, S. G. Kim, S. Kyukim, and S. Park, "Multiple surface plasmon modes for gold/silver alloy nanorods," Langmuir **25**, 5266–5270 (2009).
163. Z. L. Wang and J. M. Cowley, "Size and shape dependence of the surface plasmon frequencies for supported metal particle systems," Ultramicroscopy **23**, 97–107 (1987).
164. B. J. Wiley, S. H. Im, Z. Y. Li, J. McLellan, A. Siekkinen, and Y. Xia, "Maneuvering the surface plasmon resonance of silver nanostructures through shape-controlled synthesis," J. Phys. Chem. B **110**, 15666–15675 (2006).
165. Z. Jacob, L. V. Alekseyev, and E. Narimanov, "Optical Hyperlens: Far-field imaging beyond the diffraction limit," Opt. Express **14**, 8247 (2006).
166. E. E. Narimanov, "Dyakonov waves in biaxial anisotropic crystals," Phys. Rev. A **98**, 1–13 (2018).
167. I. I. Smolyaninov, "Modeling of causality with metamaterials," J. Opt. (United Kingdom) **15**, 1591–1595 (2013).
168. I. I. Smolyaninov, "Analog of gravitational force in hyperbolic metamaterials," Phys. Rev. A - At. Mol. Opt. Phys. **88**, 1–4 (2013).
169. R. Chandrasekar, Z. Wang, X. Meng, A. Lagutchev, Y. L. Kim, A. Wei, A. Boltasseva, and V. M. Shalaev, "Lasing Action in Gold Nanorod Hyperbolic Metamaterials," ACS Photonics **4**, 674–680 (2017).
170. Y. He, S. He, and X. Yang, "Optical field enhancement in nanoscale slot waveguides of hyperbolic metamaterials," Opt. Lett. **37**, 2907–2909 (2012).
171. T. U. Tumkur, J. K. Kitur, B. Chu, L. Gu, V. A. Podolskiy, E. E. Narimanov, and M. A. Noginov, "Control of reflectance and transmittance in scattering and curvilinear hyperbolic metamaterials," Appl. Phys. Lett. **101**, 1–5 (2012).
172. I. I. Smolyaninov, "Quantum topological transition in hyperbolic metamaterials based on high Tc superconductors," J. Phys. Condens. Matter **26**, (2014).

173. V. N. Smolyaninova, C. Jensen, W. Zimmerman, J. C. Prestigiacomo, M. S. Osofsky, H. Kim, N. Bassim, Z. Xing, M. M. Qazilbash, and I. I. Smolyaninov, "Enhanced superconductivity in aluminum-based hyperbolic metamaterials," Sci. Rep. **6**, 1–12 (2016).
174. M. Lu, L. Feng, and Y. Chen, "Phononic crystals and acoustic metamaterials Phononic crystals have been proposed about two decades ago and," Mater. Today **12**, 34–42 (2009).
175. H. Ge, M. Yang, C. Ma, M. H. Lu, Y. F. Chen, N. Fang, and P. Sheng, "Breaking the barriers: Advances in acoustic functional materials," Natl. Sci. Rev. **5**, 159–182 (2018).
176. A. Siddiqui, R. H. Olsson, S. Member, and M. Eichenfield, "Lamb Wave Focusing Transducer for Efficient Coupling to Wavelength-Scale Structures in Thin Piezoelectric Films," **27**, 1054–1070 (2018).
177. P. Shekhar, J. Atkinson, and Z. Jacob, "Hyperbolic metamaterials: fundamentals and applications," Nano Converg. **1**, 1–17 (2014).
178. Z. Guo, H. Jiang, and H. Chen, "Hyperbolic metamaterials: From dispersion manipulation to applications," J. Appl. Phys. **127**, (2020).
179. L. Ferrari, C. Wu, D. Lepage, X. Zhang, and Z. Liu, "Hyperbolic metamaterials and their applications," Prog. Quantum Electron. **40**, 1–40 (2015).
180. T. U. Tumkur, L. Gu, J. K. Kitur, E. E. Narimanov, and M. A. Noginov, "Control of absorption with hyperbolic metamaterials," Appl. Phys. Lett. **100**, 1–4 (2012).
181. A. Poddubny, I. Iorsh, P. Belov, and Y. Kivshar, "Hyperbolic metamaterials," Nat. Photonics **7**, 958–967 (2013).
182. Z. Liu, H. Lee, Y. Xiong, C. Sun, and X. Zhang, "Far-Field Optical Hyperlens Magnifying," **315**, (2007).
183. Z. Jacob, *Quantum Plasmonics* (2012), Vol. 37.
184. H. Gao, X. Zhang, W. Li, and M. Zhao, "Tunable broadband hyperbolic light dispersion in metal diborides," Opt. Express **27**, 36911 (2019).
185. I. I. Smolyaninov, E. Hwang, and E. Narimanov, "Hyperbolic metamaterial interfaces: Hawking radiation from Rindler horizons and spacetime signature transitions," Phys. Rev. B - Condens. Matter Mater. Phys. **85**, 1–7 (2012).
186. J. S. T. Smalley, F. Vallini, X. Zhang, and Y. Fainman, "Dynamically tunable and active hyperbolic metamaterials," Adv. Opt. Photonics **10**, 354 (2018).

187. M. A. Noginov, Y. A. Barnakov, G. Zhu, T. Tumkur, H. Li, and E. E. Narimanov, "Bulk photonic metamaterial with hyperbolic dispersion," Appl. Phys. Lett. **94**, 1–4 (2009).

188. X. Xiang, C. Yang, Y. Zhang, Z. Peng, Z. Cao, H. Zhao, P. Zhang, and L. Xuan, "Experimental realization of hyperbolic dispersion metamaterial for the whole visible spectrum based on liquid crystalline phase soft template," Opt. Express **23**, 21343–21351 (2015).

189. J. D. Caldwell, L. Lindsay, V. Giannini, I. Vurgaftman, T. L. Reinecke, S. A. Maier, and O. J. Glembocki, "Low-loss, infrared and terahertz nanophotonics using surface phonon polaritons," Nanophotonics **4**, 44–68 (2015).

190. G. V. Naik, V. M. Shalaev, and A. Boltasseva, "Alternative plasmonic materials: Beyond gold and silver," Adv. Mater. **25**, 3264–3294 (2013).

191. Y. Gutiérrez, A. S. Brown, F. Moreno, and M. Losurdo, "Plasmonics beyond noble metals: Exploiting phase and compositional changes for manipulating plasmonic performance," J. Appl. Phys. **128**, (2020).

192. Yu Shi and Hong Koo Kim, "Low-loss Plasmonic Metamaterial Waveguides," Proc. 17th IEEE Int. Conf. Nanotechnol. 890–893 (2017).

193. B. J. Inkson, *Scanning Electron Microscopy (SEM) and Transmission Electron Microscopy (TEM) for Materials Characterization* (Elsevier Ltd, 2016).

194. N. Garcia, E. V. Ponizowskaya, H. Zhu, J. Q. Xiao, and A. Pons, "Wide photonic band gaps at the visible in metallic nanowire arrays embedded in a dielectric matrix," Appl. Phys. Lett. **82**, 3147–3149 (2003).

195. N. Garcia, E. V. Ponizovskaya, and J. Q. Xiao, "Zero permittivity materials: Band gaps at the visible," Appl. Phys. Lett. **80**, 1120–1122 (2002).

196. M. Silveirinha and N. Engheta, "Tunneling of electromagnetic energy through subwavelength channels and bends using ε-near-zero materials," Phys. Rev. Lett. **97**, 1–4 (2006).

197. D. C. Adams, S. Inampudi, T. Ribaudo, D. Slocum, S. Vangala, N. A. Kuhta, W. D. Goodhue, V. A. Podolskiy, and D. Wasserman, "Funneling light through a subwavelength aperture with epsilon-near-zero materials," Phys. Rev. Lett. **107**, 1–5 (2011).

198. R. Liu, Q. Cheng, T. Hand, J. J. Mock, T. J. Cui, S. A. Cummer, and D. R. Smith, "Experimental demonstration of electromagnetic tunneling through an epsilon-near-zero metamaterial at microwave frequencies," Phys. Rev. Lett. **100**, 1–4 (2008).
199. J. Hao, W. Yan, and M. Qiu, "Super-reflection and cloaking based on zero index metamaterial," Appl. Phys. Lett. **96**, 1–4 (2010).
200. I. I. Smolyaninov and V. N. Smolyaninova, "Is There a metamaterial route to high temperature superconductivity?," Conf. Lasers Electro-Optics Eur. - Tech. Dig. **2014-Janua**, (2014).
201. I. I. Smolyaninov, B. Yost, E. Bates, and V. N. Smolyaninova, "Experimental demonstration of metamaterial “multiverse” in a ferrofluid," Opt. Express **21**, 14918 (2013).
202. N. A. Melosh, A. Boukai, F. Diana, B. Gerardot, A. Badolato, P. M. Petroff, and J. R. Heath, "Ultrahigh-density nanowire lattices and circuits," Science (80-.). **300**, 112–115 (2003).
203. S. Shukla, K. T. Kim, A. Baev, Y. K. Yoon, N. M. Litchinitser, and P. N. Prasad, "Fabrication and characterization of gold-polymer nanocomposite plasmonic nanoarrays in a porous alumina template," ACS Nano **4**, 2249–2255 (2010).
204. W. J. Stępniowski and M. Salerno, "Fabrication of nanowires and nanotubes by anodic alumina template-assisted electrodeposition," in *Manufacturing Nanostructures* (2014), pp. 321–357.
205. X. Wang, J. Jian, Z. Zhou, C. Fan, Y. Dai, L. Li, J. Huang, J. Sun, A. Donohue, P. Bermel, X. Zhang, H. T. Chen, and H. Wang, "Self-Assembled Ag–TiN Hybrid Plasmonic Metamaterial: Tailorable Tilted Nanopillar and Optical Properties," Adv. Opt. Mater. **7**, 1–9 (2019).
206. X. Sun, Q. Li, J. Huang, M. Fan, B. X. Rutherford, R. L. Paldi, J. Jian, X. Zhang, and H. Wang, "Strain-driven nanodumbbell structure and enhanced physical properties in hybrid vertically aligned nanocomposite thin films," Appl. Mater. Today **16**, 204–212 (2019).
207. J. Huang, L. Li, P. Lu, Z. Qi, X. Sun, X. Zhang, and H. Wang, "Self-assembled Co-BaZrO3 nanocomposite thin films with ultra-fine vertically aligned Co nanopillars," Nanoscale **9**, 7970–7976 (2017).

208. B. Zhang, M. Fan, L. Li, J. Jian, J. Huang, H. Wang, M. Kalaswad, and H. Wang, "Tunable magnetic anisotropy of self-assembled Fe nanostructures within a La0.5Sr0.5FeO3 matrix," Appl. Phys. Lett. **112**, 0–5 (2018).

209. X. Chen, Z. Wu, D. Liu, and Z. Gao, "Preparation of ZnO Photocatalyst for the Efficient and Rapid Photocatalytic Degradation of Azo Dyes," Nanoscale Res. Lett. **12**, 4–13 (2017).

210. M. I. MENDELSON, "Average Grain Size in Polycrystalline Ceramics," J. Am. Ceram. Soc. **52**, 443–446 (1969).

211. B. K. Chakbavebty, "Grain Size Distribution in thin Films," J. Phys. Chem. Solids **28**, 2401–2412 (1967).

212. A. Gaiardo, B. Fabbri, A. Giberti, V. Guidi, P. Bellutti, C. Malagù, and M. Valt, "Sensors and Actuators B : Chemical ZnO and Au / ZnO thin films : Room-temperature chemoresistive properties for gas sensing applications," Sensors Actuators B. Chem. **237**, 1085–1094 (2016).

213. R. Maas, J. Parsons, N. Engheta, and A. Polman, "Experimental realization of an epsilon-near-zero metamaterial at visible wavelengths," Nat. Photonics **7**, 907–912 (2013).

214. R. Starko-Bowes, J. Atkinson, W. Newman, H. Hu, T. Kallos, G. Palikaras, R. Fedosejevs, S. Pramanik, and Z. Jacob, "Optical characterization of epsilon-near-zero, epsilon-near-pole, and hyperbolic response in nanowire metamaterials," J. Opt. Soc. Am. B **32**, 2074–2080 (2015).

215. R. Macêdo, T. Dumelow, and R. L. Stamps, "Tunable Focusing in Natural Hyperbolic Magnetic Media," ACS Photonics **3**, 1670–1677 (2016).

216. B. Wood, J. B. Pendry, and D. P. Tsai, "Directed subwavelength imaging using a layered metal-dielectric system," Phys. Rev. B - Condens. Matter Mater. Phys. **74**, 1–8 (2006).

217. X. Zhang and Z. Liu, "Superlenses to overcome the diffraction limit," Nat. Mater. **7**, 435–441 (2008).

218. M. Wang, M. Ye, J. Iocozzia, C. Lin, and Z. Lin, "Plasmon-mediated solar energy conversion via photocatalysis in noble metal/semiconductor composites," Adv. Sci. **3**, 1–14 (2015).

219. M. Gu, Z. Ouyang, B. Jia, N. Stokes, X. Chen, N. Fahim, X. Li, M. J. Ventura, and Z. Shi, "Nanoplasmonics: A frontier of photovoltaic solar cells," Nanophotonics **1**, 235–248 (2012).

220. N. A. Joy, M. I. Nandasiri, P. H. Rogers, W. Jiang, T. Varga, S. V. N. T. Kuchibhatla, S. Thevuthasan, and M. A. Carpenter, "Selective plasmonic gas sensing: H 2 , NO 2 , and CO spectral discrimination by a single Au-CeO 2 nanocomposite film," Anal. Chem. **84**, 5025–5034 (2012).

221. S. Misra, L. Li, D. Zhang, J. Jian, Z. Qi, M. Fan, H. T. Chen, X. Zhang, and H. Wang, "Self-Assembled Ordered Three-Phase Au–BaTiO 3 –ZnO Vertically Aligned Nanocomposites Achieved by a Templating Method," Adv. Mater. **31**, 1–8 (2019).

222. W. Zhang, A. Chen, J. Jian, Y. Zhu, L. Chen, P. Lu, Q. Jia, J. L. Macmanus-driscoll, X. Zhang, and H. Wang, "Strong perpendicular exchange bias in epitaxial La0.7Sr0.3MnO3:BiFeO3 nanocomposite films through vertical interfacial coupling," Nanoscale 13808–13815 (2015).

223. G. L. Hornyak, C. J. Patrissi, E. B. Oberhauser, C. R. Martin, J. C. Valmalette, L. Lemaire, J. Dutta, and H. Hofmann, "Effective medium theory characterization of Au/Ag nanoalloy-porous alumina composites," Nanostructured Mater. **9**, 571–574 (1997).

224. M. W. Knight, N. S. King, L. Liu, H. O. Everitt, P. Nordlander, and N. J. Halas, "Aluminum for plasmonics," ACS Nano **8**, 834–840 (2014).

225. G. H. Chan, J. Zhao, E. M. Hicks, G. C. Schatz, and R. P. Van Duyne, "Plasmonic properties of copper nanoparticles fabricated by nanosphere lithography," Nano Lett. **7**, 1947–1952 (2007).

226. C. Gao, Y. Hu, M. Wang, M. Chi, and Y. Yin, "Fully alloyed Ag/Au nanospheres: Combining the plasmonic property of Ag with the stability of Au," J. Am. Chem. Soc. **136**, 7474–7479 (2014).

227. N. Alissawi, V. Zaporojtchenko, T. Strunskus, I. Kocabas, V. S. K. Chakravadhanula, L. Kienle, D. Garbe-Schönberg, and F. Faupel, "Effect of gold alloying on stability of silver nanoparticles and control of silver ion release from vapor-deposited Ag-Au/polytetrafluoroethylene nanocomposites," Gold Bull. **46**, 3–11 (2013).

228. D. . Bobb, G. Zhu, M. Mayy, A. V. Gavrilenko, P. Mead, V. I. Gavrilenko, and M. A. Noginov, "Engineering of Low-Loss Metal for Nanoplasmonic and Metamaterials Applications," Appl. Phys. Lett. **95**, 1–15 (2009).

229. H. Fang, J. Yang, M. Wen, and Q. Wu, "Nanoalloy Materials for Chemical Catalysis," Adv. Mater. **30**, 1–10 (2018).

230. B. M. Muñoz-Flores, B. I. Kharisov, V. M. Jiménez-Pérez, P. Elizondo Martínez, and S. T. López, "Recent advances in the synthesis and main applications of metallic nanoalloys," Ind. Eng. Chem. Res. **50**, 7705–7721 (2011).

231. K. E. Lee, A. V. Hesketh, and T. L. Kelly, "Chemical stability and degradation mechanisms of triangular Ag, Ag@Au, and Au nanoprisms," Phys. Chem. Chem. Phys. **16**, 12407–12414 (2014).

232. J. Huang, T. Jin, S. Misra, H. Wang, Z. Qi, Y. Dai, X. Sun, L. Li, J. Okkema, H.-T. Chen, P.-T. Lin, X. Zhang, and H. Wang, "Tailorable Optical Response of Au-LiNbO 3 Hybrid Metamaterial Thin Films for Optical Waveguide Applications," Adv. Opt. Mater. **6**, 1–9 (2018).

233. R. Ferrando, J. Jellinek, and R. L. Johnston, "Nanoalloys: From theory to applications of alloy clusters and nanoparticles," Chem. Rev. **108**, 845–910 (2008).

234. Y. Wu, C. Zhang, N. M. Estakhri, Y. Zhao, J. Kim, M. Zhang, X. X. Liu, G. K. Pribil, A. Alù, C. K. Shih, and X. Li, "Intrinsic optical properties and enhanced plasmonic response of epitaxial silver," Adv. Mater. **26**, 6106–6110 (2014).

235. S. B. Rice, C. Chan, S. C. Brown, P. Eschbach, L. Han, D. S. Ensor, A. B. Stefaniak, J. Bonevich, A. E. Vladár, A. R. H. Walker, J. Zheng, C. Starnes, A. Stromberg, J. Ye, and E. A. Grulke, "Particle size distributions by transmission electron microscopy: An interlaboratory comparison case study," Metrologia **50**, 663–678 (2013).

236. K. S. Lee and M. A. El-Sayed, "Gold and silver nanoparticles in sensing and imaging: Sensitivity of plasmon response to size, shape, and metal composition," J. Phys. Chem. B **110**, 19220–19225 (2006).

237. M. A. Baqir, P. K. Choudhury, and M. J. Mughal, "Gold Nanowires-Based Hyperbolic Metamaterial Multiband Absorber Operating in the Visible and Near-Infrared Regimes," Plasmonics **14**, 485–492 (2019).

238. V. Y. Reshetnyak, I. P. Pinkevych, A. M. Urbas, and D. R. Evans, "Controlling hyperbolic metamaterials with a core-shell nanowire array [Invited]," Opt. Mater. Express **7**, 542 (2017).
239. R. Ferrando, R. L. Johnston, and C. Louis, "Recent advances in the chemical physics of nanoalloys," Phys. Chem. Chem. Phys. **17**, 27920–27921 (2015).
240. I. Chanu, P. Krishnamurthi, and P. T. Manoharan, "Effect of Silver on Plasmonic, Photocatalytic, and Cytotoxicity of Gold in AuAgZnO Nanocomposites," J. Phys. Chem. C **121**, 9077–9088 (2017).
241. H. Prunier, J. Nelayah, C. Ricolleau, G. Wang, S. Nowak, A. F. Lamic-Humblot, and D. Alloyeau, "New insights into the mixing of gold and copper in a nanoparticle from a structural study of Au-Cu nanoalloys synthesized via a wet chemistry method and pulsed laser deposition," Phys. Chem. Chem. Phys. **17**, 28339–28346 (2015).
242. Ö. Çelik and T. Fırat, "Synthesis of FeCo magnetic nanoalloys and investigation of heating properties for magnetic fluid hyperthermia," J. Magn. Magn. Mater. **456**, 11–16 (2018).
243. I. Robinson, S. Zacchini, L. D. Tung, S. Maenosono, N. T. K. Thanh, and C. Fisica, "Synthesis and Characterization of Magnetic Nanoalloys from Bimetallic Carbonyl Clusters," 3021–3026 (2009).
244. I. Parsina, C. Dipaola, and F. Baletto, "A novel structural motif for free CoPt nanoalloys," Nanoscale **4**, 1160–1166 (2012).
245. G. Barcaro, L. Sementa, and A. Fortunelli, "Nanoalloy Simulation," 1–13 (2015).
246. J. Zhao, K. Jarvis, P. Ferreira, and A. Manthiram, "Performance and stability of Pd-Pt-Ni nanoalloy electrocatalysts in proton exchange membrane fuel cells," J. Power Sources **196**, 4515–4523 (2011).
247. R. L. Paldi, X. Sun, X. Wang, X. Zhang, and H. Wang, "Strain-Driven In-plane Ordering in Vertically Aligned ZnO-Au Nanocomposites with Highly Correlated Metamaterial Properties," ACS Omega **5**, 2234–2241 (2020).
248. R. L. Paldi, X. Wang, X. Sun, Z. He, Z. Qi, X. Zhang, and H. Wang, "Vertically aligned AgxAu1-x alloyed nanopillars embedded in ZnO as nanoengineered low-loss hybrid plasmonic metamaterials," Nano Lett. (2020).

249. X. Wang, J. Jian, S. Diaz-Amaya, C. E. Kumah, P. Lu, J. Huang, D. G. Lim, V. G. Pol, J. P. Youngblood, A. Boltasseva, L. A. Stanciu, D. M. O'Carroll, X. Zhang, and H. Wang, "Hybrid plasmonic Au–TiN vertically aligned nanocomposites: a nanoscale platform towards tunable optical sensing," Nanoscale Adv. **1**, 1045–1054 (2019).
250. R. Kumar, G. Kumar, and A. Umar, "Pulse laser deposited nanostructured zno thin films: A review," J. Nanosci. Nanotechnol. **14**, 1911–1930 (2014).
251. S. M. Chou, L. G. Teoh, W. H. Lai, Y. H. Su, and M. H. Hon, "ZnO:Al thin film gas sensor for detection of ethanol vapor," Sensors **6**, 1420–1427 (2006).
252. B. Parida, S. Iniyan, and R. Goic, "A review of solar photovoltaic technologies," Renew. Sustain. Energy Rev. **15**, 1625–1636 (2011).
253. T. Chung, C. S. H. Hwang, M. S. Ahn, and K. H. Jeong, "Au/Ag Bimetallic Nanocomposites as a Highly Sensitive Plasmonic Material," Plasmonics **14**, 407–413 (2019).
254. L. W. McKeehan, "The crystal structure of silver-palladium and silver-gold alloys," Phys. Rev. **20**, 424–432 (1922).
255. S. Choopun, R. D. Vispute, W. Noch, A. Balsamo, R. P. Sharma, T. Venkatesan, A. Iliadis, and D. C. Look, "Oxygen pressure-tuned epitaxy and optoelectronic properties of laser-deposited ZnO films on sapphire," Appl. Phys. Lett. **75**, 3947–3949 (1999).
256. T. Bando, K. Abe, and M. Yamashita, "Effect of ZnO plasma plume dynamics on laser ablation," Opt. Rev. **17**, 309–312 (2010).
257. Z. G. Zhang, F. Zhou, X. Q. Wei, M. Liu, G. Sun, C. S. Chen, C. S. Xue, H. Z. Zhuang, and B. Y. Man, "Effects of oxygen pressures on pulsed laser deposition of ZnO films," Phys. E Low-Dimensional Syst. Nanostructures **39**, 253–257 (2007).
258. J. B. Franklin, B. Zou, P. Petrov, D. W. McComb, M. P. Ryan, and M. A. McLachlan, "Optimised pulsed laser deposition of ZnO thin films on transparent conducting substrates," J. Mater. Chem. **21**, 8178–8182 (2011).
259. J. Cao, T. Sun, and K. T. V. Grattan, "Gold nanorod-based localized surface plasmon resonance biosensors: A review," Sensors Actuators, B Chem. **195**, 332–351 (2014).
260. B. Casals, N. Statuto, M. Foerster, A. Hernández-Mínguez, R. Cichelero, P. Manshausen, A. Mandziak, L. Aballe, J. M. Hernàndez, and F. Macià, "Generation and Imaging of Magnetoacoustic Waves over Millimeter Distances," Phys. Rev. Lett. **124**, 1–6 (2020).

261. M. Küß, M. Heigl, L. Flacke, A. Hörner, M. Weiler, A. Wixforth, and M. Albrecht, "Nonreciprocal Magnetoacoustic Waves in Dipolar-Coupled Ferromagnetic Bilayers," Phys. Rev. Appl. **15**, 1 (2021).
262. R. Verba, V. Tiberkevich, and A. Slavin, "Wide-band nonreciprocity of surface acoustic waves induced by magnetoelastic coupling with a synthetic antiferromagnet," Phys. Rev. Appl. **12**, 1 (2019).
263. F. D. M. Haldane and S. Raghu, "Possible realization of directional optical waveguides in photonic crystals with broken time-reversal symmetry," Phys. Rev. Lett. **100**, 1–4 (2008).
264. J. S. Lee, A. Richardella, R. D. Fraleigh, C. xing Liu, W. Zhao, and N. Samarth, "Engineering the breaking of time-reversal symmetry in gate-tunable hybrid ferromagnet/topological insulator heterostructures," npj Quantum Mater. **3**, 1–7 (2018).
265. S. Huo and Y. Wei, "Experimental realization of three-dimensional elastic phononic topological insulator," 1–17 (n.d.).
266. J. Lu, R. L. Paldi, Y. Pachaury, D. Zhang, H. Wang, M. Kalaswad, X. Sun, J. Liu, X. L. Phuah, X. Zhang, A. A. El-Azab, and H. Wang, "Ordered hybrid metamaterial of La0.7Sr0.3MnO3–Au vertically aligned nanocomposites achieved on templated SrTiO3 substrate," Mater. Today Nano **15**, 100121 (2021).
267. J. Huang, T. Jin, S. Misra, H. Wang, Z. Qi, Y. Dai, X. Sun, L. Li, J. Okkema, H. T. Chen, P. T. Lin, X. Zhang, and H. Wang, "Tailorable Optical Response of Au–LiNbO3 Hybrid Metamaterial Thin Films for Optical Waveguide Applications," Adv. Opt. Mater. **6**, 1800510 (2018).
268. Q. Su, W. Zhang, P. Lu, S. Fang, F. Khatkhatay, J. Jian, L. Li, F. Chen, X. Zhang, J. L. Macmanus-Driscoll, A. Chen, Q. Jia, and H. Wang, "Self-Assembled Magnetic Metallic Nanopillars in Ceramic Matrix with Anisotropic Magnetic and Electrical Transport Properties," ACS Appl. Mater. Interfaces **8**, 20283–20291 (2016).
269. S. H. Mousavi, A. B. Khanikaev, and Z. Wang, "Topologically protected elastic waves in phononic metamaterials," Nat. Commun. **6**, 1–7 (2015).
270. M. Opel, S. T. B. Goennenwein, M. Althammer, K. W. Nielsen, E. M. Karrer-Müller, S. Bauer, K. Senn, C. Schwark, C. Weier, G. Güntherodt, B. Beschoten, and R. Gross, "Zinc oxide -From dilute magnetic doping to spin transport," Phys. Status Solidi Basic Res. **251**, 1700–1709 (2014).

271. B. I. Reser, "Calculation of the magnetic properties of Fe, Co and Ni with account taken of the real band structure and spin fluctuations," J. Phys. Condens. Matter **11**, 4871–4885 (1999).
272. A. Y. C. Yu, T. M. Donovan, and W. E. Spicer, "Optical properties of cobalt," Phys. Rev. **167**, 670–673 (1968).
273. H. Ehrenreich, H. R. Philipp, and D. J. Olechna, "Optical properties and fermi surface of nickel," Phys. Rev. **131**, 2469–2477 (1963).
274. K. Rode, A. Anane, R. Mattana, J. P. Contour, O. Durand, and R. LeBourgeois, "Magnetic semiconductors based on cobalt substituted ZnO," J. Appl. Phys. **93**, 7676–7678 (2003).
275. E. Echeverria, A. Kaphle, A. Austin, L. Bastatas, P. Hari, and D. McLlroy, "Evolution of the Stoichiometry and Electronic Structure of Cobalt Oxide in Thermally Treated Co-Doped ZnO Nanorods for Solar Cells," ACS Appl. Nano Mater. **2**, 4113–4120 (2019).
276. J. H. Kim, H. Kim, D. Kim, Y. E. Ihm, and W. K. Choo, "Magnetic properties of epitaxially grown semiconducting Zn 1-xCo xO thin films by pulsed laser deposition," J. Appl. Phys. **92**, 6066–6071 (2002).
277. N. H. Perry and T. O. Mason, "Phase equilibria of the zinc oxide-cobalt oxide system in air," J. Am. Ceram. Soc. **96**, 966–971 (2013).
278. J. C. Slater, "Atomic radii in crystals," J. Chem. Phys. **41**, 3199–3204 (1964).
279. R. Lizárraga, F. Pan, L. Bergqvist, E. Holmström, Z. Gercsi, and L. Vitos, "First Principles Theory of the hcp-fcc Phase Transition in Cobalt," Sci. Rep. **7**, 6–13 (2017).
280. Y. T. Jeon, J. Y. Moon, G. H. Lee, J. Park, and Y. Chang, "Comparison of the magnetic properties of metastable hexagonal close-packed Ni nanoparticles with those of the stable face-centered cubic Ni nanoparticles," J. Phys. Chem. B **110**, 1187–1191 (2006).
281. I. Ennen, D. Kappe, T. Rempel, C. Glenske, and A. Hütten, "Giant Magnetoresistance: Basic concepts, microstructure, magnetic interactions and applications," Sensors (Switzerland) **16**, (2016).
282. S. Shukla, N. K. Sharma, and V. Sajal, "Theoretical Study of Surface Plasmon Resonance-based Fiber Optic Sensor Utilizing Cobalt and Nickel Films," Brazilian J. Phys. **46**, 288–293 (2016).

283. Z. Kaminskiene, I. Prosyevasa, J. Stonkute, and A. Guobiene, "Evaluation of optical properties of ag, cu, and co nanoparticles synthesized in organic medium," Acta Phys. Pol. A **123**, 111–114 (2013).
284. J. B. Khurgin, "Replacing noble metals with alternative materials in plasmonics and metamaterials: How good an idea?," Philos. Trans. R. Soc. A Math. Phys. Eng. Sci. **375**, (2017).